Neutrino Flavor Conversions in High-Density Astrophysical and Cosmological Environments

Dissertation for Doctoral Degree

submitted to the department of Physics of
Universität Hamburg
and
to the department of Physics of
Università degli Studi di Napoli "Federico II"

Ninetta Saviano

born in Ottaviano, Italy

Hamburg 2013

Neutrino Flavor Conversions in High-Density Astrophysical and Cosmological Environments

Dissertation for Doctoral Degree

submitted to the department of Physics of
Universität Hamburg
and
to the department of Physics of
Università degli Studi di Napoli "Federico II"

Ninetta Saviano

born in Ottaviano, Italy

Hamburg 2013

- Corrected version -

The following evaluators recommend the admission of the dissertation:

Jun. Prof. Alessandro Mirizzi

Dr. Gianpiero Mangano

Dr. Pasquale Di Bari

Date of Disputation: 18-06-2013

Foreward

My research activity as PhD student in Astroparticle Physics has been focussed on neutrinos, and their role in astrophysics and cosmology. In particular, the "core" of my work is represented by the theoretical and phenomenological analysis of neutrino flavor transitions in supernovae and in the Early Universe, whose results have been published in [P1]–[P6]:

[P1] A. Mirizzi, G. Mangano, N. Saviano, E. Borriello, C. Giunti, G. Miele and O. Pisanti, "The strongest bounds on active-sterile neutrino mixing after Planck data," Physic Letter B **726**, 8-14 (2013).

[P2] N. Saviano, A. Mirizzi, O. Pisanti, P. D. Serpico, G. Mangano and G. Miele, Physical Review D **87**, 073006 (2013).

[P3] A. Mirizzi, N. Saviano, G. Miele and P. D. Serpico, "Light sterile neutrino production in the early universe with dynamical neutrino asymmetries," Physical Review D **86**, 053009 (2012).

[P4] N. Saviano, S. Chakraborty, T. Fischer and A. Mirizzi, "Stability analysis of collective neutrino oscillations in the supernova accretion phase with realistic energy and angle distributions," Physical Review D **85**, 113002 (2012).

[P5] S. Chakraborty, T. Fischer, A. Mirizzi, N. Saviano and R. Tomas, "Analysis of matter suppression in collective neutrino oscillations during the supernova accretion phase," Physical Review D **84**, 025002 (2011).

[P6] S. Chakraborty, T. Fischer, A. Mirizzi, N. Saviano and R. Tomas, "No collective neutrino flavor conversions during the supernova accretion phase," Physical Review Letters **107**, 151101 (2011).

Moreover, I also worked on perturbation theory in cosmology. The result of my study has been published in [P7]:

[P7] M. Pietroni, G. Mangano, N. Saviano and M. Viel, "Coarse-Grained Cosmological Perturbation Theory," Journal of Cosmology and Astroparticle Physics **1201**, 019 (2012).

The results of these studies have been also presented in various international conferences and have been published in the following proceedings:

[C1] N. Saviano, "Active sterile neutrino oscillations in the Early Universe with dynamical lepton asymmetries," Nuclear Physics Proceeding Supplement **237-238**, 259-262 (2013)

[C2] N. Saviano, S. Chakraborty, A. Mirizzi, "Matter suppression of collective supernova neutrino oscillations and stability analysis," to appear in the Blois 2012 proceedings.

[C3] S. Chakraborty, A. Mirizzi, N. Saviano, "New possibilities in supernova accretion phase from dense matter effect," proceeding of TAUP 2011, Journal of Physics: Conference Series **375**, 042039 (2012).

[C4] N. Saviano, S. Chakraborty, A. Mirizzi, "Matter suppression of collective supernova neutrino oscillations," Proceedings of the International School of Physics "Enrico Fermi", Course CLXXXII "Neutrino Physics and Astrophysics", (IOS, Amsterdam; SIF, Bologna) 2012, pp. 327-331.

[C5] A. Mirizzi, S. Chakraborty, N. Saviano, "Collective neutrino oscillations in supernovae: Matter suppression during the accretion phase," Proceedings of HANSE 2011, Series of DESY proceedings, pp. 90-93.

Abstract

The topic of this thesis is the study of the neutrino flavor conversions in high-density environments: the supernovae and the the Early Universe. Remarkably, these represent the only two cases in which neutrinos themselves contribute to the "background medium" for their propagation, making their oscillations a non-linear phenomenon. In particular, in the dense supernova core, the neutrino-neutrino interactions can lead in some situations to surprising and counterintuitive collective phenomena, when the entire neutrino system oscillates coherently as a single collective mode. In this context, we have shown that during the early SN accretion phase (post-bounce times $<$ 0.5 s) the matter density is so high to dominate over the neutrino density, suppressing the collective flavor conversions. We have characterized this suppression numerically solving the neutrino propagation equations. We have also supported our finding with a stability analysis of the neutrino equations of motion. Neutrino flavor conversions in the Early Universe are another fascinating problem involving collisional damping, refractive effects from charged leptons and neutrino self-interactions. In this thesis, we have studied the flavor conversions of active-sterile system of neutrinos in the Early Universe. This study has been motivated by hints for low-mass sterile neutrinos, coming from precision cosmological measurements and laboratory oscillation experiments. We performed an accurate solution of the kinetic equations for the evolution of the active-sterile ensemble in order to determine the relic abundance of sterile neutrinos. We took into account a possible primordial neutrino asymmetry ($L > 10^{-3}$) in order to suppress the sterile neutrino production and to find a better agreement between the cosmological and laboratory hints. Finally, we discuss the implications of our results on Big-Bang Nucleosynthesis and on the Cosmic Microwave Background from data measured by the Planck experiment.

Zusammenfassung

Das Thema der vorliegenden Arbeit ist die Analyse der gegenseitigen Umwandlung der Neutrinoflavors für Umgebungen hoher Dichte - Supernovae und das Frühe Universum. Bemerkenswerterweise sind dies die beiden einzigen Fälle, in denen die Neutrinos selbst zum "Hintergrundmedium" ihrer eigenen Ausbreitung beitragen und es sich somit bei ihren Oszillationen um ein nichtlineares Phänomen handelt. Insbesondere im dichten Kern einer Supernova können Neutrino-Neutrino-Wechselwirkungen unter bestimmten Bedingungen zu überraschenden und kontraintuitiven kollektiven Phänomenen führen, wenn das gesamte System aus Neutrinos kohärent in Form einer einzigen kollektiven Mode oszilliert. In diesem Zusammenhang haben wir gezeigt, dass während der frühen Akkretionsphase der SN (d.h. für Post-Bounce-Zeiten < 0.5 s) die Materiedichte hoch genug ist, um die Neutrinodichte zu dominieren und somit die kollektiven Flavorumwandlungen zu unterdrücken. Wir haben diese Unterdrückung durch numerisches Lösen der Gleichungen für die Ausbreitung der Neutrinos charakterisiert und konnten unsere daraus erhaltenen Ergebnisse durch eine Stabilitätsanalyse der Bewegungsgleichungen für Neutrinos bestätigen. Umwandlungen der Neutrinoflavors im Frühen Universum sind ein weiteres faszinierendes Problem, bei dem Stoßdämpfung, Brechungseffekte geladener Leptonen und Neutrinoselbstwechselwirkungen mit einbezogen werden müssen. In dieser Arbeit haben wir die Flavorumwandlung aktiv-steriler Neutrinosysteme im Frühen Universum untersucht. Dies wurde motiviert durch die aus kosmologischen Präzisionsmessungen und Oszillationsexperimenten im Labor stammenden Hinweise auf sterile Neutrinos geringer Masse. Durch sorgfältiges Lösen der kinetischen Gleichungen zur Beschreibung der Entwicklung des aktiv-sterilen Ensembles konnten wir den Wert der Relikthäufigkeit steriler Neutrinos ermitteln. Hierbei haben wir eine mögliche primordiale Neutrinoasymmetrie ($L > 10^{-3}$) berücksichtigt, um die Produktion steriler Neutrinos zu unterdrücken und eine bessere Übereinstimmung zwischen den Hinweisen aus der Kosmologie und aus Laborexperimenten zu erzielen. Abschließend diskutieren wir die Auswirkung unserer Ergebnisse auf die primordiale Nukleosynthese und auf die Kosmische Mikrowellenhintergrundstrahlung basierend auf den Messdaten des Planck-Experiments.

Sinopsi

L'argomento di questa tesi è lo studio delle oscillazioni di sapore dei neutrini in ambienti ad alta densità come le supernovae e l'Universo primordiale. Notoriamente, questi due ambienti rappresentano i due unici casi in cui i neutrini si propagano in un bagno di neutrini stessi. Questa caratteristica rende le loro oscillazioni un fenomeno non-lineare. In particolare, nelle regioni più interne di una supernova, le autointerazioni fra i neutrini possono produrre, in alcune situazioni, dei sorprendenti fenomeni collettivi in cui l'intero sistema dei neutrini oscilla coerentemente come un sistema a singolo modo. In questo contesto abbiamo dimostrato che nella fase iniziale di accrescimento di una supernova (a tempi dopo l'esplosione $t < 0.5$ s) la densità di materia è così alta da dominare quella dei neutrini, sopprimendo le loro oscillazioni collettive di sapore. Abbiamo caratterizzato questo effetto di soppressione risolvendo numericamente le equazioni di evoluzione del sapore. Abbiamo anche confermato i nostri risultati numerici applicando un'analisi di stabilità alle equazioni linearizzate.

Le oscillazioni di sapore nell'Universo primordiale costituiscono un altro affascinante problema in cui i neutrini sono interessati da effetti collisionali e rifrattivi sui leptoni carichi e sui neutrini stessi. In particolare, in questa tesi abbiamo studiato le conversioni di sapore di neutrini attivi in neutrini sterili. Questo studio è stato motivato da alcune indicazioni di neutrini sterili leggeri fornite da misure cosmologiche di precisione e da esperimenti di laboratorio sulle oscillazioni. Abbiamo condotto uno studio accurato delle equazioni cinetiche per l'evoluzione del sistema composto da neutrini attivi e sterili per determinare l'abbondanza fossile dei neutrini sterili nell'Universo primordiale. Abbiamo inoltre considerato la possiblità di asimmetrie primordiali fra i neutrini attivi ($L > 10^{-3}$) invocate per sopprimere la produzione dei neutrini sterili e permettere un accordo migliore fra le indicazioni cosmologiche e quelle di laboratorio. Infine, abbiamo discusso le implicazioni del nostro studio sulla nucleosintesi primordiale e sullo spettro della radiazione cosmica di fondo misurato dal satellite Planck.

Contents

Introduction

The possibility of neutrino flavor oscillations, first suggested half a century ago [1, 2, 3], is based on the fact that if neutrinos are massive, one would expect a leptonic mixing matrix analogous to the Cabibbo-Kobayashi-Maskawa (CKM) matrix for the quarks. Due to this flavor mixing, neutrinos produced with one flavor could be detected in another flavor state, in analogy with the well-known K_0-$\bar{K}_0$ oscillation mechanism. Since the original proposal, the search for neutrino flavor mixing has been pursued with increasing vigor. After many years of atmospheric, solar, accelerator and reactor neutrino observations, we have a good understanding of how neutrinos oscillate.

The current neutrino phenomenology based on the data from the above experiments (see, e.g., [4] for a review) is consistent with the simplest extension of the standard electroweak model needed to accommodate non-zero neutrino masses and mixings; namely, with a scenario where the three known flavor eigenstates $\nu_\alpha \equiv \nu_{e,\mu,\tau}$ are mixed with three mass eigenstates $\nu_i \equiv \nu_{1,2,3}$ through a unitary matrix U,

$$\nu_\alpha = \sum_i U^*_{\alpha i} \nu_i, \tag{1}$$

where $U = U(\theta_{12}, \theta_{13}, \theta_{23}, \delta_{CP})$ is a unitary matrix depending on the three mixing angles θ_{ij} and on a leptonic CP violating phase δ_{CP}. Currently, the two independent neutrino mass splittings, identifing the two oscillation scales, and the three mixing angles have been determined with an accurate precision [5, 6]. Notably, in 2012 the reactor experiments Daya-Bay [7], RENO [8] and Double-Chooz [9] determined the last unmeasured neutrino mixing angle θ_{13}. This result is important also for future perspectives since it gives access to the measurement of the CP violation in the neutrino sector with future planned experiments.

Now that the three-flavor oscillation framework is well determined, neutrino physics enters a new phase, where studies of neutrinos from new sources– in particular, cosmic neutrinos–are in the agenda. In spite of their weak interactions, there are two environments where neutrinos reach thermal equilib-

rium: a supernova core and the Early Universe. Neutrinos thus play a dominant role in the supernova and cosmic evolution. In particular, these two environments offer unique conditions to probe neutrino flavor conversions.

Core-collapse supernovae (SN) represent a unique laboratory to probe neutrino properties in the extreme conditions offered by a stellar gravitational collapse (see, e.g., [10] for a review). The role of astrophysical messengers played by neutrinos during a stellar collapse is largely associated with the signatures imprinted on the observable SN neutrino burst by flavor conversions occurring deep inside the star. At this regard, the dense SN core represents a crucial environment to investigate neutrino flavor mixing in high-density conditions. Indeed, within a radius of a few hundred kilometers, the neutrino gas is so dense to become a "background to itself", making the neutrino flavor evolution highly non-linear and leading in some situations to surprising and counterintuitive collective phenomena, when the entire neutrino system oscillates coherently as a single collective mode. As a result of these phenomena SN neutrinos can have their energy spectra partially swapped. This effect is sensitive to the (still unknown) neutrino mass hierarchy.

The Early Universe offers another, different environment to test neutrino properties in high-density conditions. In particular, neutrino flavor conversions in Early Universe are a fascinating problem involving collisional damping, refractive effects from charged leptons, and neutrino self-interactions [66]. In this context, there is a renewed interest for active-sterile neutrino oscillation in the Early Universe, after intriguing but controversial hints of extra radiation in the Universe coming from precision cosmological measurements, supporting the existence of low-mass sterile neutrinos [12]. On the other hand, anomalous results of short-baseline neutrino oscillation experiments may also be interpreted in terms of sterile neutrinos, as recently emphasized [13]. However, it is not so simple to link the laboratory hints for sterile neutrinos with the cosmic extra-radiation, since the primordial abundance of thermal sterile neutrinos would be in tension with cosmological observables.

Given the importance for particle physics, cosmology and astrophysics of neutrino oscillations in supernovae and in the Early Universe, we devote this thesis to perform a detailed study of the neutrino flavor transitions in these two environments. The structure of this thesis is as follows.

In Chapter 1 we present a general introduction on the current framework in which neutrino oscillations are described. We discuss neutrino oscillations in vacuum and in matter and we summarize the current status of the three-flavor neutrino oscillation phenomenology. Finally, we discuss about different anomalies recently found in short-baseline experiments, that seem to point towards the existence of low-mass ($m \sim 1$ eV) sterile neutrinos.

In Chapter 2 we describe the neutrino equations of motion, necessary to characterize the oscillations of neutrinos which are in thermal equilibrium as in the supernova core or in the Early Universe. In these environments neutrinos scatter on the background medium and on themselves. Boltzmann-type kinetic equations in terms of the neutrino density matrix are presented to take into account simultaneously neutrino oscillations and collisions.

In Chapter 3 we present the general picture of stellar collapse and Supernova explosion, with emphasis on the time evolution of the neutrino burst from such an event. Then we discuss about the non-linear oscillations occurring in the deepest supernova regions associated to the neutrino-neutrino interactions. We present different oscillations regimes that can be encountered by neutrinos propagating in the supernova envelope and the possible signatures induced on the observable supernova neutrino spectra.

In Chapter 4 we discuss our study on the non-linear flavor conversions for supernova neutrinos emitted during the early time accretion phase (post-bounce time $t < 0.5$ s). This phase would offer the best opportunity to detect effects from neutrino flavor oscillations, since the emitted neutrino fluxes are large with a distinct flavor hierarchy. We perform a dedicated study of this problem, characterizing the neutrino emissivity and the SN matter density profile, using results from recent neutrino radiation hydrodynamical simulations. We realize that during the accretion phase the matter density, piled-up above the neutrino-sphere, is so high that it dominates over the neutrino density. In contrast to what is expected in the presence of only neutrino-neutrino interactions, we find that the trajectory-dependent effects associated with the dense ordinary matter suppress collective oscillations. We discuss the phenomenological consequences of our findings. We also present the results from an analytical approach to interpret and predict the outcome of our numerical simulations, based on a stability analysis of the linearized equations of motion.

In Chapter 5 we describe the role of neutrinos in cosmology. At first, we discuss the neutrino thermalization in the Early Universe. Then, we consider the impact of neutrinos on different cosmological observables like the Cosmic Microwave Background and Big Bang Nucleosynthesis. Finally, we present the current situation concerning the determination of the extra-radiation in the Early Universe and we comment about the data from different experiments.

In Chapter 6 we present the results of our study on active-sterile neutrino oscillations in the Early Universe. We describe the kinetic equations for the mixing of active and sterile neutrinos in multi-flavor systems. Motivated by the recent data release of the Planck satellite experiment, we perform an extensive scan of the sterile neutrino parameter space. Once more we con-

firm the tension between the cosmological data and the mass and mixings suggested by the laboratory hints. As a possible escape-route to relieve this tension we consider a primordial neutrino asymmetry to suppress the sterile neutrino production. We solve the equations of motion in this situation, calculating the sterile neutrino abundance for different values of the neutrino asymmetries ($L > 10^{-3}$). Then, we discuss also the impact of these flavor conversions on the Big-Bang Nucleosynthesis.

Finally in the Conclusions we summarize our results and we draw the conclusions of this work.

Chapter 1

Neutrinos properties and oscillations

1.1 Neutrinos in the Standard Model

Postulated by Pauli in 1930 as a *"verzweifelter Ausweg"* (desperate way out) to save the energy conservation in the beta decay of nuclei, the existence of (electron) neutrino was really established only in the 1956, detecting the $\overline{\nu}_e$ emitted by nuclear reactors. Now we know that there are three flavors of neutrinos ν_e, ν_μ, ν_τ (with the corresponding antiparticles $\overline{\nu}_e, \overline{\nu}_\mu, \overline{\nu}_\tau$) and the only force trough which these electrically-neutral, fermionic and *nearly massless* leptons interact is the weak force, described by the Standard Model (SM) of fundamental interactions among elementary particles. Indeed, neutrinos of each flavor participate in reactions, mediated by $W^\pm$ bosons, in which the charged leptons of the corresponding type are involved, like the decay $W^\pm \to l_a^\pm + \nu_a(\overline{\nu}_a)$, where $a = e, \mu, \tau$, or related processes. In addition to these charged-current reactions (CC), neutrinos can participate in neutral-current interactions (NC), mediated by the Z^0 boson, like the elastic or quasi elastic scattering processes and the decay $Z^0 \to \nu_a \overline{\nu}_a$. In particular, the last process is crucial to determine the number of light active neutrino species, measuring the invisible width of the Z^0 boson, which depends on the number of (kinematically allowed) decay channels. The measurement of the Z^0 boson width at LEP agrees with a number (2.98 ± 0.01) of neutrinos [14].

In the minimal version of the electroweak part of the SM, based on the symmetry group $SU(2)_L$ x $U(1)_Y$, the neutrinos are left-handed particles "ν_L" and there are no right-handed neutrino states "ν_R". Conversely, their antiparticles $\overline{\nu}_e$, $\overline{\nu}_\mu$, $\overline{\nu}_\tau$ are right-handed. The Lagrangian density governing

the weak interactions is the following:

$$\mathcal{L}_{\text{weak}} = \mathcal{L}_{CC} + \mathcal{L}_{NC} = -\frac{g}{2\sqrt{2}} J^{\mu}_{CC} W_{\mu} + h.c. - \frac{g}{2\cos\theta_{\text{w}}} J^{\mu}_{NC} Z_{\mu} + h.c. \quad (1.1)$$

where g is the coupling constant of the $SU(2)_L$ group, θ_{w} is the Weinberg angle. J^{μ}_{CC}, J^{μ}_{NC} are the weak leptonic charged-current and weak leptonic neutral-current, respectively, describing three-body process involving two fermions and $W^{\pm}$ or Z^0 gauge bosons:

$$J^{\mu}_{CC} = 2(\overline{\nu_{eL}}\gamma^{\mu} e_L + \overline{\nu_{\mu L}}\gamma^{\mu}\mu_L + \overline{\nu_{\tau L}}\gamma^{\mu}\tau_L) + \text{quark terms}$$

$$J^{\mu}_{NC} = 2(g^{\nu}_L\ \overline{\nu_{\alpha L}}\gamma^{\mu}\nu^{\alpha}_L + g^{l}_L\ \overline{l_{\alpha L}}\gamma^{\mu} l^{\alpha}_L + g^{l}_R\ \overline{l_{\alpha R}}\gamma^{\mu} l^{\alpha}_R) + \text{quark terms} \quad (1.2)$$

with $g^{\nu}_L = \frac{1}{2}$, $g^{l}_L = -\frac{1}{2} + \sin^2\theta_{\text{w}}$, $g^{l}_R = \sin^2\theta_{\text{w}}$.

The left-handed fields are given by the left-handed projection *chirality* operator $P_L = (1-\gamma_5)/2$, such that

$$\overline{\nu_{lL}}\ \gamma^{\mu}\ l_L = \overline{\nu_l}\ \gamma^{\mu}\frac{1}{2}(1-\gamma_5)\ l; \qquad l = e, \mu, \tau.$$

Conversely, $P_R = (1+\gamma_5)/2$ is the right-handed projection chirality operator. In the massless limit, left chirality fields are associated to left-handed helicity particles and right-handed helicity antiparticles, where the helicity is the spin component along the direction of motion.

For energies carried by the fermions much smaller than the mass of the gauge bosons ($M_W, M_Z \sim \mathcal{O}$ (100) GeV), the weak CC and NC processes at tree level are described by the effective Lagrangian in terms of the 4-fermions point-like interaction (the so called Fermi interaction)

$$\mathcal{L}_{\text{eff}} = -\frac{G_F}{\sqrt{2}} J^{\mu\dagger}_{CC} J_{\mu CC} - 2\frac{G_F}{\sqrt{2}} J^{\mu}_{NC} J_{\mu NC}, \quad (1.3)$$

where $G_F = \sqrt{2}\ g^2/(8\ m^2_W) = 1.166 \times 10^{-5}$ GeV^{-2} is the Fermi constant.

1.2 Neutrinos mass

The most sensitive probe of the neutrino mass is represented by neutrino oscillations. In the last two decades, a long series of neutrino oscillation experiments has established that neutrinos mix and than have non zero mass.

Indeed a flavor eigenstate, produced via CC interactions, is a mixture of neutrino mass eigenstates and therefore the probability of detecting a particular flavor for a neutrino oscillates with time as it propagates. The nature and the absolute scale of the mass of neutrinos are still unknown together with the question if neutrinos coincide with their antiparticles (*Majorana* neutrinos) or not (*Dirac* neutrinos).

The mass term connects the left-handed field to its right-handed partner, namely it flips the chirality of the particles.p There are two ways to extend the electroweak part of the standard model in order to include massive neutrinos. One is represented by the Dirac mass term (like for the other charged leptons and quarks)

$$\mathcal{L}_{\text{Dirac}} = -m\overline{\nu}\ \nu = -m(\overline{\nu_R}\nu_L + \overline{\nu_L}\nu_R), \tag{1.4}$$

adding three right-handed neutrinos fields ν_R which are sterile in the sense they are singlets for the gauge group since they do not interact with the other particles. In this case, neutrino and antineutrino are two different particles, each one with two possible values of the helicity, for a total of 4 degrees of freedom. Moreover, the neutrino and antineutrino fields are independent and the neutrino field splits into two independent components with definite chirality, ν_L and ν_R. The Dirac mass term preserves the lepton number.
For neutrinos, it is possible to build a mass Lagrangian, in term of only the left-handed states ν_L, the so called Majorana mass term

$$\mathcal{L}_{\text{Majorana}} = -\frac{1}{2}M(\overline{\nu_L^C}\nu_L + \overline{\nu_L}\nu_L^C) \tag{1.5}$$

where ν_L^C is the charge conjugated neutrino field with right-handed chirality and the factor $1/2$ takes into account the double counting of degrees of freedom. This mass term violates the lepton number of two units and it is possible only for neutral fermions such as neutrinos, making the neutrino and the antineutrino indistinguishable and giving a total of 2 degrees of freedom. Even if one introduces a right-handed neutrino, it would be not independent but rather related to the left-handed (by a matrix transformation) and only one chirality is possible.

In the massless limit, the distinction between Dirac and Majorana neutrinos is irrelevant and is not necessary to introduce both chiral components. Instead for massive neutrinos, while this distinction does not affect oscillation experiments [15], it is crucial in situations where the lepton number violation plays a role (as in the case of neutrinoless double beta decay [16]). Moreover the nature of the neutrino mass is very important in some theories used to explain both the small value of the neutrinos mass with respect to the other fermions and the baryon asymmetry of the universe by leptogenesis (see, e.g.,

[17] for a review). In particular the *seesaw mechanism* (see, e.g., [18] for a review) provides a very simple and fascinating explanation of the smallness smallness of the neutrino mass since it relates it to the existence of very large mass scale: "*the heavier on side, the lighter the other side*". The right-handed neutrino ν_R has a large Majorana mass $M \in [10^{10} - 10^{12}]$ GeV, while the left-handed neutrinos ν_L has mass

$$m_\nu = \frac{m_D^2}{M}, \tag{1.6}$$

where m_D is the Dirac mass, responsible for the mixing between ν_L and ν_R.

1.3 Neutrino oscillations

The idea of neutrino flavor conversions was first suggested by Pontecorvo in the 1957 [1] and it is based on the fact that if neutrinos are massive, one would expect a leptonic mixing matrix analogous to the Cabibbo-Kobayashi-Maskawa (CKM) matrix for the quarks. Consequently, neutrinos produced with one flavor could be detected in another flavor state, in analogy with the $K^0 - \overline{K}^0$ oscillation mechanism. Neutrino oscillations are a quantum mechanical phenomenon, generated by the interference of different massive neutrinos. Indeed, the neutrinos are produced via CC interaction as flavor eigenstates that are a linear superposition of mass eigenstates. As a neutrino propagates through space, the quantum mechanical phases of the mass states diffuse at different rates due to the slight differences in their masses, resulting in a changing mixture of mass states as the neutrino travels.

The first experimental research was stimulated by the necessity to understand the "solar neutrino problem", namely, the deficit of the measured solar ν_e flux with respect to the theoretical predictions based on the standard solar model [19, 20, 21], and finally solved in terms of *solar* $\nu_e \to \nu_x$ oscillations (with $x = \mu, \tau$) [22, 23]. Additional evidences for neutrino oscillations came from a long series of different detection strategies: *atmospheric* neutrino oscillations [24] and *terrestrial* neutrino oscillations from reactor [25, 7, 8, 9] and accelerator experiments [26].

If neutrinos are massive, the flavor eigenstates $|\nu_\alpha\rangle$, $\alpha = e, \mu, \tau$, which diagonalize the charged current, can be expressed as a quantum superposition of mass eigenstates $|\nu_i\rangle$, $i = 1, 2, 3$ which diagonalize the mass matrix:

$$|\nu_\alpha\rangle = \sum_i U^*_{\alpha i} \, |\nu_i\rangle \, . \tag{1.7}$$

The unitary 3×3 mixing matrix U (the leptonic analogue of the quark mixing matrix), sometimes referred to as the *Pontecorvo-Maki-Nakagawa-Sakata* (PMNS) matrix [14] is:

$$U = \begin{pmatrix} c_{12}c_{13} & s_{12}c_{13} & s_{13}e^{-i\delta} \\ -s_{12}c_{23} - c_{12}s_{23}s_{13}e^{-i\delta} & c_{12}c_{23} - s_{12}s_{23}s_{13}e^{-i\delta} & s_{23}c_{13} \\ s_{12}s_{23} - c_{12}c_{23}s_{13}e^{i\delta} & c_{12}s_{23} - s_{12}c_{23}s_{13}e^{i\delta} & c_{23}c_{13} \end{pmatrix} \times \begin{pmatrix} 1 & 0 & 0 \\ 0 & e^{i\beta} & 0 \\ 0 & 0 & e^{i\gamma} \end{pmatrix} \tag{1.8}$$

with $s_{ij} = \sin\theta_{ij}$, $c_{ij} = \cos\theta_{ij}$ and θ_{12}, θ_{23}, θ_{13} are the three mixing angles. The phase δ is a CP-violating phase present in both Majorana and Dirac neutrino cases, while β and γ are CP-violating phases present only in the case of Majorana neutrinos.

Even if the most evident proof of the neutrino masses are the neutrino flavor oscillations, these are not sensitive to the absolute mass but only to the mass-square differences $m_i^2 - m_j^2$. The current neutrino phenomenology implies that three-neutrino mass spectrum $\{m_i\}$, with $i = 1, 2, 3$, is formed by a *doublet* of relatively close states and by a third *single* neutrino state, which may be either heavier than the doublet ("Normal Hierarchy", NH) or lighter ("Inverted Hierarchy", IH) (Fig. 1.1).

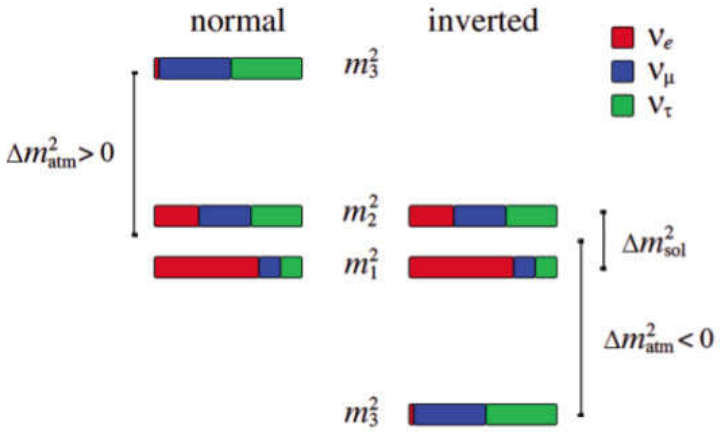

Figure 1.1: Neutrino mass ordering: normal mass hierarchy (left) and inverted mass hierarchy (right).

The lightest neutrino of the doublet is usually referred as ν_1 while the heaviest one is ν_2 and the corresponding mass-square difference is defined as

$$\Delta m^2_{21} = \Delta m^2_{\rm sol} = m_2^2 - m_1^2 \; > \; 0 \tag{1.9}$$

and indicated as solar mass-square difference.

The single state is labeled as ν_3 and the sign of $m_3^2 - m_{1,2}^2$ distinguishes the two hierarchies. The second independent mass-square difference, known as the atmospheric mass-square difference, is defined by

$$\Delta m^2_{32,1} = \Delta m^2_{\text{atm}} = \left| m_3^2 - \frac{m_1^2 + m_2^2}{2} \right| . \tag{1.10}$$

1.3.1 Oscillations in vacuum

As discussed before, in the standard theory of neutrino oscillations, a neutrino with flavor α $(= e, \mu, \tau)$ and momentum $\mathbf{p}$, created in a CC interaction process from a charged lepton or together with a charged antilepton, is described by the quantum superposition Eq. (1.7). The massive neutrino states ν_i $(i = 1, 2, 3)$ are eigenstates of the Hamiltonian $\mathcal{H} |\nu_i\rangle = \Omega_i^0 |\nu_i\rangle$ with energy eigenvalues $\Omega_i^0 = \sqrt{p^2 + m_i^2}$.

For propagation of ultrarelativistic neutrinos the full spin structure is not probed. Weak-interactions couple only to left-handed component of ν and chirality conservation is satisfied to $\mathcal{O}(m/E)$. Since for $E \gg m$, only the propagation of ν_L is relevant, eliminating the spin structure, one gets the Schrödinger-like equation [27]:

$$i\partial_t |\nu_i\rangle = \mathcal{H} |\nu_i\rangle , \tag{1.11}$$

whether the ν is a Dirac or Majorana particle. This equation implies that the massive neutrino states evolve in time as plane waves:

$$|\nu_i(t)\rangle = e^{-i\Omega_i^0 t} |\nu_i\rangle \quad . \tag{1.12}$$

Consequently, the time evolution of a neutrino created with a definite flavor is given by

$$|\nu_\alpha(t)\rangle = \sum_i U^*_{\alpha i} e^{-i\Omega_i^0 t} |\nu_i\rangle . \tag{1.13}$$

Using the unitarity of the matrix U, finally we obtain

$$|\nu_\alpha(t)\rangle = \sum_{\beta=e,\mu,\tau} \left(\sum_i U^*_{\alpha i} \, e^{-i\Omega_i^0 t} \, U_{\beta i} \right) |\nu_\beta\rangle . \tag{1.14}$$

The transition probability from one state to another is given by:

$$P_{\nu_\alpha \to \nu_\beta} = |\langle \nu_\beta | \, \nu_\alpha(t)\rangle|^2 . \tag{1.15}$$

Sometimes the neutrino oscillation phenomenology can be described in terms of simplified 2-ν scenarios associated with a mass-squared splitting and a

mixing angle θ. In this case, the two flavor neutrino states are linear superpositions of the two massive states ν_1 e ν_2 with coefficients given by the elements of the 2×2 orthogonal mixing matrix

$$U = \begin{pmatrix} c_\theta & s_\theta \\ -s_\theta & c_\theta \end{pmatrix}, \tag{1.16}$$

where θ is the mixing angle, with a value in the interval $0 \leq \theta \leq \pi/2$. Considering that there is only one mass-squared difference, $\Delta m^2 = m_2^2 - m_1^2$ and expanding $\Omega_i^0 = \sqrt{p^2 + m_i^2} \simeq p + m_i^2/2p \simeq p + m_i^2/2E$, the probability $\nu_\alpha \to \nu_\beta$, with $\alpha \neq \beta$, after an interval of t is:

$$\begin{aligned} P_{\nu_\alpha \to \nu_\beta} &= |\langle \nu_\beta | \, \nu_\alpha(t) \rangle|^2 = \\ &= \left| (0 \;\; 1) \begin{pmatrix} c_\theta & s_\theta \\ -s_\theta & c_\theta \end{pmatrix} \begin{pmatrix} e^{-i\Omega_1^0 t} & 0 \\ 0 & e^{-i\Omega_2^0 t} \end{pmatrix} \begin{pmatrix} c_\theta & -s_\theta \\ s_\theta & c_\theta \end{pmatrix} \begin{pmatrix} 1 \\ 0 \end{pmatrix} \right|^2 = \\ &= \frac{1}{2} \sin^2 2\theta \left[1 - \cos(\Omega_2^0 - \Omega_1^0) t \right] \simeq \sin^2 2\theta \sin^2 \left(\frac{\Delta m^2}{4E} t \right). \end{aligned} \tag{1.17}$$

Since for ultra-relativistic neutrinos $L \simeq t$, one can write:

$$P_{\nu_\alpha \to \nu_\beta} = |\langle \nu_\beta | \, \nu_\alpha(t) \rangle|^2 = \sin^2 2\theta \sin^2 \left(\frac{\Delta m^2}{4E} \; L \right). \tag{1.18}$$

where L is the distance between the source and the detector. For $\alpha = \beta$, the *survival probability* $P_{\nu_\alpha \to \nu_\alpha}$ is obtained by unitarity from the previous transition probability:

$$P_{\nu_\alpha \to \nu_\alpha} = |\langle \nu_\alpha | \, \nu_\alpha(t) \rangle|^2 = 1 - \sin^2 2\theta \sin^2 \left(\frac{\Delta m^2}{4E} \; L \right). \tag{1.19}$$

From the previous expression one can infer the following considerations. First the oscillation amplitude $A = \sin^2 2\theta$ is determined by the mixing angle and does not allow to distinguish between θ and $\pi/2 - \theta$, leading to the "octant" degeneracy of the transition probability in vacuum. The degeneracy will be removed in the case of neutrino propagation in matter. Moreover, the oscillation wave-length is given by

$$\lambda = \frac{4\pi E}{\Delta m^2} = 2.48 \text{ km } \frac{E}{\text{GeV}} \; \frac{\text{eV}^2}{\Delta m^2} \tag{1.20}$$

and it is then macroscopic. Finally in a realistic setup, since the neutrino beam is not monochromatic and the energy resolution of the detector is not perfect, one need to average the oscillation probability around some energy

range ΔE. Furthermore, the production and detection regions typically have finite size, so it is also necessary to average around some path-length range ΔL, loosing the phase information. Then the transition probability is just the *classical* one. Indeed, the phase acquired during neutrino propagation is averaged out and it is possible to sum incoherently over the propagation eigenstates, i.e. the mass eigenstates. The resulting averaged probability of transition from a flavor to another one is simply

$$\langle P_{\nu_\alpha \to \nu_\beta} \rangle = \frac{1}{2} \sin^2 2\theta. \tag{1.21}$$

1.3.2 Oscillations in matter

Neutrino oscillations in matter may significantly differ from the oscillations in vacuum due to modification of the neutrino propagation. For example, it is known that the photon which is massless in vacuum acquires an effective mass in medium, due to the refractive effects associated with the interactions with the particles in the medium. In analogy to the photon, Wolfenstein suggested that neutrinos propagating in matter are subject to an interaction potential, equivalent to a refraction index, due to the coherent forward scatterings (at the first order in the Fermi constant G_F), with the particles in the medium [28]. As we will see this would profoundly modify the mixing properties. Actually, neutrinos in matter are also affected by incoherent scatterings at the second order in G_F . These incoherent scatterings are extremely small in most situations and can be in general neglected. We will comment later on their role in the flavor conversions of neutrinos in the Early Universe.

It is intriguing that even if the vacuum mixing angle is small, matter effects can significantly enhance it. In particular, Mikheyev and Smirnov [29] understood that, in case of varying density medium, the neutrinos traveling in it can experience resonant flavor transitions through the famous *Mikheyev, Smirnov, Wolfenstein effect (MSW)*. This mechanism plays a crucial role in interpreting oscillations of neutrinos during their propagation in matter, as e.g. in the case of solar and supernova neutrinos. The evolution equation is affected by two effective potentials associated with the forward CC and NC scatterings with the constituents of the medium. The CC interactions, mediated by the $W^\pm$ bosons, are possible only for ν_e since μ and τ are not present in the normal matter. For an unpolarized medium, the effective potential becomes (see [27] for details)

$$V_{CC} = \sqrt{2}\, G_F\, n_e, \tag{1.22}$$

with n_e the electron density. For what concerns the NC contributions to the matter-induced neutrino potentials, being flavor independent, they are irrelevant for neutrino oscillations.

Considering an ultrarelativistic neutrino ν_α of flavor $\alpha = e, \mu, \tau$, this is a superposition of massive states $|\nu_i\rangle$ [Eq. (1.7)], eigenstates of the free Hamiltonian $\mathcal{H}_0$. The total Hamiltonian in matter is given by $\mathcal{H}_0 + \mathcal{H}_I$, where $\mathcal{H}_I$ is the interaction Hamiltonian, diagonal in the flavor basis, such that $\mathcal{H}_I |\nu_\alpha\rangle = V_\alpha |\nu_\alpha\rangle$.

In the Schrödinger picture, the evolution of the neutrino ν_α is given by:

$$i\frac{d}{dt}|\nu_\alpha(t)\rangle = (\mathcal{H}_0 + \mathcal{H}_I)|\nu_\alpha(t)\rangle\,. \tag{1.23}$$

For the sake of brevity, we consider only two neutrino families, the ν_e and ν_x ($x = \mu, \tau$) and the two mass eigenstates ν_1 and ν_2, with mass-squared difference Δm^2. Neglecting common phases, irrelevant for neutrino oscillations which depend only on the phase differences, the evolution equation can be written as

$$i\frac{d}{dt}\begin{pmatrix}\nu_e\\ \nu_\mu\end{pmatrix} = \frac{1}{4E}\begin{pmatrix}-\Delta m^2\cos 2\theta + 2|p|V_{CC} & \Delta m^2\sin 2\theta\\ \Delta m^2\sin 2\theta & -\Delta m^2\cos 2\theta - 2|p|V_{CC}\end{pmatrix}\begin{pmatrix}\nu_e\\ \nu_\mu\end{pmatrix}. \tag{1.24}$$

The diagonalization of the effective Hamiltonian in Eq. (1.24) gives the following neutrino eigenstates in matter [27]

$$\begin{pmatrix}\nu_1^m\\ \nu_2^m\end{pmatrix} = \begin{pmatrix}\cos\theta_m & -\sin\theta_m\\ \sin\theta_m & \cos\theta_m\end{pmatrix}\begin{pmatrix}\nu_e\\ \nu_\mu\end{pmatrix} \tag{1.25}$$

where the mixing angle in matter θ_m is given by

$$\sin^2 2\theta_m = \frac{\left(\frac{\Delta m^2}{2E}\right)^2\sin^2 2\theta}{\left[\frac{\Delta m^2}{2E}\cos 2\theta - \sqrt{2}G_F n_e\right]^2 + \left(\frac{\Delta m^2}{2E}\right)^2\sin^2 2\theta}. \tag{1.26}$$

The MSW resonance condition occurs for [28, 29, 27]

$$\sqrt{2}G_F n_e = \frac{\Delta m^2}{2E}\cos 2\theta. \tag{1.27}$$

which corresponds to the electron number density

$$n_e^{\rm res} = \frac{\Delta m^2\cos 2\theta}{2\sqrt{2}EG_F}. \tag{1.28}$$

In this circumstance the mixing angle is maximal, i.e. $\theta_m = \pi/4$, leading to a complete transition from one flavor to another, if the resonance region is

wide enough. Since in normal matter V_{CC} is positive, the resonance can exist only for $\theta \leq \pi/4$, otherwise the cosine would be negative.

For constant matter density, the vacuum solution can be converted to the solution in a medium by replacing the vacuum quantities with their corresponding medium quantities

$$P_{m\ \nu_e \to \nu_\mu} = \sin^2 2\theta_m \sin^2 \left(\frac{\Delta m^2_m}{4E}\ L \right) \tag{1.29}$$

with the effective squared-mass difference in matter

$$\Delta m^2_m = \sqrt{\left(\Delta m^2 \cos 2\theta - 2\sqrt{2} E G_F\ n_e \right)^2 + (\Delta m^2 \sin 2\theta)^2}. \tag{1.30}$$

Conversely, in the case of not constant matter density, it is necessary to take into account the variation of the mixing angle in matter $\dot{\theta}_m = d\theta_m/dx$ along the neutrino trajectory. In particular the off-diagonal terms proportional to this variation could be responsible of transitions between the instantaneous neutrino mass eigenstates. These transitions are, however, negligible if the off-diagonal terms are much smaller than the diagonal ones. This is the case of the *adiabatic propagation* in which the density is slowly changing on a distance scale of roughly the wave length in matter and the mass states become eigenstates of the Hamiltonian. An important consequence of the adiabatic evolution is the possibility of large flavor swaps even in presence of small mixing angles, when neutrinos encounter a resonance [27].

1.4 Neutrino phenomenology

Experiments on neutrinos aim at determining the neutrino mixing properties studying their flavor conversions. Moreover, the determination of the absolute neutrino mass scale and its nature (Dirac or Majorana) is an important independent goal. In addition, a significant boost to the knowledge of different neutrino properties comes from astrophysical and cosmological observations. In the following we will briefly introduce the determination of the mass and mixing parameters.

1.4.1 Mass searches

For what concerns the absolute scale of the neutrino mass, information can be obtained by measuring the spectrum of electrons near the end point in β-decay experiments and from cosmological and astrophysical data. The

present experimental upper bound on the ν_e mass was obtained in the Troitzk experiment studying ^{3}H β-decay: $m_{\nu_e} < 2.05$ eV [30]. The KArlsruhe TRItium Neutrino (KATRIN) β-experiment, currently under construction, will be able to reduce this bound by one order of magnitude [31]. The Cosmic Microwave Background (CMB) data of the Wilkinson Microwave Anisotropy Probe (WMAP) experiment, combined with galaxy clustering data can be used to obtain an upper limit on the sum of neutrinos masses. Depending on the cosmological model and the dataset used one obtains $\sum_i m_i < 0.3-1.3$ eV [32]. The recent results of Planck experiments give the bound $\sum_i m_i < 0.28$ eV combining CMB and Baryonic Acoustic Oscillation (BAO) data [135].

The best method to probe the nature of neutrinos is represented by the study of the *neutrinoless double* β-decay of nuclei. Indeed, $0\nu2\beta$ decays, in which only two electrons or two positrons are emitted but no neutrinos, violating lepton number by two units, are allowed for Majorana neutrinos and forbidden for Dirac neutrinos [16]. All $0\nu2\beta$ experiments provide only upper bounds on the neutrino mass (the most sensitive in the eV range [34]. An exception is represented by the Heidelberg-Moscow experiment [35], with the claim of a positive (but highly debated [34]) $0\nu2\beta$ signal, corresponding to a Majorana mass in the sub-eV range at best-fit [36].

1.4.2 Neutrino mixing parameters

Neutrino mixing parameters have been studied for more than 40 years in a long series of oscillation experiments exploiting different techniques and sources. In Fig. 1.2 are represented different classes of neutrino experiments with the corresponding neutrino energy and path length. We see that neutrinos have been studied from both natural sources or artificial ones. In particular the pioneering experiments on neutrino oscillations were related to the solar neutrino detection (at MeV energies) [20], followed by experiments on atmospheric neutrinos (at GeV energies) [24]. Neutrinos in the MeV energy range have been detected also from the explosion of Supernova 1987A [37, 38, 39]. Neutrinos from artificial sources like accelerators (at GeV energies)[26] and reactors (MeV energies [25]) are also crucial in probing the neutrino mixing. An experiment with typical neutrino energies E and a distance L between source and detector is sensitive to a minimal value of the mass-squared difference of

$$\left(\delta m^2\right)_{min} \simeq \frac{E}{L}. \tag{1.31}$$

In Table 1.1 is indicated the minimum δm^2 probed by different experiments. In particular in Figure 1.2 the solar (with $\Delta m^2_{\rm sol} \sim 7 \times 10^{-5}$ eV^2) and

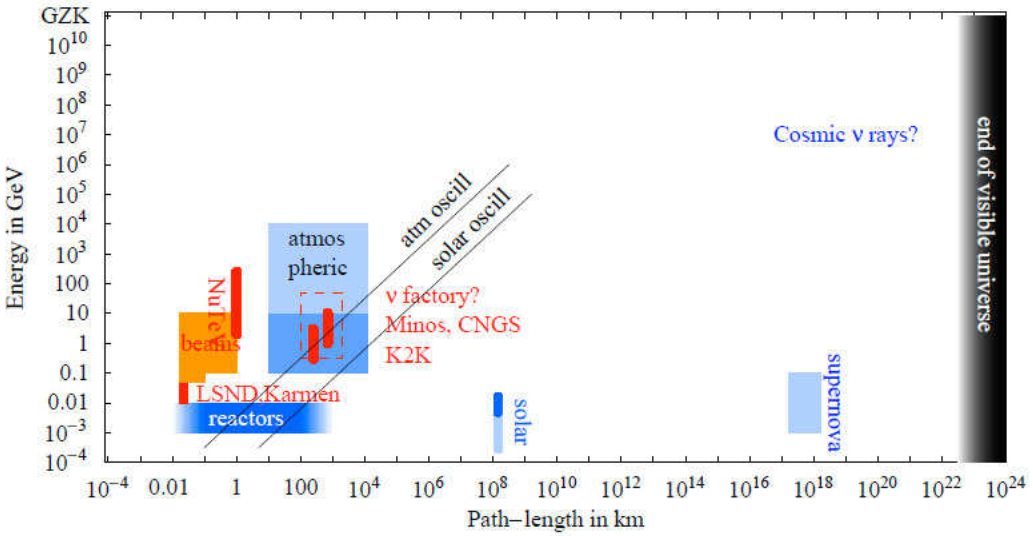

Figure 1.2: Energy and pathleght for different neutrino sources and experiments. Figure taken from [4].

Table 1.1: Characteristics of typical oscillation experiments.

Source	Flavor	E [GeV]	L [km]	$(\delta m^2)_{\min}$ [eV^2]
Atmosphere	$\overset{(-)}{\nu}_e$, $\overset{(-)}{\nu}_\mu$	$10^{-1} \ldots 10^{2}$	$10 \ldots 10^{4}$	10^{-6}
Sun	ν_e	$10^{-3} \ldots 10^{-2}$	10^{8}	10^{-11}
Reactor	$\bar{\nu}_e$	$10^{-4} \ldots 10^{-2}$	10^{-1}	10^{-3}
Accelerator	ν_e, $\overset{(-)}{\nu}_\mu$	$10^{-1} \ldots 1$	10^{2}	10^{-1}

atmospheric (with $\Delta m^2_{\text{atm}} \sim 3 \times 10^{-3}$ eV^2) neutrino oscillations occur below the black lines.

In the following we will describe in more details these different classes of experiments.

1. Δm^2_{21} and θ_{12}: solar and reactor neutrinos

   The Sun is a powerful source of ν_e of energy of MeV, produced in the thermonuclear fusion reactions occurring in the core. Several experiments have been devoted to measure the solar neutrino flux, starting from the historical Chlorine experiment (1965) in the Homestake mine in the US [19], which provided the first evidence of a neutrino deficit, with respect to the theoretical prediction of the solar model. This deficit, known as the Solar Neutrino Problem, has stimulated an enormous amount of theoretical investigations to give an explanation of this anomaly in terms of possible modifications of the solar model or alternative particle physics scenarios. Now it is well-known that this deficit is due to neutrino flavor conversions and the determination of the solar neutrino mass and mixing parameters are mainly provided by Super Kamiokande (SK) [40], Subdury Neutrino Observatory (SNO) [22, 23], Borexino [41]. The Δm^2_{12} and θ_{12} have been independently confirmed by the reactor experiment KamLAND in Japan studying the disappearance of $\overline{\nu}_e$ produced by nuclear reactors on a baseline of ~ 200 km [25].

2. Δm^2_{32} and θ_{23}: atmospheric and terrestrial long-baseline experiments

   The experimental determination of Δm^2_{32} and θ_{32} is principally due to the Super-Kamiokande measurement of atmospheric neutrinos.

   Atmospheric neutrinos are produced by collision of primary cosmic rays (typically protons) with nuclei in the atmosphere, creating a shower of hadrons, mainly pions which in turn decay into muons, electrons and neutrinos. This would give a flavor ratio $\nu_e : \nu_\mu = 1 : 2$. Muons produced by ν_μ reactions at $E >$GeV show an anomalous zenith angle distributions. Indeed the flux of up-ward going muons is about two times lower than the flux of down-ward going muons. Instead, the electron sample is compatible with no oscillations. By the analysis of all data, Super Kamiokande has established, without any doubt, the occurrence of $\nu_\mu \to \nu_\tau$ oscillations, while ν_e were unaffected [24, 42]. The results of Super Kamiokande have been confirmed by a series of experiments using neutrinos produced at accelerators. These experiments, using ν_μ with energy higher than 1 GeV, are for example, MINOS, OPERA and Tokai-to-Kamioka (T2K). Minos is situated in the Sudan mine, 735 km north of Fermilab. Observing ν_μ charged current events and therefore

Parameter	Best fit	1σ range	2σ range	3σ range
$\Delta m^2_{12}/10^{-5}$ eV^2 (NH or IH)	7.54	7.32 – 7.80	7.15 – 8.00	6.99 – 8.18
$\sin^2\theta_{12}/10^{-1}$ (NH or IH)	3.07	2.91 – 3.25	2.75 – 3.42	2.59 – 3.59
$\Delta m^2_{13}/10^{-3}$ eV^2 (NH)	2.43	2.33 – 2.49	2.27 – 2.55	2.19 – 2.62
$\Delta m^2_{13}/10^{-3}$ eV^2 (IH)	2.42	2.31 – 2.49	2.26 – 2.53	2.17 – 2.61
$\sin^2\theta_{13}/10^{-2}$ (NH)	2.41	2.16 – 2.66	1.93 – 2.90	1.69 – 3.13
$\sin^2\theta_{13}/10^{-2}$ (IH)	2.44	2.19 – 2.67	1.94 – 2.91	1.71 – 3.15
$\sin^2\theta_{23}/10^{-1}$ (NH)	3.86	3.65 – 4.10	3.48 – 4.48	3.31 – 6.37
$\sin^2\theta_{23}/10^{-1}$ (IH)	3.92	3.70 – 4.31	3.53 – 4.84 $\oplus$ 5.43 – 6.41	3.35 – 6.63
δ/π (NH)	1.08	0.77 – 1.36	—	—
δ/π (IH)	1.09	0.83 – 1.47	—	—

Table 1.2: Results of the global 3ν oscillation analysis [5].

ν_μ disappearance, MINOS provides a determination of θ_{23} and Δm^2_{32} in agreement with the SK one [43, 44]. Opera is a detector located at the Gran Sasso laboratory in Italy designed to explicitly detect ν_τ appearance from a ν_μ neutrino beam produced at CERN [45]. The appearance of a third ν_τ (the latest in March 2013) confirms the indirect, but solid, interpretation of the SK results in terms of $\nu_\mu \to \nu_\tau$ oscillations.

3. The latest neutrino mixing angle: θ_{13}

   The determination of θ_{13} is important for several reasons. First it completes the determination of the mixing angle, giving possible indications for flavor models. Moreover, as results from Eq. (1.8), θ_{13} is necessary condition to have access to possible CP violation effects in the neutrino sector. The first hints for a value different from zero of θ_{13} emerged in in the 2008 by a global analysis of different neutrino oscillations data [46] and in the 2011 by the T2K experiment[26], but only the last year the reactor experiments Daya Bay [7] and RENO [8] have definitely established $\theta_{13} > 0$ at 5 σ. This results has been confirmed by the reactor experiment Double Chooz [9].

In conclusion, except for a few anomalous results (to be discussed later), recently observed in short-baseline terrestrial neutrino experiments, all data from neutrino oscillation experiments can be interpreted in the standard three-neutrino framework, described in terms of six parameters governing neutrino mixing. Still unknown are the mass ordering (the neutrino mass hierarchy) and the CP violating phase. The current status of the 3 ν mass and mixing framework is summarized in Table 1.2, taken from [5].

1.4.3 Anomalies and sterile neutrinos

Even if the 3 ν scenario successfully explains most of the data coming from the oscillation experiments, there exist a few experimental results (called

"anomalies") that cannot be explained in this framework. If interpreted as oscillation signals, these anomalies point towards the possible existence of additional sterile neutrino species behind the 3 active species (see [13] for a review). These sterile particles, predicted as new gauge singlets by many theoretical models beyond the Standard Model, are neutral leptons insensitive to weak force interacting only gravitationally. Their masses are usually postulated heavy, but lighter sterile neutrinos are anyway possible. Indeed, although the most popular models of neutrino mass-generation, the seesaw mechanisms, normally involve sterile neutrinos with mass close to the grand unification scale or the TeV scale, a priori there is no theoretical constraint on the mass of these particles.

The first evidence, at 3.8σ level, comes from the short baseline LSND experiment [47], studying $\overline{\nu}_\mu \to \overline{\nu}_e$ oscillations, providing a $\Delta m^2 = 1$ eV^2 much larger than those required from a three-neutrino analysis. The KARMEN experiment, built with characteristics very similar to LSND, did not support such evidence [48], although a joint analysis of the two experiments shows that their data sets are compatible with oscillations at Δm^2 either in a band [0.2–1] eV^2 or in a region around 7 eV^2 [49]. The experiment MiniBooNE, designed to test the LSND anomaly, and sensitive both to $\nu_\mu \to \nu_e$ and $\overline{\nu}_\mu \to \overline{\nu}_e$ transitions, has given different results during the last few years. The initial results of the MiniBooNE experiment did not verify oscillation evidence in the $\nu_\mu \to \nu_e$ [50]. Later the collaboration presented new results for the antineutrino oscillation channel supporting the LSND evidence, requiring $\Delta m^2 = 1$ eV^2 [51]. In a new preliminary data release, this significance has decreased, but it is still consistent with the LSND signal. In addition, an unexplained excess of electron-like events is observed in MiniBooNE at low energies. The simultaneous analysis of LSND (antineutrino) and MiniBooNE (neutrino and antineutrino) could be explained in terms of sterile neutrino oscillations only assuming CP-violation or some other exotic scenarios. An independent test of the LSND and MiniBooNE anomalies has been recently performed at the LBL accelerator experiment ICARUS [52]. The combination of the four experiments LSND, KARMEN, MiniBooNE and ICARUS, restricts the allowed mass-mixing parameters to a small region around $\Delta m^2 \sim 0.5$ eV^2 and $\sin^2 2\theta \sim 5 \times 10^{-3}$.

An additional anomaly supporting oscillations with sterile neutrinos has recently appeared from a revaluation of reactor antineutrino fluxes, with a 3% of increase relative to previous calculations of the mean flux. As a result, data from reactor neutrino experiments at very short distances can be interpreted as an apparent 6% deficit of $\overline{\nu}_e$ [53]. Known as the reactor antineutrino anomaly, it is again compatible with sterile neutrinos having a $\Delta m^2 \sim \mathcal{O}(1)$ eV^2. However the calculation of the emitted antineutrino spec-

	3+1	**3+2**
Δm^2_{41} [eV^2]	0.89	0.90
$\|U_{e4}\|^2$	0.025	0.017
$\|U_{\mu 4}\|^2$	0.023	0.019
Δm^2_{51} [eV^2]		1.61
$\|U_{e5}\|^2$		0.017
$\|U_{\mu 5}\|^2$		0.0061

Table 1.3: Best–fit values of the mixing parameters obtained in 3+1 and 3+2 fits of short-baseline oscillation data taken from [55].

trum is very difficult, involving the sum of thousands of β-branches weighted by the branching ratio of each transition. Finally, an independent experimental evidence for ν_e disappearance at very short baseline exists from the Gallium radioactive source experiments GALLEX and SAGE which consist in the detection of electron neutrinos produced by intense artificial ^{51}Cr and ^{37}Ar radioactive sources placed inside the detectors [54]. The exact statistical significance of the deficit depending on the assumptions made on the theoretical estimate of the cross section $\nu_e \ + ^{71} Ga \rightarrow ^{71} Ge \ + e^-$. Both the reactor and gallium anomalies can be interpreted in terms of a phenomenon of ν_e disappearance driven by sterile neutrino oscillations. Scenarios with one (dubbed "3+1") or two ("3+2") sub-eV sterile neutrinos have been proposed to fit the different data [55, 56, 57, 58]. In the Table 1.3, taken from [55], are reported the best-fit values of the mixing parameters obtained in 3+1 and 3+2 fits of short-baseline oscillation data and used in our study.[1]

As we will see later, cosmology provides an important arena to test these scenarios. In fact, neutrinos are abundantly produced via weak interactions in the hot (temperature $T \gg 1$ MeV) primordial cosmological plasma. The sterile mass eigenstate(s) can be produced via oscillations with the active ones and can modify cosmological observables.

[1] See Chapter 6 for details on the 4 ν formalism.

Chapter 2

Neutrino oscillations in high density environments

2.1 Density matrix formalism

As discussed in the previous Chapter, the treatment of neutrino mixing is well understood in terms of the the propagation of a beam of particles, in vacuum or in a medium. In particular the evolution of the neutrino flavor transitions has been described by means of the Schrödinger equation. However this simple formalism is insufficient whenever we are concerned with the evolution of a statistical ensemble of neutrinos simultaneously mixing and scattering in a medium. This is a typical situation encountered during stellar collapse or in the early Universe. Such problems cannot be easily understood in terms of the propagation of a beam. Indeed, while this treatment allows to obtain the transition probabilities between single-particle states and to study the oscillations between field amplitudes, it cannot be directly applied to many-particle states. Specifically, we need to handle the interactions between the medium and the coherent superposition of states that are involved. In presence of a propagation medium it is important to follow the evolution of the whole ensemble, including those particles scattered out of the beam. Two types of effects have to be considered. One concerns the refractive effect described in Sec. 1.3.2. The second effect is due to collisions which destroy the coherence of the evolution and can influence the behavior of the mixing process.

In addition to the interactions with the external medium, one has also to consider the interactions of neutrinos among themselves (*self-interaction*). Indeed, as pointed out by Pantaleone in the 1992 [59] , in the deepest region of the Supernova (SN) and in the Early Universe, the neutrinos gas is so

dense that the neutrinos themselves form a background medium leading to intriguing non-linear effects in the neutrino flavor conversions.

A proper treatment of all these effects requires to exploit the density matrix formalism, in which mixed quantum states for neutrinos and possible loss of coherence due to real collisions are described together. We will strictly follow the derivation of [60]. See also [61, 62, 63, 64].

Let us consider the momentum expansion of a left-handed massless neutrino field

$$\psi_L(x) = \int d\mathbf{p}(a_{\mathbf{p}} u_{\mathbf{p}} + b^\dagger_{-\mathbf{p}} u_{-\mathbf{p}}) e^{i\mathbf{p}\cdot\mathbf{x}} \tag{2.1}$$

where $d\mathbf{p} = d^3\mathbf{p}/(2\pi)^3$, the Dirac spinors $u_{\mathbf{p}}$ and $v_{\mathbf{p}}$ refer to massless negative-helicity neutrinos and positive-helicity antineutrinos, respectively. Moreover, $a_{\mathbf{p}}$ is the annihilation operator for negative helicity neutrinos of momentum $\mathbf{p}$, while $b^\dagger_{\mathbf{p}}$ is the creation operator for positive helicity antineutrinos. For n neutrino flavor states, either active or sterile, these operators are column vectors with anticommutation relations

$$\{a_i(\mathbf{p}), a_j^\dagger(\mathbf{p}')\} = \{b_i(\mathbf{p}), b_j^\dagger(\mathbf{p}')\} = \delta_{ij}(2\pi)^3\delta^{(3)}(\mathbf{p}-\mathbf{p}'). \tag{2.2}$$

From all possible bilinears involving the operators a and b, the only ones that do not violate lepton number by two units, or whose expectation values do not oscillate around zero, are $a^\dagger a$ $b^\dagger b$. Requiring also the spatial homogeneity, their expectation values contribute only for equal momenta $\mathbf{p} = \mathbf{p}'$. Therefore, a homogeneous ensemble of neutrinos and antineutrinos can be characterized by the $n \times n$ density matrices $\varrho_{\mathbf{p}}(t)$ and $\overline{\varrho}_{\mathbf{p}}(t)$ defined for neutrinos and antineutrinos, respectively, as

$$\begin{aligned} \langle a_j^\dagger(\mathbf{p}) a_i(\mathbf{p}')\rangle &= (2\pi)^3\delta^{(3)}(\mathbf{p}-\mathbf{p}')(\varrho_{\mathbf{p}})_{ij} \\ \langle b_i^\dagger(\mathbf{p}) b_j(\mathbf{p}')\rangle &= (2\pi)^3\delta^{(3)}(\mathbf{p}-\mathbf{p}')(\overline{\varrho}_{\mathbf{p}})_{ij} \end{aligned} \tag{2.3}$$

The reversed order of the indices in the definition of $\overline{\varrho}$ guarantees that both density matrices transform in the same way under a unitary transformation $\psi' = U^\dagger \psi U$. The diagonal elements of $\varrho_{\mathbf{p}}$ and $\overline{\varrho}_{\mathbf{p}}$ are the usual particle and antiparticle distribution functions (occupation numbers) for the corresponding neutrino species, while the off-diagonal ones encode phase information and vanish for zero mixing,

$$\varrho_{\mathbf{p}} = \begin{pmatrix} \varrho_{ee} & \varrho_{e\mu} & \varrho_{e\tau} \\ \varrho_{\mu e} & \varrho_{\mu\mu} & \varrho_{\mu\tau} \\ \varrho_{\tau e} & \varrho_{\tau\mu} & \varrho_{\tau\tau} \end{pmatrix}, \qquad \overline{\varrho}_{\mathbf{p}} = \begin{pmatrix} \overline{\varrho}_{ee} & \overline{\varrho}_{e\mu} & \overline{\varrho}_{e\tau} \\ \overline{\varrho}_{\mu e} & \overline{\varrho}_{\mu\mu} & \overline{\varrho}_{\mu\tau} \\ \overline{\varrho}_{\tau e} & \overline{\varrho}_{\tau\mu} & \overline{\varrho}_{\tau\tau} \end{pmatrix}. \tag{2.4}$$

2.2 Equations of motion for the neutrino ensemble

The evolution in time of $\varrho_{\mathbf{p}}$ and $\overline{\varrho}_{\mathbf{p}}$ is obtained as a perturbative expansion in the Heisenberg formalism, assuming the appropriate Hamiltonian of weak interactions. Considering up to the second order in the perturbation expansion, we can write the equation of motion (EoM) in the form Boltzmann-like collisional equation for neutrinos

$$i\dot{\varrho}_{\mathbf{p}} = i\partial_t \varrho_{\mathbf{p}} = +[\Omega^{\rm vac}_{\mathbf{p}}, \varrho_{\mathbf{p}}] + [\Omega^{\rm ref}_{\mathbf{p}}, \varrho_{\mathbf{p}}] + \mathcal{C}[\varrho_{\mathbf{p}}], \tag{2.5}$$

where $[\cdot,\cdot]$ is a commutator. The equation for antineutrinos is obtained adopting the following prescription: $\varrho_{\mathbf{p}} \to \overline{\varrho}_{\mathbf{p}}$, $\Omega^{\rm ref}_{\mathbf{p}} \to \overline{\Omega}^{\rm ref}_{\mathbf{p}}$, The first term at the r.h.s of the Eq. (2.5) represents, in the flavor basis, the usual vacuum oscillation effects in absence of interactions. For ultrarelativistic neutrinos

$$\Omega^{\rm vac}_{\mathbf{p}} = U\frac{M^2}{2p}U^\dagger \tag{2.6}$$

where U is the mixing matrix and M^2 is the squared mass matrix which, apart from a common term proportional to the identity matrix and irrelevant for the oscillations, is parametrized as [176]:

$$M^2 = \mathrm{diag}\left(m^2_{12}, m^2_{12}, m^2_{23}\right) = \left(-\frac{\Delta m^2_{21}}{2}, +\frac{\Delta m^2_{21}}{2}, \pm\frac{\Delta m^2_{32}}{2}\right). \tag{2.7}$$

The second term represents the *refractive potential term* at the first order in the perturbation expansion ($\propto G_F$) responsible for an energy shift due to forward scattering in the medium. This term is the sum of two contributions:

$$\Omega^{\rm ref}_{\mathbf{p}} = \Omega^{\rm M}_{\mathbf{p}} + \Omega^{\nu\nu}_{\mathbf{p}} \tag{2.8}$$

where $\Omega^{\rm M}_{\mathbf{p}}$ describes the interactions with all other particles of the medium except for neutrinos, $\Omega^{\nu\nu}_{\mathbf{p}}$ represents the "self-interactions" with the other neutrinos in the medium and, depending on the neutrino ensemble $\varrho_{\mathbf{p}}$ itself, it makes the problem non-linear.

Finally, the last term at the right-hand side (r.h.s) of the Eq. (2.5) is the second order in the perturbative expansion ($\propto G_F^2$), known as *collisional term*, responsible for the breaking of the coherence of the neutrino ensemble.

In the next section, we will discuss more in details the different terms involved in the EoM.

2.2.1 Neutrino interaction terms

Refraction terms with an ordinary background medium For the environments and temperatures which we are interested in, we can consider the ordinary background medium as composed only by electrons and positrons. The Feynman diagrams for these interactions are represented in the panel *(a)* and *(b)* of the Fig. 2.1.

- *Leading order*

  Starting from the four-leptons weak Hamiltonian

$$\mathcal{H}_{\nu e}^{\text{eff}} = \frac{G_F}{\sqrt{2}} \left[\overline{\nu_e}\gamma^\mu(1-\gamma_5)\nu_e\right] \left[\overline{e}\gamma_\mu(1-\gamma_5)e\right] \tag{2.9}$$

  and considering a gas of unpolarized electrons with a statistical distribution function $f(\mathbf{k})$, the refractive potential can be written as [65]

$$V_{\nu e} = \pm\sqrt{2}G_F n_{e^-} \int \mathrm{d}\mathbf{k} f(E_\mathbf{k})(1 - \mathbf{v_k}\cdot\mathbf{v_p}) \tag{2.10}$$

  where n_{e^-} is the the number density of the electrons and the + sign refers to neutrinos while the − one to antineutrinos. The term $(1-\mathbf{v_k}\cdot\mathbf{v_p})$ comes form the the current-current structure of the weak interactions, with $\mathbf{v_k}$ and $\mathbf{v_p}$ the electron and neutrino velocities. It reduces to 1 in case of isotropy of the electron background. The same procedure for positrons yields an opposite sign in the result. Therefore, the refractive potential experienced by neutrinos travelling in a isotropic background of electron and positron is

$$\Omega^{\mathrm{M}(0)} = \pm\sqrt{2}\, G_F\, n_e, \tag{2.11}$$

  where $n_e = (n_{e^-} - n_{e^+})$ is the net electron density.

- *Higher order*

  Including the mass of gauge bosons in the Hamiltonian, the contribution due to CC interaction with the isotropic background medium is:

$$\Omega^{\mathrm{M}(1)} = -\frac{8\sqrt{2}\, G_F p}{3m_W^2}(\epsilon_{e^-} + \epsilon_{e^+}), \tag{2.12}$$

  where ϵ_e is the energy density of electrons and positrons. The sign is the same for neutrinos and antineutrinos.

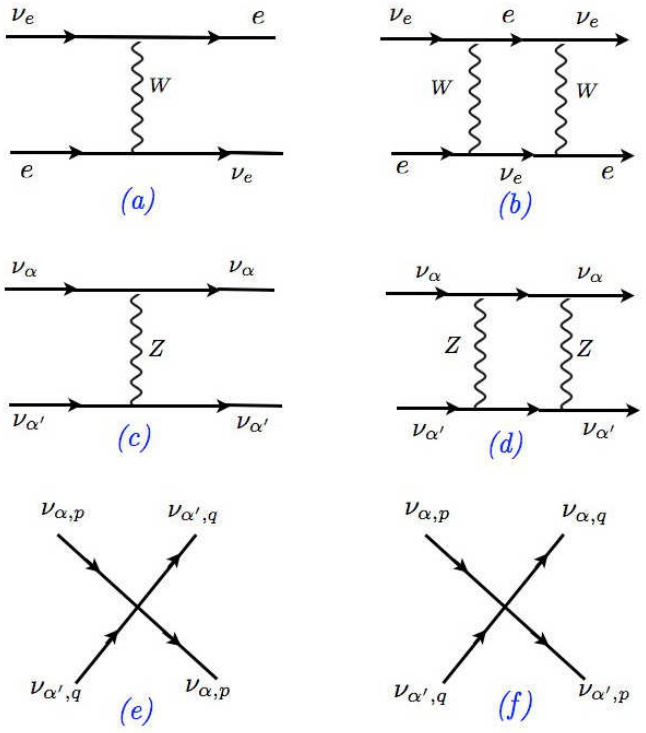

Figure 2.1: Representative amplitudes contributing to forward scatterning: *(a)* leading order and *(b)* higher order CC interactions *(c)* leading order and *(d)* higher order NC interactions, *(e)* and *(f)* momentum conserving and momentum exchanging processes, respectively, corresponding to the low-energy limit of *(c)*.

Self-interaction terms In extreme environments, such as the SN and the Early Universe, the density of the neutrinos can be very high that the neutrinos themselves form a background medium for their propagation [59]. The neutrino-neutrino interactions, $\propto G_F$, make an additional contribution to the refractive energy shift. In particular, in addition to the diagonal refractive index, there will be present also "off-diagonal refractive potentials" given by the zero-momentum transfer processes in which neutrinos exchange flavor. The amplitudes contributing to these processes are shown in the panel *(c)*, *(d)*, *(e)*, *(f)* of the Fig. 2.1.

- *Leading order*

Neutrino-neutrino forward scattering at three level presents not only processes in which ν do not exchange momenta, corresponding to the effective Hamiltonian

$$\mathcal{H}^{\text{eff}}_{\nu\nu} = \frac{G_F}{\sqrt{2}} \left[\overline{\nu_e}(\mathbf{p})\gamma^\mu(1-\gamma_5)\nu_e(\mathbf{p})\right] \left[\overline{\nu_x}(\mathbf{q})\gamma_\mu(1-\gamma_5)\nu_x(\mathbf{q})\right] \tag{2.13}$$

but also processes in which neutrinos exchange their flavors, which results in a exchange of the momenta:

$$\mathcal{H}^{\text{eff}}_{\nu\nu} = \frac{G_F}{\sqrt{2}} \left[\overline{\nu_e}(\mathbf{q})\gamma^\mu(1-\gamma_5)\nu_e(\mathbf{p})\right] \left[\overline{\nu_x}(\mathbf{p})\gamma_\mu(1-\gamma_5)\nu_x(\mathbf{q})\right]. \tag{2.14}$$

In [60] it was shown that, using the density matrix formalism, the leading order self interaction term can be written as

$$\Omega^{\nu\nu(0)}_{\mathbf{p}} = \pm\sqrt{2}G_F \int \mathrm{d}\mathbf{q}\ (1-\mathbf{v_q}\cdot\mathbf{v_p}) \left\{G_S(\varrho_{\mathbf{q}} - \overline{\varrho}_{\mathbf{q}})G_S + G_S\ \mathrm{Tr}\left[(\varrho_{\mathbf{q}} - \overline{\varrho}_{\mathbf{q}})G_S\right]\right\}, \tag{2.15}$$

where G_S is the standard model coupling matrix which in the tree-level case is the unit matrix in flavor space, $G_S = \mathbf{1}$. (This is not true anymore if one or more neutrinos are sterile). The term $(1-\mathbf{v_q}\cdot\mathbf{v_p}) = (1-\cos\theta_{\mathbf{qp}})$ takes into account the angular dependence of the scattering amplitude. In the case of isotropic medium, it averages to 1, as in the case of the Early Universe. Instead it is important for neutrinos streaming form a SN core. Again, + sign refers to neutrinos while the − one to antineutrinos.

- *Higher order*

In order to include the correction due to the non-local nature of the Z-boson propagator which mediate forward scattering on neutrinos of the same species, we consider also the term

$$\Omega^{\nu\nu(1)}_{\mathbf{p}} = -\frac{8\sqrt{2}G_F\ p}{3m_Z^2} \int \mathrm{d}\mathbf{q}\ \frac{3}{4}(1-\mathbf{v_q}\cdot\mathbf{v_p})^2\ q\ G_S(\varrho_{\mathbf{q}} + \overline{\varrho}_{\mathbf{q}})G_S. \tag{2.16}$$

The sign does not change in the antineutrino equations.

Collisional term The term $\mathcal{C}[\varrho_{\mathbf{p}}]$ accounts for processes $\propto G_F^2$ such as creation and annihilation and all the momentum exchanging processes of neutrinos with the leptonic background and among neutrinos themselves. In particular it contains the scattering processes with the medium X of the form $\nu_{\mathbf{p}} X \to X' \nu_{\mathbf{p}'}$, production and absorption by CC processes of the type $X \to X' \nu_{\mathbf{p}}$ or $\nu_{\mathbf{p}} X \to X'$ (and the same processes for antineutrinos) and also the NC pair processes $XX' \to \nu_{\mathbf{p}} \overline{\nu}_{\mathbf{p}'}$ and $\nu_{\mathbf{p}} \overline{\nu}_{\mathbf{p}'} \to XX'$.

Following again [60], we consider the part of the interaction Hamiltonian which is bilinear in the left-handed neutrino field ψ. After a suitable Fierz transformation, the Hamiltonian can be written as an affective NC interaction with an external medium consisting of various particle species. Assuming these different target species uncorrelated, their interference terms can be neglected (being proportional to the second order forward scattering) and then the collisional term becomes an incoherent sum over all target species. A lengthy calculation gives

$$\begin{aligned}(\mathcal{C}[\varrho_{\mathbf{p}}])_{\mathrm{NC}} = &+\frac{1}{2}\int \mathrm{d}\mathbf{p}' \left[W(p',p)(1-\varrho_{\mathbf{p}})G\varrho_{\mathbf{p}'}G - W(p,p')\varrho_{\mathbf{p}}G(1-\varrho_{\mathbf{p}'})G\right] + \\ &+\frac{1}{2}\int \mathrm{d}\mathbf{p}' \left[W(-p',p)(1-\varrho_{\mathbf{p}})G(1-\overline{\varrho}_{\mathbf{p}'})G - W(p,-p')\varrho_{\mathbf{p}}G\,\overline{\varrho}_{\mathbf{p}'}G + h.c.\right],\end{aligned} \tag{2.17}$$

where the isotropy of the medium was assumed. The non-negative transition probabilities $W(p',p) \equiv W(p_\mu, p'_\mu)$ are Wick contractions of medium operators of the form

$$W(p',p) = 2\, G_F^2\, \mathcal{M}^{\mu\nu}(p'-p)\, \mathcal{N}_{\mu\nu}(p',p) \tag{2.18}$$

with $\mathcal{M}^{\mu\nu}(p'-p)$ and $\mathcal{N}_{\mu\nu}(p',p)$ the "medium structure function tensor" and the "neutrino tensor", respectively. G represents a $n \times n$ matrix of dimensionless coupling constant, which in the flavor basis reads $G = \mathrm{diag}(g_1, ..., g_n)$. The first two terms at the r.h.s. of the Eq. (2.17) are due to neutrino scattering off the medium, the positive term being a gain term corresponding to a scattering process while the negative one being a loss term corresponding to the inverse reaction. The third and fourth terms account for pair processes with the positive term being a gain term from pair creations by medium, while the negative one is a loss term from pair annihilations. For a more detailed treatment see [60] and the references therein. We note that in the limit of a single neutrino flavor, or several unmixed flavors, the role of $\varrho_{\mathbf{p}}$ is played by the usual occupation number while the matrix G is the unit matrix. Then the Eq. (2.17) resembles the usual Boltzmann collisional integral, which we will discus later.

- *Damping prescription*

The complete form of the collisional term is quite complicated. However, in many cases, a sufficiently accurate description can be achieved if the scattering and pair processes are mimicked by a damping term. Concerning the scattering processes, from the several heuristic formulations present in literature, we take advantage of the following form for the collisional integral:

$$\mathcal{C}[\varrho_{\mathbf{p}}] = -\frac{1}{2}\Gamma_{\mathbf{p}}[G,[G,\varrho_{\mathbf{p}}]] \tag{2.19}$$

where $\Gamma_{\mathbf{p}}$ denotes a total rate for all the interactions considered. For the explicit forms of the rate and of the matrix G, we refer to the Chapter 6. Finally, we remark that the double commutator structure ensures that the total lepton number is conserved.

2.3 Two extreme environments: the Early Universe and the supernova core

Neutrinos play a dominant role in the evolution of the Early Universe and of the supernova core. In particular, these two environments offer unique conditions to probe neutrino flavor mixing in high-density conditions, involving refractive effects from charged leptons and collisional damping. Moreover, these represent the only two cases in which neutrinos themselves contribute to the background medium for their propagation, making their oscillations a non-linear phenomenon and leading, in some situations, to surprising and counterintuitive collective phenomena.

In the most general situation, the flavor evolution for the density matrices $\varrho_{\mathbf{p},\mathbf{x}}$ and $\bar{\varrho}_{\mathbf{p},\mathbf{x}}$ (depending in general on the momentum $\mathbf{p}$ and on the coordinate $\mathbf{x}$) in dense environments is governed by the Boltzmann collision equations

$$\hat{L}[\varrho_{\mathbf{p},\mathbf{x}}] = -i[\Omega_{\mathbf{p},\mathbf{x}},\varrho_{\mathbf{p},\mathbf{x}}] + \hat{\mathcal{C}}[\varrho_{\mathbf{p},\mathbf{x}}] \tag{2.20}$$

and a similar equation for $\bar{\varrho}_{\mathbf{p}}$. At r.h.s. $\Omega_{\mathbf{p},\mathbf{x}} = \Omega^{\rm vac}_{\mathbf{p}} + \Omega^{\rm ref}_{\mathbf{p},\mathbf{x}}$. The l.h.s. contains the Liouville operator

$$\hat{L}[\varrho_{\mathbf{p},\mathbf{x}}] = \partial_t \varrho_{\mathbf{p},\mathbf{x}} + \mathbf{v}_{\mathbf{p}} \cdot \nabla_{\mathbf{x}}\, \varrho_{\mathbf{p},\mathbf{x}} + \dot{\mathbf{p}} \cdot \nabla_{\mathbf{p}}\, \varrho_{\mathbf{p},\mathbf{x}}, \tag{2.21}$$

which includes temporal evolution and spatial transport phenomena. In particular, the first term represents an explicit time dependence, the second a drift caused by the particles free-streaming, and the third the effects of external macroscopic forces, for example gravitational deflection.

In the following we will study in detail the flavor evolution in both SNe and Early Universe. For the moment we find useful to briefly compare the main differences in the treatment of the flavor evolution in the two cases.

1. **Early Universe**

   The evolution in time in the form of Boltzmann-like equations applied to the Early Universe, safely considered isotropic and homogeneous at large scale, reduces to

   $$\partial_t \varrho_{\mathbf{p}} = -i[\Omega_{\mathbf{p}}, \varrho_{\mathbf{p}}] + \hat{\mathcal{C}}[\varrho_{\mathbf{p}}] \ , \tag{2.22}$$

   where

   $$\partial_t \to \partial_t - Hp\, \partial_{\mathbf{p}} \tag{2.23}$$

   with H the Hubble parameter which encodes the information about the universe expansion.

   Refractive matter term: in the Early Universe there were almost equal numbers of baryons and antibaryons with an asymmetry fixed by observations to be $\eta_B \sim 10^{-10}$. Due to the charge neutrality of the Universe, the electron-positron density is expected to be of the same order and its contribution to the refractive term $\Omega^{M(0)}$, Eq. (2.11), is subdominant. It is necessary to consider the higher order which depends on the sum of the electron and positron energy densities, [Eq. (2.12)].

   Self-interaction term: in absence of a neutrino-antineutrino asymmetry $(\varrho - \overline{\varrho})$, as expected in the standard case, the only contribution is given by the second order term Eq. (2.16) $(\varrho + \overline{\varrho})$ which is subleading for the neutrino evolution, since its numerical value is small. Conversely, in the case of large neutrino asymmetries, the leading order term $\Omega_{\mathbf{p}}^{\nu\nu(0)}$ [Eq. (2.15)], becomes important and the evolution is dominated by the effect of *synchronized* oscillations, i.e. the self-potential forces all neutrino modes to follow the same oscillation pattern [66]. In the following we will discuss in details the role of neutrino asymmetry in the case of active-sterile neutrino oscillations.

Collisional term: at high temperature of the primordial plasma, this term is very important since it breaks the coherence of the neutrino ensemble. It damps the off diagonal terms of the density matrix $\varrho_{\mathbf{p}}$ and it pushes the diagonal terms towards their equilibrium distributions.

2. **Supernova**

In the case of radiating object such as the supernova, we have to include spatial transport phenomena in the EoMs. Indeed a proper description requires to consider a stationary system evolving in space instead of a homogeneous system evolving in time. Once the core of a massive star becomes gravitationally unstable, it quickly collapses, leading to a fast increase of density. The neutrinos initially trapped within a region called "neutrinosphere", are then ejected from it in according to a free streaming emission. Therefore, the evolution equations become:

$$\mathbf{v_p} \cdot \nabla_{\mathbf{x}} \varrho_{\mathbf{p,x}} = -i[\Omega_{\mathbf{p,x}}, \varrho_{\mathbf{p,x}}]\,, \tag{2.24}$$

where in the Liouville operator we ingnored an explicit temporal evolution of $\varrho_{\mathbf{p,x}}$, as well as the effect of external macroscopical forces, like the gravity. At r.h.s. we have neglected collisional terms that play no role in the SN flavor evolution.

Refractive matter term: the relevant term for the SN oscillations is given by the leading order in which the matter potential assumes the form of the Eq. (2.10). This term is trajectory dependent, inducing different oscillation phases for neutrinos traveling in different directions. This effect can be relevant in the region close to the neutrinosphere. Moreover MSW effect in supernovae can leave a peculiar imprint on the observable neutrino signal, sensitive to the propagation of the shock wave in the SN envelope.

Self-interaction tem: differently from the case of the Early Universe, in the case of SN one expects relevant flux differences among different flavors. Therefore, for the SN environment it is enough to consider the leading order in the self interaction term, Eq. (2.15), in which the non-isotropic nature of neutrino emission would lead to peculiar *multi-angle* effects in the flavor evolution. The large neutrino densities in the deepest stellar regions can result in significant coherent $\nu - \nu$ forward scatterings, which give rise to collective features for the flavor oscillations. The fate of these fascinating effects depends on the competition between the ordinary electron

matter potential and the neutrino potential itself, as we will discuss later.

Collisional term: this term is completely negligible in the SN evolution since one can separate the neutrino spectra formation problem in the scattering dominated high-density region, from the flavor evolution after the neutrino-sphere where neutrinos are free streaming.

Chapter 3

Self-induced neutrino oscillations in Supernovae

Core-collapse supernovae (SNe) represent one of the most energetic and spectacular phenomena in the Universe. They are powerful explosions which mark the violent death of massive stars ($M \gtrsim 8$ M$_\odot$) as they become unstable during the late phases of their evolution [67]. The explosion is driven by a shock wave that eventually ejects the outer mantle of the collapsing star, liberating a gravitational binding energy $E_{\rm B} \simeq 3 \times 10^{53}$ erg. Remarkably, 99% of this binding energy is carried away by neutrinos and antineutrinos of all the flavors, making a core-collapse SN one of the most powerful neutrino source. Therefore, neutrinos emitted during such a process are a promising tool to probe neutrino mass and mixing properties and to provide valuable information about SN mechanism itself [68]. The neutrino fluxes and spectra are sensitive to many details of SN physics, notably the progenitor mass, the nuclear equation of state, and the occurrence of convection inside and outside the SN core. Originating deep inside the core and passing through the mantle of the star, the neutrino flavor conversions are affected by dense matter on their road through the stellar envelope [28, 29, 69]. Moreover, in the deepest SN regions the neutrino density is so high that can dominate the flavor evolution, eventually producing a surprising collective behavior in the SN neutrino ensemble [70]. As a consequence of these effects, the SN neutrino fluxes reaching the detectors would be deeply modified with respect to the initial ones, carrying fascinating signatures of oscillation effects occurring in the deepest SN regions. Thus detection of a high-statistics neutrino signal from the next nearby SN represents a new frontier in low-energy neutrino physics and astrophysics. In this Chapter we describe the SN explosion mechanism with particular emphasis on the expectation for the initial neutrino fluxes. After that we discuss in details the supernova neutrino fla-

vor conversions, focusing particularly on the the collective effects, induced by the neutrino-neutrino interactions. This presentation is mainly based on [67, 70, 71, 72, 73, 74, 75, 76, 77] to which we address the reader for more details.

3.1 Core-collapse SN dynamics

During its life a star is kept in equilibrium by two effects operating in opposite directions: the gravitational force which tends to collapse the star and the thermal pressure which tends to expand it. In order to maintain this equilibrium the star will undergo a series of nuclear burning stages, starting with the burning of the Hydrogenum in the Helium and proceeding with heavier elements, leading to the "onion" structure with several burning shells, an expanded envelope, and a degenerate iron core (see Fig. 3.1).

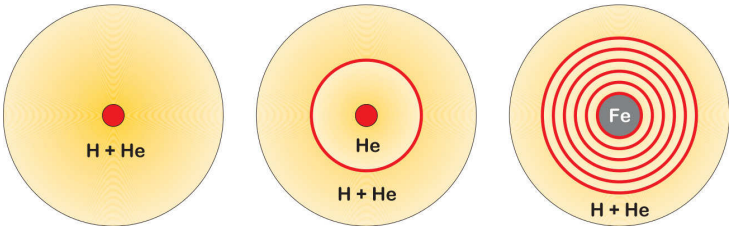

Figure 3.1: Different stages of the stellar evolution. Left : hydrogen fusion in the stellar core. Centre : helium burning star. Right: onion-structure of a massive star with an iron core and shells of lighter elements produced during the different phases of nuclear fusion.

The fate of the star is determined when the mass core reaches the Chandrasekhar limit, which is the maximum mass that can be supported by the electron degeneracy pressure. Then the gravitational pull wins over the internal pressure and the core starts to collapse, leading to a fast increase of density. Indeed, the collapsing star can not ignite nuclear fusion because iron is the nucleus with the largest binding energy. The first stage of the collapse occurs when densities of $\rho \simeq 10^{12}$ g cm^{-3} are reached and matter becomes opaque to neutrinos, due their large NC scattering cross sections on heavy nuclei. This stage is know as "neutrino trapping", since the neutrinos are confined within a "neutrinosphere" . Therefore, the collapse continues until the equation of state stiffens at about nuclear density ($\rho \sim 3 \times 10^{14}$ g cm^{-3}). At this point the inner core becomes incompressible, the implosion is suddenly halted and the core rebounces. The core bounce generates sound waves that

start propagating radially out of the inner core, producing a density, pressure, and velocity discontinuity in the flow. A hydrodynamic shock wave forms and travels outward, ejecting the outer layers.

Technically, even if the bounce and shock explosion mechanism [78, 79, 80, 67] is essentially a hydrodynamical phenomenon, the realistic numerical simulations have difficulties in triggering the explosion for a physical reason. The shock wave forms within the iron core. As it moves outward it dissipates energy by the dissociation of iron. Therefore, the shock wave stalls without driving off the stellar mantle and envelope. The standard scenario holds that the stagnating shock is revitalized by energy deposition so that enough pressure builds up behind the shock to trigger the explosion.

3.1.1 Emission of SN neutrinos

During and after the explosion, the star emits neutrinos in three main phases (Fig. 3.2).

1. *Prompt ν_e burst*: As the shock wave passes through the neutrino sphere, a ν_e burst, lasting $t \simeq 10$ ms, is released due to rapid electron capture on dissociated nuclei (deleptonization of the outer core layers) $e^- + p \to n + \nu_e$, leading to leads to a sudden rise in the luminosity up to $L = 10^{53}$ erg s^{-1}. In this phase the fluxes of the other neutrino flavors are negligible compared to ν_e.

2. *Accretion phase*: The shock wave quickly loses its energy in dissociating nuclei and stagnates at a radius of 150-200 km. Material continues to fall onto the core ("accretion shock") for the following few 100 ms and powers the emission of neutrinos and antineutrinos of all species, with a luminosity of $L = 10^{52}$ erg s^{-1} and caracterized by a strong excess of the ν_e species over the others. Pronounced hierarchy of average energies $\langle E_{\nu_x} \rangle > \langle E_{\bar{\nu}_e} \rangle > \langle E_{\nu_e} \rangle$, where x stands for any of $\nu_{\mu,\tau}$ or $\bar{\nu}_{\mu,\tau}$.

3. *Kelvin-Helmholtz cooling phase*: After the successful explosion, the remaining proto-neutron star cools by neutrino emission over about 10 s. The luminosity is approximately equipartitioned between different species $L = 3 \times 10^{51}$ erg s^{-1} and the flavor hierarchy of average energies is probably mild.

A supernova can be roughly considered as a black-body that cools via neutrino emission. Indeed, supernova simulations typically provide neutrinos emitted with "quasi-thermal" spectra. In particular, a simple analytical

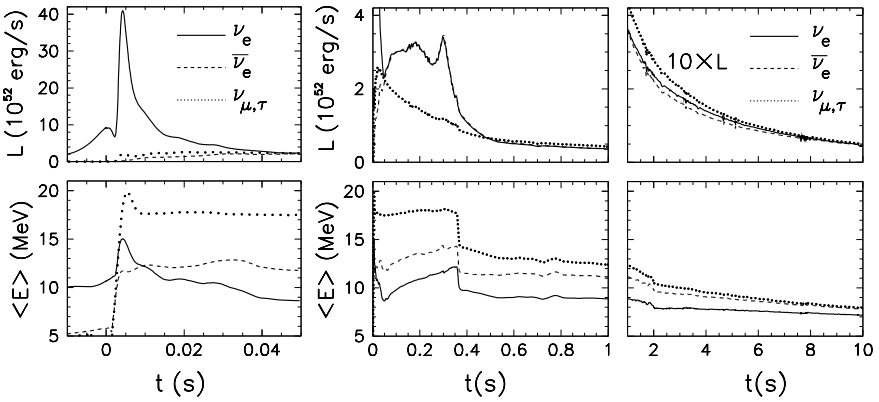

Figure 3.2: Neutrino signal of a core-collapse SN for a 10.8 $M_\odot$ progenitor according to a numerical simulation of the Basel group [81]. In this spherically symmetric simulation the explosion was triggered by hand. *Left*: Prompt neutrino burst. *Middle*: Accretion phase. *Right*: Cooling phase.

parametrization of the neutrino spectra is given in terms of the so-called "alpha-fit" [82]:

$$F_{\nu_\alpha}(E) = \frac{L_\nu}{\langle E_\nu\rangle^2}\frac{(\alpha+1)^{(\alpha+1)}}{\Gamma(\alpha+1)}\left(\frac{E}{\langle E_\nu\rangle}\right)^\alpha \exp\left[-(\alpha+1)\frac{E}{\langle E_\nu\rangle}\right] , \tag{3.1}$$

with $\langle E_\nu\rangle$ the average energy. The numerical parameter "pinch" α controls the width of the distribution,

$$\frac{\langle E^2\rangle - \langle E\rangle^2}{\langle E\rangle^2} = \frac{1}{1+\alpha} , \tag{3.2}$$

and $\alpha = 2$ corresponds to a Maxwell-Boltzmann spectrum, $\alpha > 2$ to a pinched spectrum with suppressed high- and low-energy tails, and $\alpha < 2$ to an anti-pinched spectrum. Simulations find values of α typically in the range 2-5, so the spectra are generally pinched.

The spectral characteristics evolve in time (Fig. 3.2), are expected to vary for different supernova progenitors, and depend on uncertain input physics such as the nuclear equation of state and the treatment of neutrino transport. Typically, one expects $\langle E_{\nu_e}\rangle \simeq$ 10–12 MeV, while the $\overline{\nu}_e$ energies are expected to be somewhat larger, $\langle E_{\overline{\nu}_e}\rangle \simeq$ 12–15 MeV, due to their smaller charged-current interaction rate in neutron-rich matter, allowing them to escape from deeper and hotter layers. Interactions are almost identical for ν_μ, ν_τ, and their antiparticles. They will have nearly identical primary fluxes F_{ν_x} and average energies $\langle E_{\nu_x}\rangle \simeq$ 15–18 MeV.

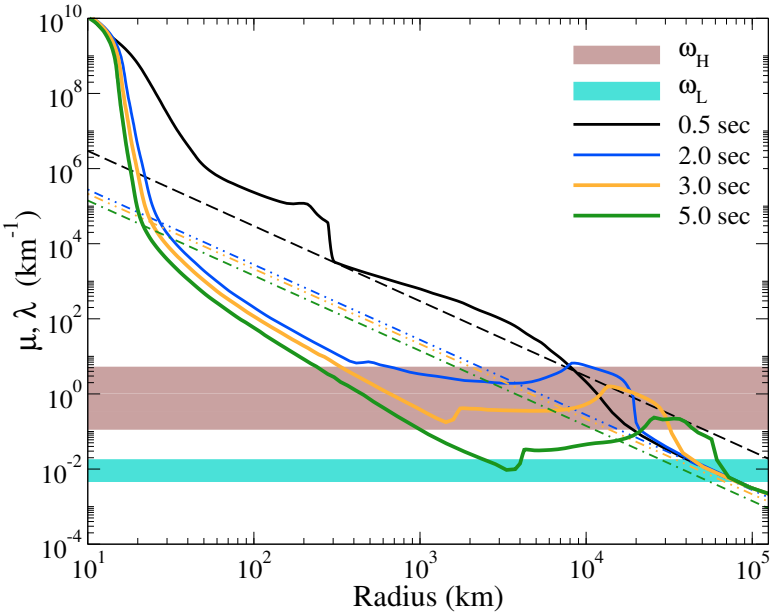

Figure 3.3: Snapshots of SN potentials for different post-bounce times. Continuous curves refer to the matter potential λ, dot-dashed to the neutrino potential μ. The horizontal bands represent the vacuum oscillation frequencies relevant for the MSW resonant conversions associated to the $\Delta m^2_{\rm atm}$ (ω_H) and to the $\Delta m^2_{\rm sol}$ (ω_L), respectively (see the text for details).

3.2 Supernova potential profiles and neutrino flavor conversions

Effects of flavor conversions on supernova neutrinos depend on the different densities encountered by neutrinos in their propagation in the stellar envelope. In Fig. 3.3 is represented a snapshot of the different interaction potentials associated with different supernova densities obtained from the Basel-Darmstadt simulations of a 10.8 $M_\odot$ SN progenitor for different post-bounce times [81]. As we will discuss in the following, self-induced neutrino oscillations, associated with the neutrino-neutrino interactions are related to the neutrino number densities. In Fig. 3.3 is represented the neutrino-neutrino potential

$$\mu = \sqrt{2} G_F [n_{\nu_e} - n_{\overline{\nu}_e}] = \frac{1}{4\pi r^2} \left(\frac{L_{\nu_e}}{\langle E_{\nu_e} \rangle} - \frac{L_{\overline{\nu}_e}}{\langle E_{\overline{\nu}_e} \rangle} \right) \quad , \tag{3.3}$$

The non-electron neutrino has not included since it cancels between ν_x and $\bar{\nu}_x$. We realize that this neutrino potential decrease in time as the SN cools.

Matter effects on SN neutrinos depend on the potential

$$\lambda = \sqrt{2} G_F n_e \ , \tag{3.4}$$

where n_e is the net electron density n_e encountered by neutrinos in their propagation. The numerical values of μ and λ from the previous two expressions are quoted in km^{-1}, as appropriate for the SN case. From Fig. 3.3, we realize that the SN electron density profile is non-monotonic and time-dependent and presents an abrupt discontinuity, corresponding to the position of the *shock-front*. In general the shock wave, while propagating outwards at supersonic speed, leaves behind a rarefaction zone, and creates a high-density front with a sharp density drop (down to the static value). The two horizontal strips represent the regions associated with MSW resonant flavor conversions with the atmospheric oscillation frequency ω_H (violet band) and with the solar one ω_L (light blue) for an energy range $E \in [1 - 50]$ MeV.

From the comparison of the different densities we realize that in the deepest SN regions ($r < 10^3$ km) $n_\nu \gg n_e$, except during the accretion phase ($t < 0.5$ s). We will see that when the neutrino density dominates over the matter one (as during the cooling phase) self-induced flavor conversions would develop without any hindrance.

Conversely, at larger radii, the flavor conversions will be dominated by the ordinary matter effects. The L-resonance is always adiabatic. The H-resonance is adiabatic for values of θ_{13} as large as the one recently measured [7, 8], except at the shock-front where strong non-adiabatic conversions occur [83]. The H resonance takes place in the neutrino sector for normal mass hierarchy and in the anti-neutrino one for inverted mass hierarchy. Therefore, in principle, the neutrino burst is sensitive to the neutrino mass hierarchy.

Neglecting for the moment the self-induced effects, the flux arriving at Earth relevant for the detection can be expressed in terms of energy-dependent ν_e survival probabilities $p(E)$ in the form [69]

$$F_{\nu_e} = p(E) F^0_{\nu_e}(E) + [1 - p(E)] F^0_{\nu_x}(E), \tag{3.5}$$

where 0 indicates the initial neutrino fluxes. An analogous expression exists for $\bar{\nu}_e$ with survival probabilities $\bar{p}(E)$. In particular, considering for simplicity a static SN matter profile one finds $(p, \bar{p}) = (0, \cos^2\theta_{12})$ in normal mass hierarchy, and $(p, \bar{p}) = (\sin^2\theta_{12}, 0)$ in inverted mass hierarchy [69].

3.3 Self-induced flavor evolution of SN neutrinos

As already described in the Chapter 2, the evolution equations for the SN neutrino ensembles are given by

$$\mathbf{v_p} \cdot \nabla_x \varrho_{\mathbf{p},\mathbf{x}} = -i[\Omega^{\rm vac}_{\mathbf{p}}, \varrho_{\mathbf{p},\mathbf{x}}] - i[\Omega^{\rm ref}_{\mathbf{p},\mathbf{x}}, \varrho_{\mathbf{p},\mathbf{x}}], \tag{3.6}$$

where the vacuum term for relativistic neutrinos is represented by $\Omega^{\rm vac}_{\mathbf{p}} = {\rm diag}(m_1^2, m_2^2, m_3^2)/2p$, while the refractive terms are:

$$\Omega^{\rm ref}_{\mathbf{p},\mathbf{x}} = \lambda \mathsf{L} + \sqrt{2}\, G_{\rm F} \int \frac{{\rm d}^3\mathbf{q}}{(2\pi)^3} \left(\varrho_{\mathbf{q},\mathbf{x}} - \bar{\varrho}_{\mathbf{q},\mathbf{x}}\right) (1 - \mathbf{v_q} \cdot \mathbf{v_p}) \,. \tag{3.7}$$

The ordinary refractive matter effect is represented by $\lambda = \sqrt{2}\, G_{\rm F}(n_{e^-} - n_{e^+})$ and $\mathsf{L} = {\rm diag}(1,0,0)$ in the weak interaction basis. The second term at r.h.s. of the Eq. (3.7) describes the self-interactions where the factor $(1 - \mathbf{v_q} \cdot \mathbf{v_p}) = (1 - \cos\theta_{\mathbf{p}q})$ comes from the current-current nature of the weak interaction, and $\mathbf{v_p} = \mathbf{p}/p$ is the velocity. The angular term averages to zero if the gas is isotropic. Different approximations have been proposed in literature in order to simplify this challenging problem. In the following sections we will present different toy-models at increasing levels of complexity, proposed to capture different aspects of this flavor dynamics.

3.3.1 Polarization vectors formalism for two-flavor system

Since ν_μ and ν_τ behave equally in core collapse SN, neutrino oscillations can be described at first approximation in two-flavor scenario. Therefore, we expand all the 2×2 matrices in the EoMs in terms of the 2×2 unit matrix I and the Pauli matrices σ. All the quantities involved in the EoMs can written as [72]

$$\begin{aligned}
\rho_{\mathbf{p}} &= \tfrac{1}{2}\big(f_{\mathbf{p}}\mathsf{I} + \mathbf{P_p} \cdot \boldsymbol{\sigma}\big) \,, \\
\bar{\rho}_{\mathbf{p}} &= \tfrac{1}{2}\big(\bar{f}_{\mathbf{p}}\mathsf{I} + \bar{\mathbf{P}}_{\mathbf{p}} \cdot \boldsymbol{\sigma}\big) \,, \\
\Omega^{\rm vac}_{\mathbf{p}} &= \tfrac{1}{2}\big(\omega_0 \mathsf{I} + \omega_{\mathbf{p}}\, \mathbf{B} \cdot \boldsymbol{\sigma}\big) \,, \\
\Omega^{\rm M}_{\mathbf{p}} &= \tfrac{\lambda}{2}\big(\mathsf{I} + \mathbf{L} \cdot \boldsymbol{\sigma}\big) \,, \\
\Omega^{\nu\nu}_{\mathbf{p}} &= \tfrac{\mu}{2}\big(\mathsf{I} + \mathbf{V} \cdot \boldsymbol{\sigma}\big) \,,
\end{aligned} \tag{3.8}$$

in which we have only considered the leading terms in refraction and self-refraction. The vectors $\mathbf{P_p}$ and $\bar{\mathbf{P}}_{\mathbf{p}}$ are the ν and $\bar{\nu}$ polarization vectors in

flavor space. The coordinate system in flavor space is chosen in such a way that in an ensemble of pure electron neutrinos, the z-component of $\mathbf{P_p}$ corresponds to the electron neutrino occupation number, and the total number density of electron neutrinos would be $n_{\nu_e} = \int P^z_{\mathbf{p}}\ d^3\mathbf{p}/(2\pi)^3$, whereas an orientation in the negative z-direction corresponds to a combination of muon and tau neutrinos, which we denote ν_x. We remark that $\mathbf{P_p} = 0$ means that it contains an incoherent equal mixture of ν_e and ν_x. In this formalism, the survival probability of ν_e is $[1 + P_z]/2$ [72].

Moreover, we have $\omega_0 = m_1^2 + m_2^2$ and vacuum oscillations are determined by the mass differences and vacuum mixing angle θ, so that

$$\begin{aligned} \omega_{\mathbf{p}} &= (m_1^2 - m_2^2)/2p\,, \\ \mathbf{B} &= (\sin 2\theta, 0, \cos 2\theta)\,. \end{aligned} \tag{3.9}$$

where the unit vector $\mathbf{B}$ is oriented in the the mass eigenstate direction in flavor space, such that $\mathbf{B} \cdot \mathbf{L} = \cos 2\theta$. In an ordinary medium composed by electrons and positrons, $\mathbf{L}$ is a unit vector in the positive z-direction $\mathbf{L} = \mathbf{e}_z$ and λ is an effective electron density, i.e., the density of electrons minus that of positrons, $\lambda = \sqrt{2}G_F n_e$. Finally, we define the parameter $\mu = \sqrt{2}G_F n_\nu$ which normalizes the neutrino-neutrino interaction strength, given by:

$$\mathbf{V} = \int \frac{\mathrm{d}^3\mathbf{q}}{(2\pi)^3}(1 - \mathbf{v_q} \cdot \mathbf{v_p})(\mathbf{P_q} - \overline{\mathbf{P}}_\mathbf{q}). \tag{3.10}$$

As further approximation, instead of considering the spatial evolution of neutrinos emitted from the neutrino sphere, we consider an homogeneous and isotropic neutrino gas evolving along an affine coordinate t. Then, the neutrino and antineutrino EOMs assume the form:

$$\begin{aligned} \partial_t \mathbf{P_p} &= [+\omega\mathbf{B} + \lambda\mathbf{L} + \mu\mathbf{V}] \times \mathbf{P_p}\,, \\ \partial_t \overline{\mathbf{P}}_p &= [-\omega\mathbf{B} + \lambda\mathbf{L} + \mu\mathbf{V}] \times \overline{\mathbf{P}}_p\,. \end{aligned} \tag{3.11}$$

In the limit of isotropic distributions one obtains the so-called "single-angle" self-refractive potential:

$$\mathbf{V} = \left(\mathbf{J} - \overline{\mathbf{J}}\right)\ , \tag{3.12}$$

where

$$\mathbf{J} = \int \frac{\mathrm{d}^3\mathbf{p}}{(2\pi)^3}\mathbf{P_p}\ , \quad \overline{\mathbf{J}} = \int \frac{\mathrm{d}^3\mathbf{p}}{(2\pi)^3}\overline{\mathbf{P}}_\mathbf{p}. \tag{3.13}$$

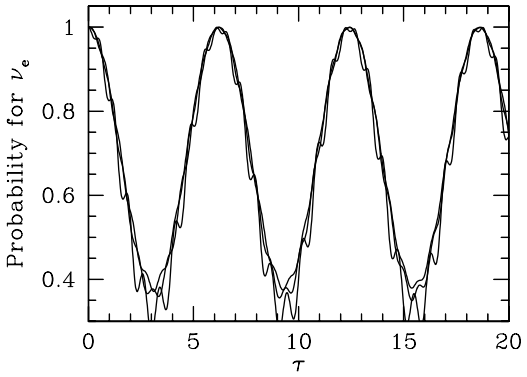

Figure 3.4: Synchronized neutrino oscillations: evolution of the ν_e survival probability for three values of the neutrino energy in presence of large $\nu - \nu$ interaction term. Here $\tau = (\Delta m^2/2E)t$. Figure taken from [84] .

3.3.2 Single-angle approximation

We want to show some types of collective behaviors that can arise in dense neutrino gases in the single angle approximation for few representative cases.

Gas of only ν. We consider as first case a dense neutrino gas composed of only ν_e. In the presence of only vacuum oscillations, modes with different energies would oscillate with different oscillation frequency ω, leading to what is called *kinematical decoherence*. If now one switches on a large $\nu - \nu$ interaction term $\mu \gg \omega$, one realize that the different modes are locked to oscillate together as a single-energy mode (Fig. 3.4) whose precession motion is described by [84]

$$\partial_t \mathbf{J} = \omega_{\rm synch} \mathbf{B} \times \mathbf{J} \ , \tag{3.14}$$

with oscillation frequency

$$\omega_{\rm synch} = \left\langle \frac{\Delta m^2}{2E} \right\rangle = \frac{1}{N_\nu} \sum_{j=1}^{N_\nu} \frac{\Delta m^2}{2E_j} \ , \tag{3.15}$$

where we have assumed a discrete ensemble of N_ν neutrinos. This is the first example of collective oscillations behavior, called *synchronized oscillations*. A system consisting of ν and $\overline{\nu}$ behaves in the same way of the one constituted

by ν only, except that the role of $\mathbf{J}$ is played by $\mathbf{V}$, and $\omega_{\rm synch}$ is given by [84]

$$\omega_{\rm synch} = \frac{1}{|\mathbf{V}|}\left(\sum_{j=1}^{N_\nu}\frac{\Delta m^2}{2p_j}\,\hat{\mathbf{V}}\cdot\mathbf{P}_j + \sum_{k=1}^{N_{\bar\nu}}\frac{\Delta m^2}{2p_k}\,\hat{\mathbf{V}}\cdot\overline{\mathbf{P}}_k\right). \tag{3.16}$$

Equal densities of ν and $\overline{\nu}$ We consider now the simplest system initially composed of equal densities of pure ν and $\overline{\nu}$. In this case, since $\mathbf{V}$=0, synchronized oscillations are not possible. However, we will see that depending on the flavor content and on the mass hierarchy this system can be unstable in the flavor space, experiencing significant flavor conversions.

1. *Vacuum + self-interaction (μ =const)*

   We consider a system consisting of only ν_e and $\overline{\nu}_e$ with a small vacuum mixing angle ($\theta \ll 1$) and a strong self-interaction term ($\mu \gg \omega$). We neglect the matter term λ in the EoMs [Eq. (3.11)] and for simplicity we consider a mono-energetic ν ensemble. If we consider inverted mass hierarchy [1], the evolutions of P_z and $\overline{P}_z$ are shown in the Fig. 3.5.

   Initially, both P_z and $\overline{P}_z$ stay put in their initial flavor state. After some time they flip completely, but immediately they return to their original state, leading to periodic motion, with complete and simultaneous conversion of ν_e and $\overline{\nu}_e$ to ν_x and $\overline{\nu}_x$ and back (*pair conversions* of $\nu_e\overline{\nu}_e \leftrightarrow \nu_x\overline{\nu}_x$) which conserve the total flavor content. On the other hand, for the normal hierarchy the system is totally stable and no flavor conversions take place. It is important to comment that if we would have taken an ensemble composed of only ν_μ and $\overline{\nu}_\mu$, we would have found large flavor conversions in normal hierarchy, instead of the inverted one. Indeed, the unstable case is when the initial ensemble consists of that flavor which is dominated by the heavier mass eigenstate.

   This evolution can be explained in analogy to a pendulum in flavor space [72, 85]: for normal hierarchy the system initially sets near the minimum of the pendulum potential and is therefore blocked leading to no visible effects. Conversely, in the inverted hierarchy the evolution starts with the system close to the maximum of the potential in an unstable equilibrium and so it moves to situation of minimum, leading to this periodic *pendular* conversions. The pendular period (the separation between dips), scales logarithmically with the small vacuum

[1] In the 2-ν formalism of Sec. 3.3.1, the inverted mass hierarchy is obtained sending $\theta \to \pi/2 - \theta$ [72]

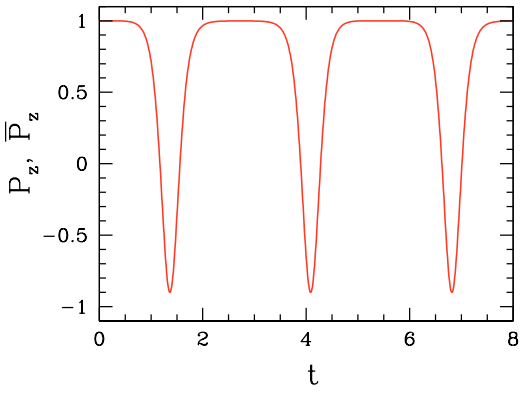

Figure 3.5: Evolutions of P_z and $\overline{P}_z$ for $\theta = 0.01$, $\omega = 1$, and strong neutrino-neutrino interaction $\mu = 10$. Figure taken from [72].

mixing angle. Indeed it is intriguing that the sort of flavor conversions being associated with an *instability* in flavor space take place also for very small values of the mixing angle ($\theta < 10^{-10}$) [86].

2. *Vacuum + matter + self-interaction (μ =const)*

   Taking into account also the matter term, the evolution equations in matter [Eq. (3.11)], can be reduced to the ones in vacuum, going to the frame co-rotating around the **L**-direction, with a time dependent **B** [72]:

$$\mathbf{B} = \begin{pmatrix} \sin(2\theta_0)\cos(-\lambda t) \\ \sin(2\theta_0)\sin(-\lambda t) \\ -\cos(2\theta_0) \end{pmatrix}. \tag{3.17}$$

   In this picture **B** rotates around the z-direction with frequency $-\lambda$. If this rotation is faster than all other frequencies, the transverse components of **B** would average to zero, leaving us with $\langle \mathbf{B} \rangle$ along the z-axis, i.e., an effectively vanishing mixing angle and no flavor conversions. However this fast rotating transverse components are still enough to trigger conversions, with a matter suppressed effective mixing angle, extending logarithmically the pendular period, as in Fig. 3.6.

3. *Vacuum + self-interaction (μ varying)*

   In order to mimic more realistically the SN scenario always with a toy-model, one has to consider a self-induced potential μ declining with distance. In particular, there is a factor scaling like r^{-2} from the geometrical neutrino flux dilution at which adds another r^{-2} factor due to the collinearity suppression, coming from the average on $\langle 1 - \mathbf{v_q} \cdot \mathbf{v_p} \rangle$

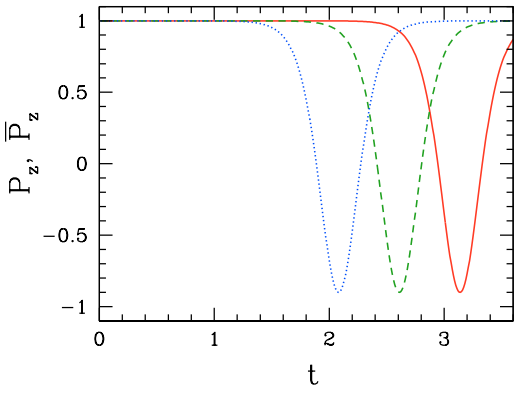

Figure 3.6: Evolution of P_z and $\overline{P}_z$ for the same parameters of the Fig. 3.5 and different strengths of background matter: $\lambda = 10^2$ (blue/dotted line), $\lambda = 10^3$ (green/dashed line), $\lambda = 10^4$ red/solid line. Figure taken from [72].

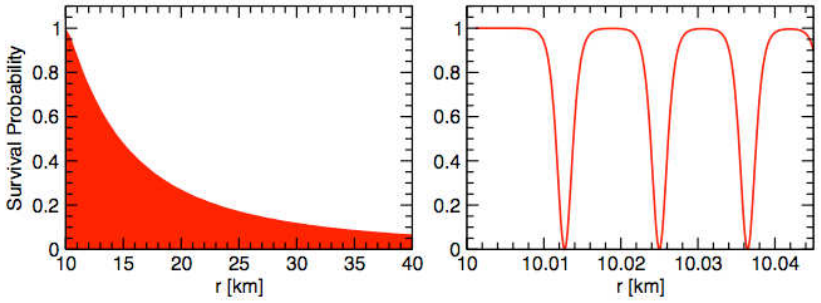

Figure 3.7: Survival probabilities for ν_e or ν_e in presence of a radial-dependent $\nu - \nu$ potential term with $\mu_0 = 7 \times 10^5$ km^{-1} and $\sin 2\theta = 0.001$ Figure taken from [72].

factor, leading essentially to an r^{-4} decline for the self-interaction term [72]. In this case, the evolution P_z and $\overline{P}_z$ for a ν_e and $\overline{\nu}_e$ ensemble in inverted hierarchy are shown in Fig. 3.7. The oscillation amplitude has declined as a function of radius leading to a complete flavor conversion caused by the pendular effect. Comparing this result with the case of constant density μ and using again the pendulum analogy, one can understand that by reducing μ, also the energy of the system is reduced and therefore, after each oscillation, the pendulum will not come back to its initial position (the maximum of the potential) but to a lower

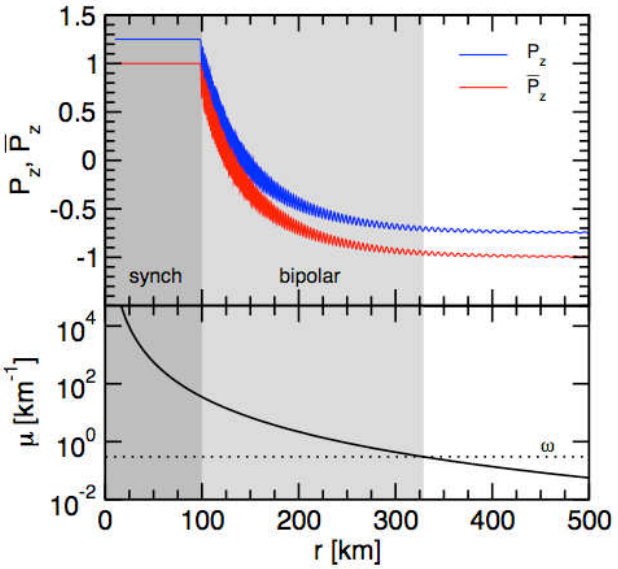

Figure 3.8: Evolution of P_z (blue curve) and $\overline{P}_z$ (red curve) in presence of neutrino-antineutrino fluxes asymmetry $\epsilon = 0.75$ and $\sin 2\theta = 0.001$. The grey shaded bands represent the synchronization (dark) and pendular regions (light). Figure taken from [87].

one, which will be closer and closer to the rest point as μ decreases.

ν and $\overline{\nu}$ asymmetry. In addition to the radial dependence of μ, another feature to characterize the SN neutrino case is the initial neutrino-antineutrino asymmetry.

As described in the Sec. 3.1.1 one expects some hierarchy among the neutrino number fluxes, in particular, during the accretion phase, $F_{\nu_e} > F_{\overline{\nu}_e} > F_{\nu_x}$. This feature is taken into account imposing the initial conditions $\overline{P}_z = 1$ and $P_z = 1 + \epsilon$, where the asymmetry parameter ϵ, representing the electron neutrino excess coming from the deleptonization of the collapsed core, is defined as:

$$\epsilon = \frac{F_{\nu_e} - F_{\overline{\nu}_e}}{F_{\nu_e} - F_{\nu_x}} \tag{3.18}$$

with $F_{\nu_x} = F_{\overline{\nu}_x}$. The evolution of the polarization vectors in this case is shown in the Fig. 3.8 where we have considered a small vacuum mixing angle and inverted mass hierarchy. From this figure, it is possible to distinguish three different regimes of evolution, corresponding to different relative strengths of

μ with respect to the vacuum frequency ω:

-*syncronized oscillations* ($\mu > \mu_{\rm syn}$), right behind the neutrino sphere and up to about 100 km, corresponds to the first stage of evolution, where synchronized oscillations occur. Since the mixing angle is small, ν e $\overline{\nu}$ stay in their original flavor up to a distance called $r_{\rm syn}$. The condition for the synchronized oscillations is given by [72, 73]:

$$\mu_{(r_{\rm syn})} = \frac{2\omega}{(1-\sqrt{1+\epsilon})^2}. \tag{3.19}$$

-*pendular oscillations* ($\mu_{\rm syn} < \mu < \omega$) represent the second stage of evolution characterised by of pendular conversions, where complete pair transformation are developed, conserving the initial flavor lepton asymmetry.

-*vacuum oscillations* ($\mu < \omega$) the neutrino-neutrino interactions cease and ordinary oscillations take place, where the normal matter can play an important role via the usual MSW effect.

Multi-energy spectral splits Finally, we have to consider that in SN are emitted neutrinos of all the flavors with continuos energy distributions. In Fig. 3.9 we show the flavor evolution in inverted mass hierarchy of the integrated polarization vectors $\mathbf{J}$ and $\bar{\mathbf{J}}$ [Eq. (3.13)] for representative supernova conditions as the ones considered in [74]. We realize the the behavior of J_z and $\bar{J}_z$ is similar to the single-flavor and single-energy cases shown before. At the same time, antineutrinos tend to totally invert the polarization vector ($\bar{\mathbf{J}} \to -\bar{\mathbf{J}}$), in order to minimize their potential energy. Neutrinos also try to reverse their global polarization vector when the alignment approximation breaks down at $r \gtrsim 100$ km and so $\mathbf{J}$ decreases.

In Fig. 3.10 we show the corresponding evolution of the individual polarization vectors P_z (upper panel) and $\bar{P}_z$ (lower panel) as a function of r for different representative energy values. One realizes that the evolution of each P_z or $\bar{P}_z$ depends on energy. For neutrinos (upper panel in Fig. 3.10), one can distinctly see the occurrence of *spectral split* around a critical energy $E_c \simeq 7$ MeV. For curves at $E > E_c$, P_z ends up at the same initial value, while the curves at $E > E_c$ show the expected inversion $P_z \to -P_z$. For antineutrinos, as expected, (lower panel in Fig. 3.10), all curves present complete polarization reversal ($\bar{P}_z \to -\bar{P}_z$). We will show in Sec. 3.4 how these behaviour of the polarization vectors would imprint peculiar spectral splits in the oscillated SN neutrino fluxes.

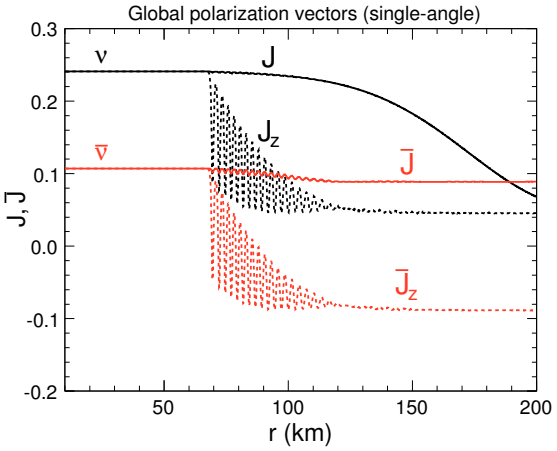

Figure 3.9: Single-angle simulation in inverted hierarchy: modulus and z-component of the global polarization vector $\mathbf{J}$ and $\overline{\mathbf{J}}$, as a function of radius. Figure taken from [74].

3.3.3 Self-induced and matter-induced multi-angle effects

The main complication in the self-induced flavor evolution for SN neutrinos with respect to the toy models discussed before, is that the flux of neutrinos emitted from a SN core is not isotropic. The current-current nature of the weak-interaction Hamiltonian implies a term proportional to $(1-\mathbf{v_p}\cdot\mathbf{v_q})$ for the interaction energy between neutrinos with momenta $\mathbf{p}$ and $\mathbf{q}$, where $\mathbf{v_p}$ is the neutrino velocity (see Eq.(3.7)). In the non-isotropic medium this velocity-dependent term would not average to zero, leading to a different refractive index for neutrinos which propagate on different trajectories. We have then the so-called "multi-angle effects", which challenge the occurrence of the coherent oscillation behavior for different neutrino modes [88]. In [89] it has been shown that in an anisotropic dense neutrino gas initially composed only of ν_e and $\bar{\nu}_e$ with equal flavors, instead of the pendular oscillations found for an isotropic ensemble, multi-angle effects would be responsible for *flavor decoherence*, leading to a flux equilibration among electron and non-electron (anti)neutrino species. On the other hand in the presence of important flavor asymmetries between ν_e and $\bar{\nu}_e$ the multi-angle effects are suppressed [73]. Therefore, in order to have a realistic characterization of these effects in the context of the SN neutrino flavor evolution, it is necessary to perform a numerical study of the equations of motion [Eq. (3.6)] for time evolving SN ν

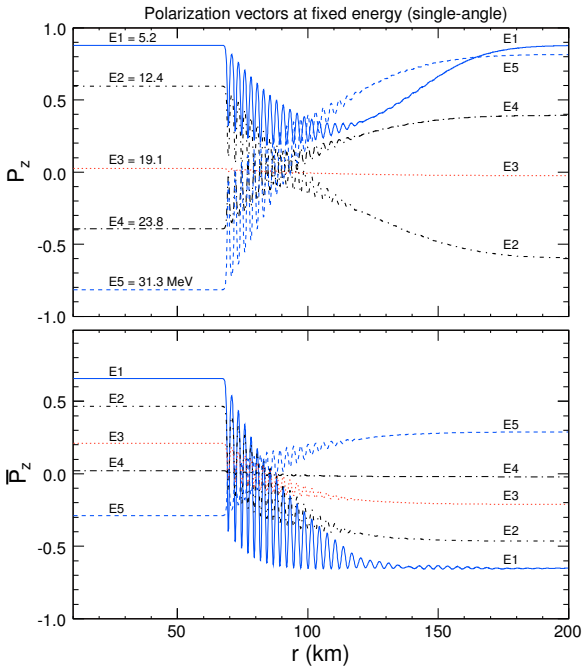

Figure 3.10: Single-angle simulation in inverted hierarchy: z-component of the polarization vector P_z (upper panel) $\overline{P}_z$ (lower panel) as a function of radius, for five representative values of the energy. Figure taken from [74].

fluxes.

As discussed in Sec. 3.3, the complete set of equations of motion for neutrinos streaming-off a supernova core involves a space evolution in a quasi-stationary situation described by partial differential equations [Eq. (3.6)]. This problem has never been solved till now in its full complexity. However, since few years have been developed the first large-scale "multi-angle" simulations of the flavor evolution in the so-called "bulb model" [77]. The basic assumptions adopted in this model are the following:

- Neutrinos are emitted uniformly and half-isotropically (i.e. with all the outward-going modes occupied, and all the back-ward going modes empty) from the surface of a spherical neutrinosphere, like in a black-body.

- The half-isotropical neutrino angular distributions are assumed energy and flavor-independent.

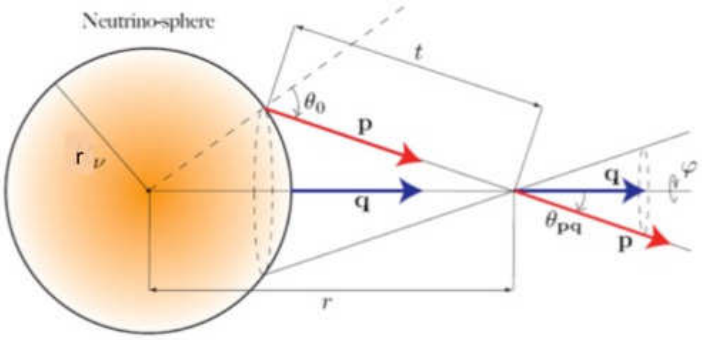

Figure 3.11: The geometrical picture of the neutrino bulb-model.

- Azimuthal symmetry in the SN is assumed, i.e. physical conditions only depend on the distance r from the center of the star.

Under the assumption of the azimuthal symmetry one can reduce the general partial differential equations [Eq. (3.6)] into a ordinary differential equations problem, projecting the evolution along the radial direction, i.e. $\mathbf{v_p} \cdot \nabla_\mathbf{x} \to v_r d/dr$. The geometry of the bulb-model is represented in Fig. 3.11. Considering a neutrino emitted at an angle θ_0 relative to the radial direction. Its radial velocity is

$$v_{r_\nu} = \cos\theta_0 \,. \tag{3.20}$$

At $r > r_\nu$, the angle of the trajectory relative to the radial direction is given by simple geometry to be [77]:

$$r_\nu \sin\theta_0 = r \sin\theta_{\mathbf{pq}} \,. \tag{3.21}$$

Therefore, the radial velocity at r is

$$v_{u,r} = \cos\theta_{\mathbf{pq}} = \sqrt{1 - \frac{r_\nu^2}{r^2}\, u} \tag{3.22}$$

where we have introduced

$$u = 1 - v_{r_\nu}^2 = \sin^2\theta_{r_\nu} \,, \tag{3.23}$$

and r_ν is the radius of the neutrino-sphere.

For a blackbody-like emission the flux modes are uniformly distributed in the interval $0 \leq u \leq 1$. For the polarization vectors labeled in function of the u angular variable, $\mathbf{P}_{u,r}$ and $\overline{\mathbf{P}}_{u,r}$, the EoM becomes [73]:

$$\partial_r = \mathbf{H}_{u,r} \times \mathbf{P}_{u,r} \,, \tag{3.24}$$

where the Hamiltonian is

$$\mathbf{H}_{u,r} = \frac{\omega\mathbf{B} + \lambda_r \mathbf{L}}{v_{u,r}} + \mu_r \left(\frac{\mathbf{D}_r}{v_{u,r}} - \mathbf{F}_r \right) . \tag{3.25}$$

For antineutrinos we have, as always, $\omega \to -\omega$. The global density and flux polarization vectors are respectively

$$\begin{aligned} \mathbf{D}_r &= \int_0^1 \mathrm{d}u \, \frac{\mathbf{P}_{u,r} - \overline{\mathbf{P}}_{u,r}}{v_{u,r}} , \\ \mathbf{F}_r &= \int_0^1 \mathrm{d}u \, \left(\mathbf{P}_{u,r} - \overline{\mathbf{P}}_{u,r} \right) , \end{aligned} \tag{3.26}$$

using the normalization $\int_0^1 \mathrm{d}u \, \bar{\mathbf{P}}_{u,r} = 1$ and $\int_0^1 \mathrm{d}u \, \mathbf{P}_{u,r} = 1 + \epsilon$. The matter coefficient

$$\lambda_r = \sqrt{2} \, G_{\mathrm{F}} [n_{e^-}(r) - n_{e^+}(r)] \tag{3.27}$$

encodes the effective electron density at radius r whereas the $\nu - \nu$ potential is given by:

$$\mu_r = \mu_{r_\nu} \, \frac{r_\nu^2}{r^2} . \tag{3.28}$$

Here $\mu_{r_\nu} = \sqrt{2} G_F [n_{\bar{\nu}_e}(r_\nu) - n_{\bar{\nu}_x}(r_\nu)]$, where $n_{\bar{\nu}_e}$ and $n_{\bar{\nu}_x}$ are respectively the electron and the non-electron antineutrino densities at the neutrinosphere. Neglecting for the moment the matter effects, i.e. putting $\lambda_r = 0$ we see that the presence of the trajectory-dependent term $v_{u,r}$ in the neutrino-neutrino interaction term in Eq. (3.25) leads to the multi-angle effects in the self-induced oscillations. Indeed, as already said before, if the flavor asymmetry ϵ between neutrinos and antineutrinos in small, it can rapidly lead to flavor decoherence in the neutrino ensemble.

Considering now also the matter term, we realize that it also contain a multi-angle effect due to the factor $v_{u,r}$. It has been shown in [75] that self-induced flavor conversions are not affected by this matter effect if

$$n_{e^-} - n_{e^+} \ll n_{\bar{\nu}_e} - n_{\bar{\nu}_x} \ . \tag{3.29}$$

Conversely, if $n_{e^-} - n_{e^+} \gg n_{\bar{\nu}_e}$, the multi-angle matter effects can produce a large spread in the oscillation frequencies of neutrinos travelling on different trajectories, blocking the self-induced flavor conversions. Finally, when $n_{e^-} - n_{e^+} \sim n_{\bar{\nu}_e} - n_{\bar{\nu}_x}$, it can produce a matter-induced multi-angle decoherence in the neutrino ensemble. According to realistic SN models, matter density is expected to dominate over the neutrino one during the early accretion phase. At this regard, in Chapter 4 we will discuss in details the matter suppression of collective oscillations, during the accretion phase.

3.4 Self-induced spectral splits during the different supernova phases

In the bulb-model first large-scale multi-angle simulations have been performed in 2006 in the seminal work by [77]. Their results represented a major breakthrough in the characterization of self-induced effects for supernova neutrinos and stimulated a torrent of activities to characterize many aspects of this intriguing flavor dynamics. In this context, different groups developed independent multi-angle simulations (see, e.g. [73, 74]) that confirmed the seminal findings of Duan and Fuller [77] and explored the dependence of the flavor evolution on the initial supernova neutrino fluxes. Many surprises and unexpected results were found with a strong dependence on many details (i.e. neutrino flavor asymmetries, angular distributions, three-flavor effects) and at the moment a complete picture of the self-induced flavor conversions in SNe is still missing. However, following [76] we can summarize the most important results of the self-induced flavor conversions in the different SN phases as follow:

- *Neutronization burst.* As shown in Fig. 3.2, during this phase one expects an excess of ν_e over $\bar{\nu}_e$ and a deficit of ν_x over $\bar{\nu}_e$. Under this situation, the pendular flavor conversions, proceeding through pair productions of $\nu_e\bar{\nu}_e \to \nu_x\bar{\nu}_x$ are not possible [72]. Therefore, only synchronized oscillations occur, with no relevant effect of flavor conversion, since the in-medium mixing angle is small. Multi-angle effects are also negligible.[2]

- *Accretion phase.* One expects a large excess of electron neutrino species over non-electron ones. As an example of this situation, in Figs. 3.12 and 3.13 is considered the three-flavor flavor evolution in inverted mass hierarchy for a flux ordering $\Phi^0_{\nu_e} : \Phi^0_{\bar{\nu}_e} : \Phi^0_{\nu_x} = 2.40 : 1.60 : 1.0$. As wee will see in Chapter 4, during the accretion phase the dense matter can dominate over the neutrino density, suppressing the self-induced flavor conversions. However, for the moment we are neglecting this effect, assuming $\lambda_r = 0$. In particular Figure 3.12 refers to the single-angle flavor evolution, while Fig. 3.13 show the multi-angle case. In the upper panels are represented the initial ν_e fluxes (dashed curves) and the

[2] A different situation could be encountered in the case of low-mass SNe with an oxygen-neon-magnesium core. In this situation the profile of the matter density can be very steep. Then, the usual MSW matter effect occur within the region of high neutrino densities close to the neutrino sphere. Therefore, self-induced flavor conversions will be possible at low-radii [90, 91].

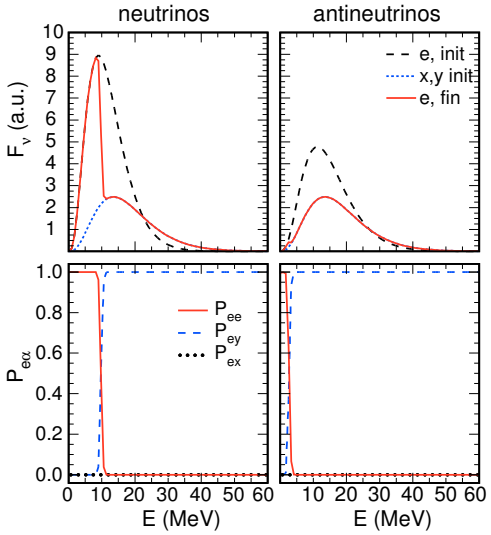

Figure 3.12: Accretion phase: 3-flavor evolution in the single-angle case and in inverted mass hierarchy for neutrinos (left panels) and antineutrinos (right panels). Upper panels: initial energy spectra for ν_e (long-dashed curve) and $\nu_{x,y}$ (short-dashed curve) and for ν_e after collective oscillations (solid curve). Lower panels: probabilities P_{ee} (solid red curve), P_{ey} (dashed blue curve), P_{ex} (dotted black curve). Figure taken from [76].

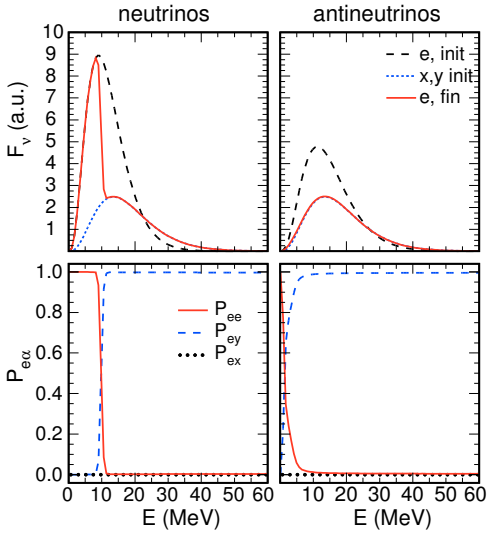

Figure 3.13: The same of the Fig. 3.12 but in the multi-angle case. Figure taken from [76].

final ones for ν_e and $\nu_{x,y}$ where $\nu_{x,y}$ are linear combinations of the $\nu_{\mu,\tau}$ fluxes. In the lower panels are represented the conversion probabilities P_{ee}, P_{ey}, P_{ex}. One can see that the final $\bar{\nu}_e$ flux is completely *swapped* with respect to the initial one, while the final ν_e flux presents a peculiar spectral *split* at $E \simeq 10$ MeV, being swapped to ν_y at higher energy. From the conversion probabilities we realize that the flavor conversions occur in the 2ν $(e-y)$ sub-system associated with $\Delta m^2_{\rm atm}$ and θ_{13}. From the comparison with the multi-angle case, we see that these effects play a sub-leading role, being suppressed by the large flavor hierarchy of the accretion phase. Finally, we comment that in normal mass hierarchy no self-induced flavor conversions occur.

- *Cooling phase*. In this case one expect a less pronounced flavor hierarchy among the different species. We consider here $\Phi^0_{\nu_e} : \Phi^0_{\bar{\nu}_e} : \Phi^0_{\nu_x} = 0.85 : 0.75 : 1.0$. Figures and 3.14 and 3.15 are in the same format of Figs. 3.12 and 3.13 for the accretion phase. We realize that differently from the accretion phase, *multiple spectral splits* are present in both neutrino and antineutrino channel. Moreover, three-flavor effects associated with $(e - x)$ conversions in the $\Delta m^2_{\rm sol}$ and θ_{12} sector are also relevant. Conversely, in the multi-angle case, this three-flavor dynamics is suppressed. Moreover, the spectral swaps and splits are less pronounced, as due to some amount of multi-angle decoherence in the flavor conversions. It has been shown in [76] that further reducing the flavor asymmetry, complete decoherence would occur. Finally, we mention that for the flux ordering of the cooling phase also in normal hierarchy spectral splits and swap can occur [92].

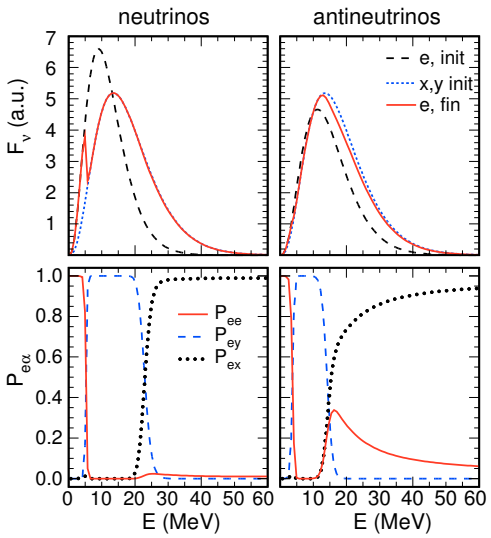

Figure 3.14: Cooling phase: the same of the Fig. 3.14. Figure taken from [76].

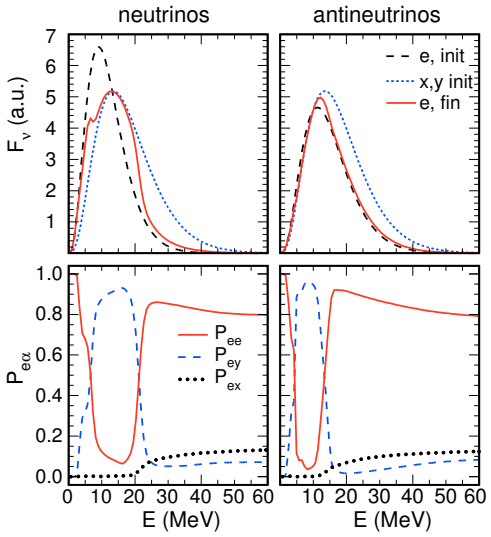

Figure 3.15: The same of the Fig. 3.14 but in the multi-angle case. Figure taken from [76].

Chapter 4

Matter suppression of self-induced neutrino oscillations during the SN accretion phase

The development of the self-induced ν conversions in supernovae crucially depends on the primary SN ν spectra. At this regard, the post-bounce accretion phase of core-collapse SNe would offer the best opportunity to detect signatures of collective ν flavor oscillations. Indeed, during this phase, the absolute ν fluxes are large with significant spectral differences between the different ν species and a flux order $F_{\nu_e} > F_{\overline{\nu}_e} \gg F_{\nu_x}$. As discussed in Chapter 3, self-induced spectral swaps and splits would occur in inverted mass hierarchy. However, it is important to realize that also the net electron density n_e should be large during the SN accretion phase. When it is not negligible in relation to the neutrino density n_ν, the large phase dispersion induced by the matter for ν's traveling on different directions is responsible for a partially or totally suppression of the collective oscillations through peculiar trajectory-dependent multi-angle effects [75].

In this context we have performed a numerical study of the matter suppression during the accretion phase, numerically solving the multi-angle equations of motion. We characterized the matter and the neutrino density profiles using the recent long-term neutrino radiation hydrodynamical simulations [81], based on three flavor Boltzmann neutrino transport in spherical symmetry. In contrast to what is expected in the presence of only neutrino-neutrino interactions, we found that the multi-angle effects associated with the dense ordinary matter strongly impact collective oscillations. Furthermore, we confirmed these results performing a linearized stability analysis of

the neutrino equations of motion, in the presence of the realistic SN density profiles. The results shown here are based on our works:

- S. Chakraborty, T. Fischer, A. Mirizzi, N. Saviano and R. Tomàs, "*No collective neutrino flavor conversions during the supernova accretion phase*," Phys. Rev. Lett. **107**, 151101 (2011).
- S. Chakraborty, T. Fischer, A. Mirizzi, N. Saviano and R. Tomàs, "*Analysis of matter suppression in collective neutrino oscillations during the supernova accretion phase*," Phys. Rev. D **84**, 025002 (2011).
- N. Saviano, S. Chakraborty, T. Fischer and A. Mirizzi, "*Stability analysis of collective neutrino oscillations in the supernova accretion phase with realistic energy and angle distributions*," Phys. Rev. D **85**, 113002 (2012).

4.1 Neutrino signal from SN model for the accretion phase

As already explained in the Sec. 3.1.1, neutrinos are emitted in different stages after the core-collapse of the star. In particular, the post-bounce accretion phase represents a very interesting scenario being characterised by large fluxes of neutrino and with significant spectral differences between the different neutrino species. At this regard, we characterize the neutrino emission during the accretion phase from core-collapse supernova simulations of massive progenitor stars of 8.8, 10.8 and 18 $M_\odot$, developed by the Basel-Darmstadt group [81]. The first mass, 8.8 $M_\odot$ belongs to the class of O-Ne-Mg-core progenitors [93, 94] and constitutes the threshold between thermonuclear explosions and core-collapse supernovae [95, 81]. Conversely, 10.8 and 18 $M_\odot$ are iron-core progenitors [96]. All models have been evolved through core collapse, bounce and the early post-bounce phase up to several seconds after the onset of explosion [81]. The core-collapse model is based on relativistic radiation hydrodynamics that considers three flavor Boltzmann neutrino transport in spherical symmetry and a complex equation of state for dense and hot nuclear matter [97] (for details about the supernova model, see [98, 81] and references therein). We note that the explosions of massive iron-core progenitors cannot occur in spherically symmetric supernova models and it has to be triggered by hand. Indeed for the 10.8 and 18 $M_\odot$ progenitor mass, the heating rates are artificially increased in the gain region where neutrinos deposit energy in order to revitalize the stalled bounce shock.

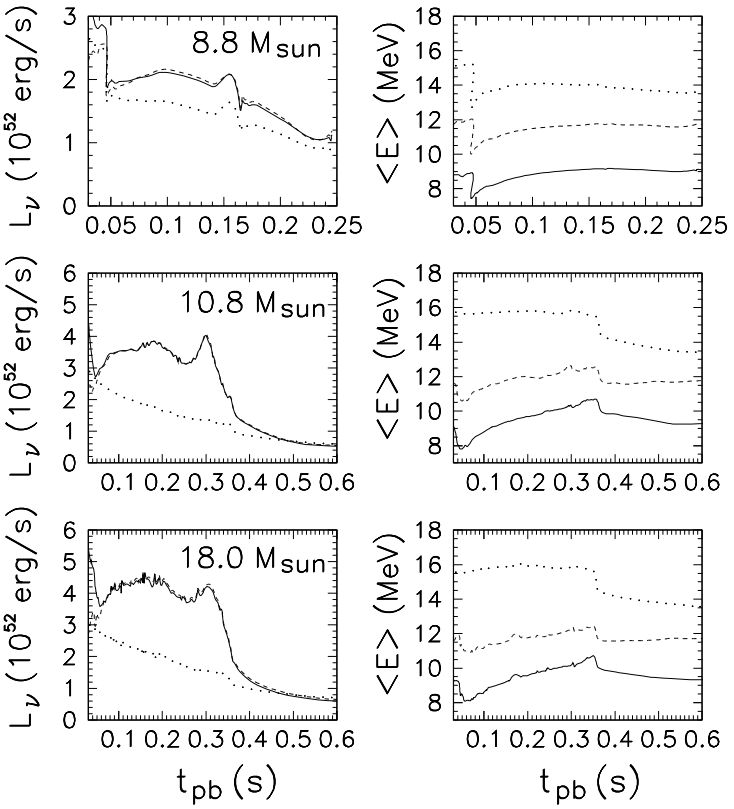

Figure 4.1: Neutrino luminosities (left panels) and average energies (right panels) during the accretion phase for 3 different progenitor mass core-collapse SN simulations: 8.8 $M_\odot$ (top), 10.8 $M_\odot$ (middle) and 18.0 $M_\odot$ (bottom). The continuous line represents ν_e, the dashed line the $\bar{\nu}_e$ and, finally, the dotted line the ν_x .

In Fig. 4.1 are shown the evolution of the neutrino luminosities L_{ν_α} (left panels) and average energies $\langle E_{\nu_\alpha} \rangle$ (right panels), during the post-bounce accretion phase for all models we consider. Here, $\nu_\alpha = (\nu_e, \overline{\nu}_e, \nu_x)$ where ν_x indicates both (μ, τ)-neutrinos and antineutrinos. As already discussed, the large electron flavor neutrino luminosities $\mathcal{O}(10^{52})$ erg/s are caused by the continuous mass accretion at the neutrinospheres and the ν_e luminosities are ruled by the charged current reactions. We remark that the slightly excess of the $\overline{\nu}_e$ luminosity with respect to the ν_e one and the magnitude of the differences obtained in the these different models are still under investigation and may slightly change improving weak rates and using multi-dimensional supernova models. The increasing and decreasing electron flavor luminosities mimic the propagating bounce shock (and the mass accretion rate at the neutrinospheres): it contracts during the accretion phase driven by neutrino

heating and expands driven by neutrino cooling. Moreover, $\nu_{\mu/\tau}$'s are produced only after bounce by pair-processes being the muonic charged current processes suppressed and then the (μ/τ)-neutrino luminosities are generally smaller than the electron flavor neutrino ones. Concerning the average energies during the accretion phase, for all models under investigation, we have the following hierarchy: $\langle E_{\nu_e} \rangle < \langle E_{\bar{\nu}_e} \rangle < \langle E_{\nu_x} \rangle$. As shown in In Fig. 4.1 (right panels), the average energies rise continuously for all neutrino flavors.

The situation changes after the onset of explosion, when mass accretion vanishes. Indeed, the luminosities and average energies of all flavors decrease on a longer timescale (on the order of seconds). For the O-Ne-Mg-core, we consider the neutrino signal only up to $t_{\rm pb}$=0.25 s (top panel of Fig. 4.1). We note that in this case the mass accretion at the neutrinospheres cancels out already at about $t_{\rm pb}$=0.03 s, determining the onset of the explosion. For the 10.8 and 18 $M_\odot$ progenitor models, we show the neutrino signal up to $t_{\rm pb}$=0.6 s. For these cases, the explosion starts at about $t_{\rm pb}$=0.36 s. This is caused by the more massive envelopes surrounding the iron-core responsible for a more extended accretion (and hence neutrino heating) phase. Furthermore, referring still to Fig. 4.1, we observe a sharp drop of the luminosities and average energies of all neutrino flavors after the onsets of explosion. This is due to the overturn of matter velocities from infall to expansion when the explosion shock passes through the distance of 500 km. Finally, we note that these results suggest lower average energies than usually assumed in the previous literature [99] and a less pronounced spectral hierarchy, in particular during the later proto-neutron star cooling phase. The results obtained for the low mass O-Ne-Mg-core collapse supernova explosion are in qualitative and quantitative good agreement with recent simulations performed by the Garching-group [100].

4.2 Characterization of the flavor conversions during the accretion phase

In this Section we present our assumptions in order to characterize the flavor conversions during the accretion phase. In particular, we first describe the geometry model for SN neutrino emission and neutrino number fluxes of different flavors, then we discuss the neutrino-neutrino and matter potentials and finally we introduce the different oscillation regimes.

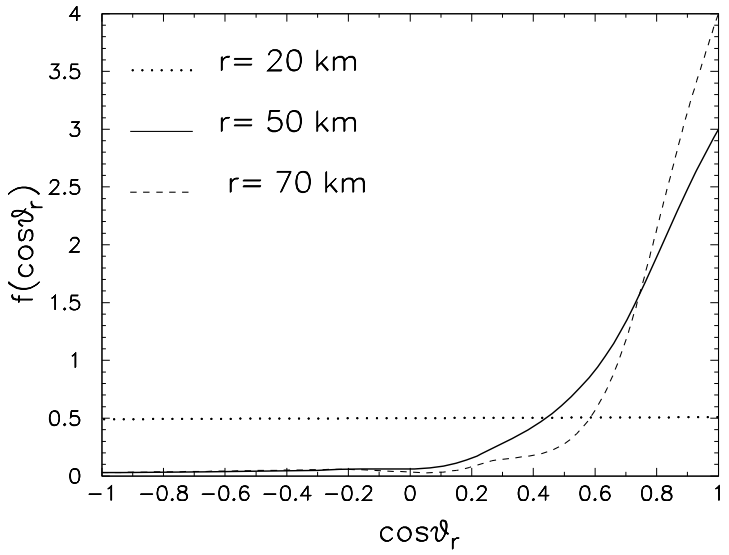

Figure 4.2: Angular distributions for ν_e of 10.8 $M_\odot$ progenitor mass, at $t_{\rm pb}$=0.4 s for $E_{\rm rms}$ = 11.5 MeV at different radii: r=20 km (dotted line), r=50 km (continuous line), r=70 km (dashed line).

4.2.1 Neutrino emission geometry

To take into account the geometry of the neutrino emission, we refer to the "bulb" model represented in the Fig. 3.11, in which neutrinos and antineutrinos are assumed emitted from spherically symmetrical source, the neutrinosphere, at radius $r = r_\nu$. We define r_ν as the radius where the neutrino radiation field is assumed to be "half-isotropic".We note that this conventional definition of the neutrinosphere is intended only to fix a boundary condition for the flavor evolution. Indeed, the half-isotropic definition does not necessarily coincide with the definition of the neutrinosphere as neutrino last scattering surface, defined as the radius where the optical depth becomes 2/3. However, the collective oscillations start at radii much larger than the adopted boundary that neutrinos can be safely assumed in a free-streaming regime [101]. Therefore, we do not carry about the details of the ν decoupling.

We fix r_ν consistently with the SN simulations which provide the angular distributions of the different neutrino species as a function of time and energy at different radii. We choose the ν_e's distribution as representative for all the different flavors since, during the accretion phase, they reach the free-streaming regime at larger radii with respect to the other neutrino species. Since the angular distributions are functions of the energy, we consider as reference the root mean square (rms) energy relevant for the average neutrino-nucleon interaction rates, which define the neutrino angular distributions. In

Fig. 4.2 we plot the ν_e angular distribution $f(\cos\theta_0) = dn_\nu/d\cos\theta_0$, where θ_r is the zenith angle of a given mode relative to the radial direction at distance r (see Fig. 3.11). Here $E_{\rm rms} = 11.5$ MeV at three different radii at the selected post-bounce time $t_{\rm pb} = 0.4$ s, as taken form the 10.8 $M_\odot$ model. At small radii ($r = 20$ km in the Fig. 4.2) the angular distribution is isotropic being the neutrinos in a trapping regime and then isotropically emitted in all directions. At large radii ($r = 70$ km in the Fig. 4.2), the angular distribution becomes forward peaked due to the free-streaming of neutrinos. We schematically *assume* the neutrinosphere radius as the one at which the ν_e's angular distribution has no longer significant backward flux, i.e. a few % of the total one (at $r = 50$ km in the Fig. 4.2).[1] Finally, we remark that the real angular distribution is not half-isotropic, rather more forward-peaked than what we are assuming, leading to a reduction of strength of the neutrino-neutrino potential. Therefore, our simplified choice has to be considered conservative.

4.2.2 Neutrino number fluxes for different flavors

The neutrino number flux for the different flavors is defined as $F_{\nu_\alpha} = L_{\nu_\alpha}/\langle E_{\nu_\alpha}\rangle$, while the flux asymmetries among the different ν species is described by the flavor asymmetry parameter ϵ in the Eq. (3.18)[73].

In Fig. 4.3 are shown the neutrino number flux F_{ν_α} (left panels) and the asymmetry parameter ϵ (right panels) for the three benchmark SN simulations considered. We observe that, as expected during the accretion phase, the particle fluxes present the following hierarchy $F_{\nu_e} > F_{\overline{\nu}_e} \gg F_{\nu_x}$, where the first part of the hierarchy is caused by the deleptonization of the collapsed stellar core, while the second is due to the absence of charged-current interactions for ν_x. Consequently, the electron and non-electron neutrino particle fluxes differ by almost a factor of two during the accretion phase. Conversely, during the cooling phase ($t_{\rm pb} > 0.05$ s), the flux differences tend to become much smaller.

Concerning the asymmetry parameter ϵ, the strong excess of ν_e's during the early post-bounce deleptonization ($t_{\rm pb} \lesssim 0.05$ s) leads to an increase, such that $\epsilon \gg 1$. Then, ϵ drops and reaches values between 0.3-0.5 during the accretion phase (see Fig. 4.3). Finally, since the flux difference $F_{\overline{\nu}_e} - F_{\overline{\nu}_x}$ drops more rapidly than $F_{\nu_e} - F_{\nu_x}$, ϵ rises again, becoming larger than 1 for the iron-core SNe. This behavior will impact the development of the self-induced flavor conversions.

[1] Changing the neutrinosphere radius by a factor of three, we checked that the results on matter effects remained basically unchanged, indicating a weak dependence of the oscillation analysis from the decoupling region.

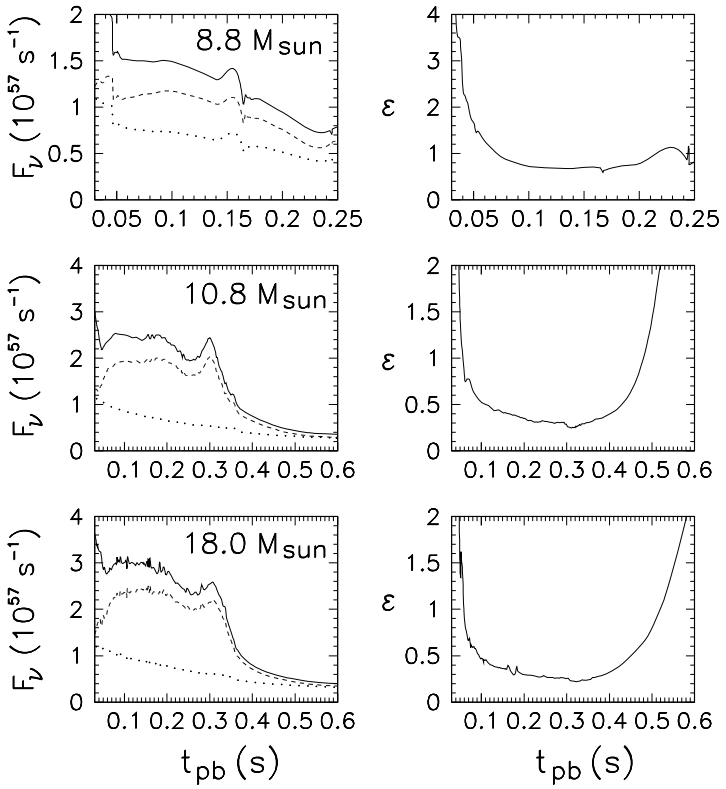

Figure 4.3: Neutrino particle fluxes (left panels) and flavor asymmetry parameter ϵ (right panels) for ν_e (continuous line), $\overline{\nu}_e$ (dashed line), ν_x (dotted line).

4.2.3 Set-up of the flavor evolution

We study the non-linear neutrino flavor conversions in the two-flavor oscillation scenario, driven by the atmospheric mass-square difference $\Delta m^2_{\rm atm} \simeq 2.6 \times 0^{-3}$ eV^2 and by a small (matter suppressed) in-medium mixing $\theta_{\rm eff} = 10^{-3}$ and considering the inverted mass hierarchy case. Indeed, the three-flavor effects, associated with the solar sector, are small for the neutrino flux ordering expected during the accretion phase [103, 76]. Moreover in the normal mass hierarchy and for the spectral ordering of the accretion phase, no self-induced flavor conversion will occur.

We take into account the effect of the non-isotropic nature of neutrino emission on collective oscillations by "multi-angle" simulations [77], where one follows a large number [$\mathcal{O}(10^3)$] of neutrino trajectories [Eq. (3.24)–(3.25)]. Even if the neutrinos are emitted with a broad energy distribution, we will assume all ν's to be represented by a single energy, $E = 15$ MeV, in order to simplify the numerical calculation. This assumption is justified

by the fact that large matter effects would lock togheter the different neutrino energy modes, both in case of supression [75] and of decoherence [73] of collective oscillations.

This choice results in the neutrino vacuum oscillation frequency

$$\omega = \left\langle \frac{\Delta m^2_{\rm atm}}{2E} \right\rangle = 0.4 \ \ {\rm km}^{-1} \ . \tag{4.1}$$

The strength of the neutrino-neutrino interaction, normalized at the neutrinosphere, is parametrized by [73]

$$\begin{aligned} \mu_r &= \sqrt{2} G_F \left[n_{\overline{\nu}_e}(r) - n_{\overline{\nu}_x}(r) \right] \\ &= 7 \times 10^5 \ \ {\rm km}^{-1} \left(\frac{L_{\overline{\nu}_e}}{\langle E_{\overline{\nu}_e} \rangle} - \frac{L_{\overline{\nu}_x}}{\langle E_{\overline{\nu}_x} \rangle} \right) \\ &\times \ \ \frac{15 \ \ {\rm MeV}}{10^{52} {\rm erg}} \left(\frac{10 \ \ {\rm km}}{r} \right)^2 \end{aligned} \tag{4.2}$$

where $n_{\nu_\alpha}(r)$ is the flux of the neutrino species ν_α at radius r defined as $n_{\nu_e,\bar{\nu}_e} = F_{\nu_e,\bar{\nu}_e}/(4\pi r^2)$.

The matter potential is represented by [69]

$$\begin{aligned} \lambda_r &= \sqrt{2} G_F n_e(r) = 1.9 \times 10^6 \ \ {\rm km}^{-1} \\ &\times \ \ \left(\frac{Y_e}{0.5} \right) \left(\frac{\rho}{10^{10} \ \ {\rm g/cm}^3} \right) \end{aligned} \tag{4.3}$$

encoding the net $n_e \equiv n_{e^-} - n_{e^+}$ electron density, whit $Y_e = Y_{e^-} - Y_{e^+}$ the net electron fraction and ρ the matter density. We note that λ_r is given by the detailed matter profile from the SN simulations.

4.2.4 Oscillation regimes

In the case of absence of matter suppression, collective neutrino flavor conversions start outside the synchronization radius, given by [73]

$$\frac{r_{\rm sync}}{r_\nu} = \left(\frac{\sqrt{1+\epsilon} - 1}{2} \right)^{1/2} \left(\frac{\mu_r \big|_{r=r_\nu}}{\omega} \right)^{1/4} \ , \tag{4.4}$$

and they develop at least up to the radii $r_{\rm end}$ in which the neutrino-neutrino interaction strength becomes comparable to the vacuum term, i.e. at [74]

$$\frac{r_{\rm end}}{r_\nu} = \left(\frac{\mu_r \big|_{r=r_\nu}}{2\omega} \right)^{1/4} \ . \tag{4.5}$$

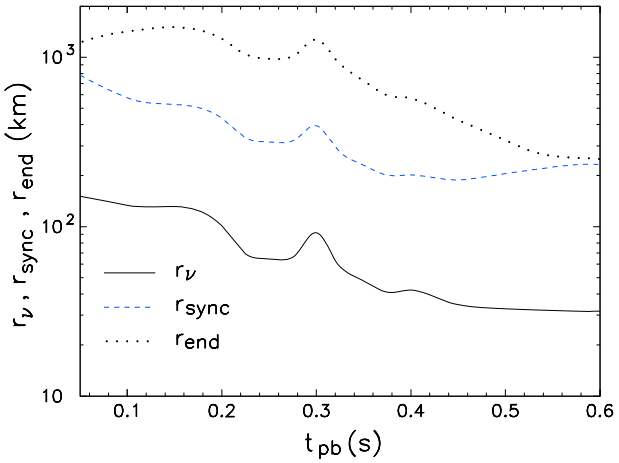

Figure 4.4: Time evolution of r_ν (continuous line), $r_{\rm sync}$ (dashed curve) and $r_{\rm end}$ (dotted curve), for 10.8 $M_\odot$ progenitor mass.

We remind the reader that outside $r_{\rm sync}$ the multi-angle nature of the neutrino trajectories can lead to self-induced flavor decoherence between different angular modes. However, if the asymmetry parameter ϵ is significantly large, multi-angle effects are suppressed and self-induced neutrino conversions present the collective behavior [73].

According to these definitions, in Fig. 4.4 we present for the case of the 10.8 $M_\odot$ SN simulation, the neutrinosphere radius R_ν, the synchronization radius $r_{\rm sync}$ and the radius $r_{\rm end}$ at which collective effects saturate. We observe that $R_\nu \sim 10^2$ km during the accretion phase and drops to ~ 30 km at the beginning of the cooling phase.

Collective oscillations should occur in the range $r \in [r_{\rm sync}, r_{\rm end}]$. This range is at $r \sim [600, 1500]$ km at $t_{\rm pb} = 0.1$ s when the neutrinosphere radius $R_\nu > 10^2$ km, driving the flavor conversions to larger radii. Then, due the contraction of the neutrinosphere radius, the conversion range shifts at smaller radii $r \sim [200, 500]$ km at $t_{\rm pb} \simeq 0.4$ s. Finally at $t_{\rm pb} \simeq 0.6$ s, the lower neutrino luminosity and the larger asymmetry parameter ϵ operate together to push $r_{\rm sync}$ towards $r_{\rm end}$ [see Eqs. (4.4)–(4.5)].

It is important to note, that in the range $[r_{\rm sync}, r_{\rm end}]$, the self-induced neutrino oscillations can be affected by the dense matter when [75]

$$n_e \gtrsim n_{\overline{\nu}_e} - n_{\overline{\nu}_x} \ . \tag{4.6}$$

In particular, as discussed in Sec. 3.3.3, when the electron and neutrino densities are comparable, matter effects induce multi-angle decoherence among different neutrino modes, leading to a flavor equilibration among the different species. When the net electron density is significantly larger than the

neutrino one, collective oscillations are suppressed at all [75].

We remark that previous numerical studies of collective oscillations typically considered smaller neutrinosphere radii, namely $r_\nu = \mathcal{O}(10 \text{ km})$ (see, e.g., [73]). Nevertheless, this choice is more indicate for the cooling phase rather than for the accretion one. As a consequence, in the our work the neutrino oscillations start at larger radii than typically assumed in previous studies.

4.3 Results of matter effect for different progenitor mass

In this Section we present the results of our study regarding the effects of dense matter on of the self-induced neutrino oscillations for the three representative SN simulations based on the different progenitor masses.

4.3.1 10.8 $M_\odot$ progenitor mass

We start our study with the case of the 10.8 $M_\odot$ iron-core SN. In Fig. 4.5 are shown, for different post-bounce times, the net electron density n_e (left panel) as well as the difference of neutrino densities $n_{\overline{\nu}_e} - n_{\overline{\nu}_x}$ (right panel) which defines the potential μ_r [Eq. (4.2)]. While the neutrino density simply scales as r^{-2}, the electron density presents a more complicated behavior as we can infer observing the abrupt discontinuity in n_e associated with the supernova shock-front that propagates in time. The shock-wave starts to dissipate its energy due to heavy nuclei dissociation and eventually stalls at $t_{\rm pb} = 0.05$ s. The standing accretion shock is then revitalized via neutrino heating, on a timescale on the order of 0.1 seconds, and expands accordingly as well as contracts via neutrino cooling. After 0.35 seconds post-bounce, the standing accretion shock turns into a dynamic shock with positive matter velocities, giving rise to the onset of explosion at about 0.4 seconds post-bounce.

During the accretion phase of the 10.8 $M_\odot$ iron-core SN model, the matter density in the post-shock region decreases slower than the neutrino density, in particular as $\sim r^{-1.5}$. From the comparison between the electron and the neutrino densities, we notice that at the different post-bounce times, n_e is always larger than or comparable to $n_{\overline{\nu}_e} - n_{\overline{\nu}_x}$ suggesting that is not possible to neglect matter effects on self-induced flavor conversions.

We quantify the relative strength of the electron and neutrino densities

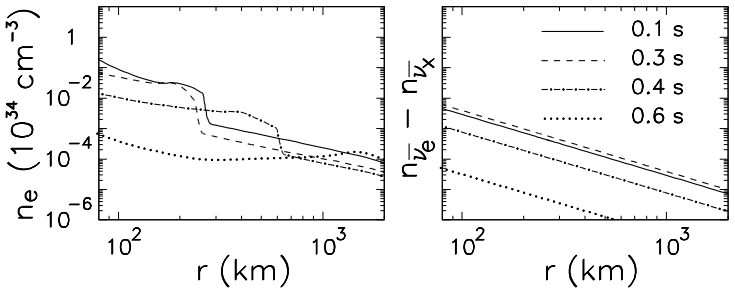

Figure 4.5: Radial evolution of the net electron density n_e (left panel) and of the neutrino density difference $n_{\overline{\nu}_e} - n_{\overline{\nu}_x}$ (right panel) at different post-bounce times, for 10.8 $M_\odot$ progenitor mass.

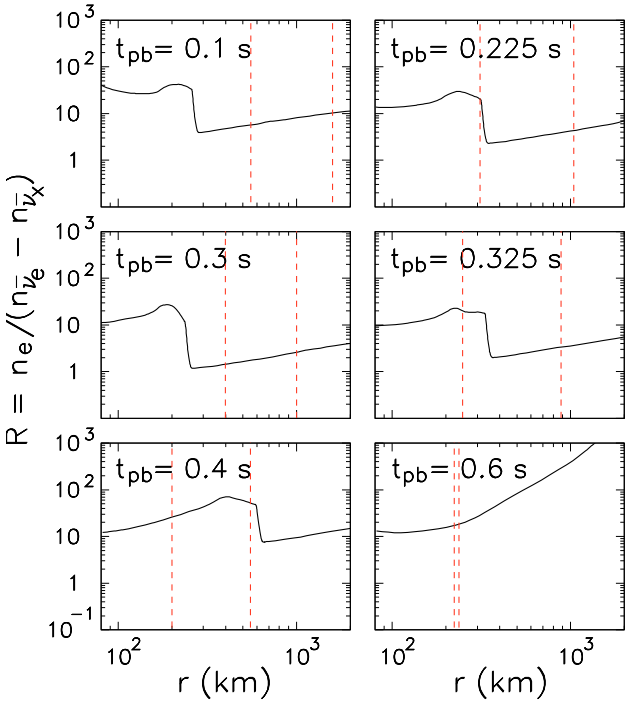

Figure 4.6: Radial evolution of the ratio R between electron and neutrino densities at different post-bounce times, 10.8 $M_\odot$ progenitor mass. The two dashed vertical lines define the position of $r_{\rm sync}$ (left lines) and $r_{\rm end}$ (right lines).

considering the ratio

$$R = \frac{n_e}{n_{\overline{\nu}_e} - n_{\overline{\nu}_x}} \quad . \tag{4.7}$$

as a function of the radial coordinate r at different post-bounce times for $t_{\rm pb} \in$

$[0.1, 0.6]$ s, shown in in Fig. 4.6. The range $r_{\rm sync} < r < r_{\rm end}$, delimited in the same figure with two vertical dashed lines, set the possible range for the self-induced flavor conversions and the shock radius $r_{\rm sh}$ presents the abrupt drop in the electron density. Therefore, their relative position is very important to estimate the impact of matter effects on the self-induced oscillations. In this range, $R \gg 1$ will imply a strong matter dominance in the flavor conversions and thus complete suppression of the collective effects, while, when electron and neutrino densities are comparable ($R \gtrsim 1$), decoherence will occur for the collective oscillations.

Let us discuss in more detail the Fig. 4.6. At very early post-bounce times ($t_{\rm pb} = 0.1$ s) the matter term strongly predominates the neutrino term also behind the shock-front ($R \gg 1$) blocking the oscillations. At intermediate times ($t_{\rm pb} = 0.225, 0.3$ s), in the shock-post region (where the flavor conversion are expected), the matter density drops faster than the neutrino one, leading the $R = 1 - 2$. In this case matter-induced decoherence is possible. Next, at $t_{\rm pb} = 0.325$ s, oscillations are suppressed behind the shock front, but then decoherence will develop at larger radii ($r \gtrsim 300$ km) when $R \gtrsim 1$. Finally, at later times ($t_{\rm pb} = 0.4, 0.6$ s), the shock has restarted its forward motion and the region relevant for the oscillations is at $r < r_{\rm sh}$, where $R \gg 1$, leading to the suppression of self-induced oscillations.

These expectations are confirmed by the results of our multi-angle numerical study of the equations Eq. (3.24)–(3.25) for neutrino evolution. In Fig. 4.7 are shown the radial evolution of the $\overline{\nu}_e$ survival probability P_{ee} (continuous black curve) for different post-bounce times, obtained taking into account the effects of the SN matter profile. For comparison, are also shown the results obtained setting $n_e = 0$ (dashed red curve). At this regard, we comment that, in absence of ordinary matter, for the given flavor asymmetry $\epsilon \gtrsim 0.3$, we would have expected the "quasi-single angle" behavior described in Ref. [73], where after the onset of the conversions at $r = r_{\rm sync}$, the survival probability P_{ee} decrises smoothly approaching zero at large radii. However, in our study the flavor conversions develop at radii larger than what is typically shown in previous works (see, e.g., [73]). Therefore, the evolution is more adiabatic (i.e. the evolution length scale $l_\mu \sim r$ [102]) and, consequently, effects of self-induced multi-angle decoherence could develop, producing some small disturbance in the smooth decline of the survival probability at large radii (visible at $t_{\rm pb} = 0.1, 0.3, 0.325$ s for $r \gtrsim 700$ km). Even if this finding is potentially interesting, we did not investigate more due to the fact that matter effects will alter this picture.

In reference to the Fig. 4.7 , we observe that, in presence of matter, at $t_{\rm pb} = 0.1, 0.4, 0.6$ s the flavor oscillations are completely blocked, since $R \gg 1$ in the conversion range. For the other three intermediate times ($t_{\rm pb} =$

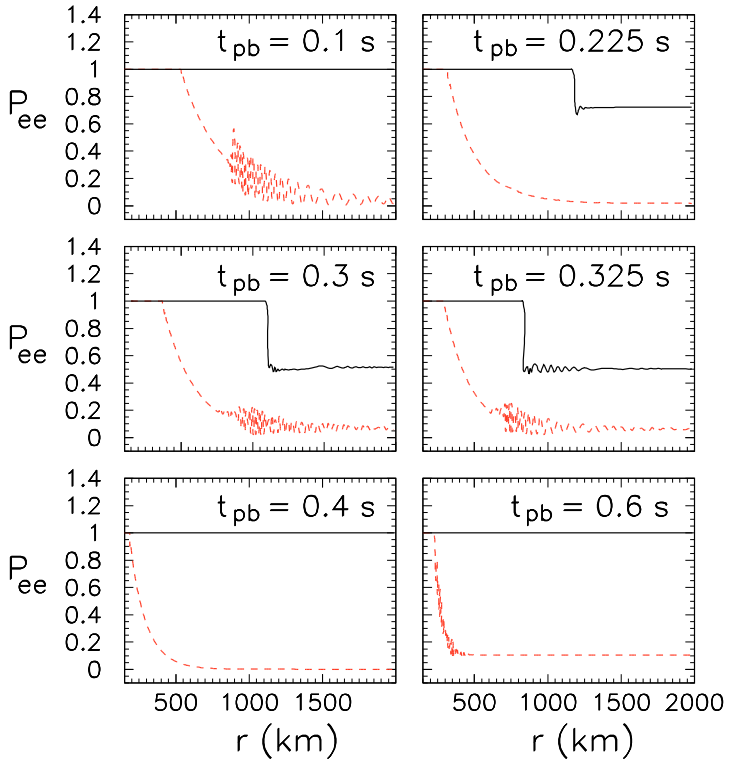

Figure 4.7: Radial evolution of the survival probability P_{ee} for $\overline{\nu}_e$ at different post-bounce times, in presence of matter effects (continuous curve) and for $n_e = 0$ (dashed curve), considering a multi-angle evolution for the 10.8 $M_\odot$ progenitor mass.

$0.225, 0.3, 0.325$ s), the presence of a large matter term at $r_{\rm sync}$ significantly delays the onset of the flavor conversions with respect to the case with $n_e = 0$. Then, at larger radii ($r > 700$ km) when $R \gtrsim$1–2, matter effects partial suppress the flavor conversions. When the flavor decoherence is complete, it leads to $P_{ee} \to 1/2$ (at $t_{\rm pb} = 0.3, 0.325$ s), implying a complete mixture between $\overline{\nu}_e$ and $\overline{\nu}_x$.

4.3.2 18.0 $M_\odot$ progenitor mass

In addition to the 10.8 $M_\odot$ progenitor mass, we also consider the SN simulation of the more massive 18 $M_\odot$ iron-core progenitor, for which the net electron density n_e (left panel) and the difference of neutrino densities $n_{\overline{\nu}_e} - n_{\overline{\nu}_x}$, at different post-bounce times, are shown in the Fig. 4.8. Comparing with Fig. 4.5, we see that their evolution in time is similar to the case 10.8 $M_\odot$ SN simulation. Therefore, we expect a similar impact for the matter effects

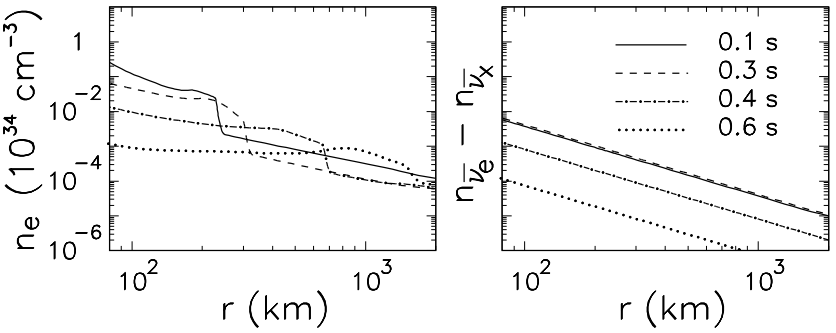

Figure 4.8: The same description of the Fig. 4.5 for 18 $M_\odot$.

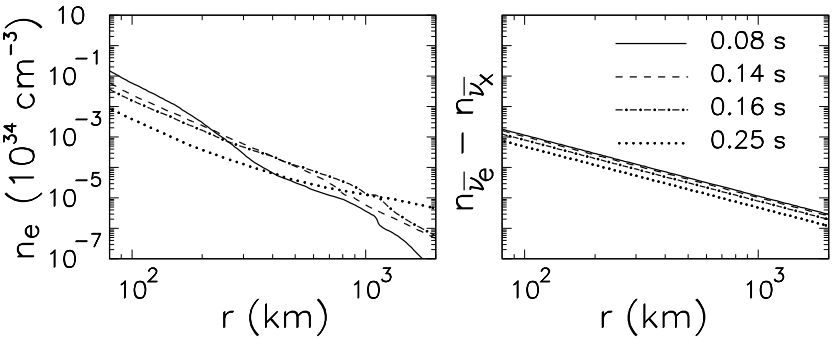

Figure 4.9: Radial evolution of the net electron density n_e (left panel) and of the neutrino density difference $n_{\overline{\nu}_e} - n_{\overline{\nu}_x}$ (right panel) at different post-bounce times, for 8.8 $M_\odot$ progenitor mass.

on the neutrino flavor evolution. Indeed we observe an analogous pattern of complete $0.05 \lesssim t_{\rm pb} \lesssim 0.2$ s), partial ($0.2 \lesssim t_{\rm pb} \lesssim 0.35$ s) and complete ($0.35 \lesssim t_{\rm pb} \lesssim 0.6$ s) matter suppression in the self-induced flavor conversions, that we do not show here for sake of brevity.

4.3.3 8.8 $M_\odot$ progenitor mass

As last case, we study the SN neutrino flavor evolution for the low mass 8.8 $M_\odot$ O-Ne-Mg core SN model. In Fig. 4.9 are presented the net electron density n_e (left panel) and the difference of neutrino densities $n_{\overline{\nu}_e} - n_{\overline{\nu}_x}$ (right panel) for different post-bounce times. We find a notably difference in these density profiles with respect to the iron-core SN cases. In particular we observe that the electron density profile above the core is very steep, declining as $\sim r^{-2.5}$, faster than the neutrino density. This is due to the fact the matter density of the envelope is very low compared to the iron-core progenitors. Moreover, also the neutrino densities for $t_{\rm pb} \lesssim 0.2$ s are roughly a factor

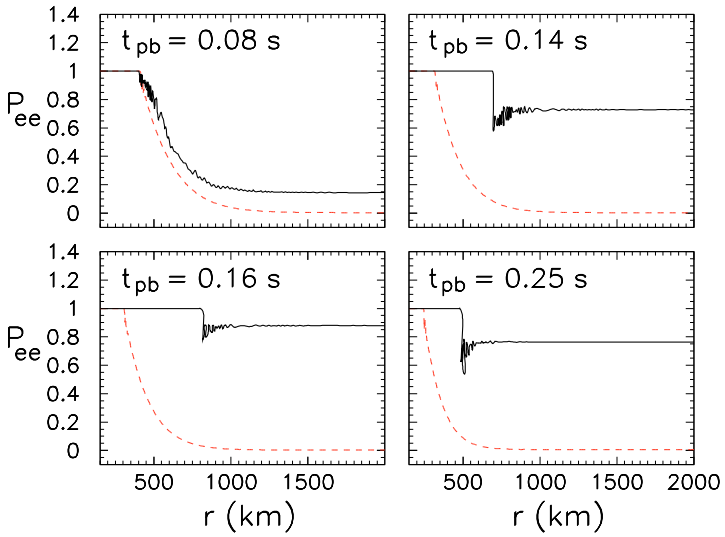

Figure 4.10: Radial evolution of the survival probability P_{ee} for $\overline{\nu}_e$ at different post-bounce times, in presence of matter effects (continuous curve) and for $n_e = 0$ (dashed curve), considering a multi-angle evolution for the 8.8 $M_\odot$ progenitor mass.

~ 3 smaller than in the previous cases, reflecting the practical absence of an extended accretion phase for this low-mass star. Since the explosion succeeds very shortly after the core-bounce, the shock-front is already beyond the radial range which is interesting for the flavor conversions.

The time-evolution of the $\overline{\nu}_e$ survival probability P_{ee} at different post-bounce times presents a change between a regime dominated by the ν–ν effect at very early times and one of matter-suppressed oscillations at later times, as shown in Fig. 4.10. We find that at $t_{\rm pb} = 0.08$ s, the matter suppression is relatively small and the neutrino-neutrino interactions produce a quite almost complete swap between $\overline{\nu}_e$ and $\overline{\nu}_x$ spectra ($P_{ee} = 0.15$ at the end of the evolution). Conversely, for the later times, the flavor conversions are strongly suppressed with a final $P_{ee} \simeq 0.7 - 0.9$.

4.4 Stability analysis of the self-induced flavor conversions

Our results of the matter suppression on the collective flavor conversions presented in the previous section have stimulated further independent studies. In particular, in [105] it has been proposed to investigate the matter effects with a linearized stability analysis of the neutrino equations of mo-

tion [106] in order to obviate the numerical challenges of full "multi-angle" simulations for the flavor evolution. Indeed if one is interested only in the issue of the flavor stability of the dense neutrino gas, i.e. if the flavor conversions occur or not, the stability analysis allows to determine the possible onset of the conversions. In particular, one seeks for an exponentially growing solution of the eigenvalue problem, associated with the linearized equations of motion for the neutrino ensemble. Driven by this insight, we have decided to apply the stability analysis to the same models discussed before, taking into account also realistic energy and angle neutrino distributions, finding a complete agreement with our previous numerical result.

4.4.1 The stability condition equations

We present the main ingredients to perform the stability analysis of the neutrino equations of motion following the treatment of [106]. The flavor scenario adopted in this study is the same of that presented in the Sec. 4.2. Following [106], we find useful to express the equations of motion [Eqs. (3.24)–(3.25)] in terms of the flux matrices $\Phi_{E,u} = (r^2E^2/2\pi)\rho_{E,u}$ as function of the radial coordinate. The diagonal $\Phi_{E,u}$ components are the ordinary number fluxes $F_{\nu_\alpha}(E,u)$ integrated over a sphere of radius r, while the off-diagonal elements, which are initially zero, denote a phase information due to flavor mixing. We normalize the flux matrices to the total $\overline{\nu}_e$ number flux $n_{\overline{\nu}_e}$ at the neutrino-sphere and we define negative E and negative number fluxes for anti-neutrinos Then the equations of motion read:

$$\mathrm{i}\partial_r \Phi_{E,u} = [H_{E,u}, \Phi_{E,u}] \tag{4.8}$$

with the Hamiltonian

$$\begin{aligned} H_{E,u} &= \frac{1}{v_u}\left(\frac{M^2}{2E} + \sqrt{2}G_F N_l\right) \\ &+ \frac{\sqrt{2}G_F}{4\pi r^2}\int_{-\infty}^{+\infty} dE' \int_0^1 du' \left(\frac{1 - v_u v_{u'}}{v_u v_{u'}}\right) \Phi_{E',u'} \ . \end{aligned} \tag{4.9}$$

To follow the stability prescription, we first switch to the frequency variable $\omega = \Delta m^2_{\mathrm{atm}}/2E$ so that $E(\omega) = |\Delta m^2_{\mathrm{atm}}/2\omega|$ and we introduce the neutrino flux difference distributions $g_{\omega,u} \equiv g(\omega,u)$ defined as

$$\begin{aligned} g_{\omega,u} = \frac{|\Delta m^2_{\mathrm{atm}}|}{2\omega^2} \times \Big\{ &\Theta(\omega)\left[F_{\nu_e}(E(\omega),u) - F_{\nu_x}(E(\omega),u)\right] \\ &+\Theta(-\omega)\left[F_{\nu_x}(E(\omega),u) - F_{\overline{\nu}_e}(E(\omega),u)\right] \Big\} \end{aligned} \tag{4.10}$$

normalized to the total $\overline{\nu}_e$ flux at the neutrino-sphere. At this point, we write the flux matrices in the form

$$\Phi_{\omega,u} = \frac{\mathrm{Tr}\Phi_{\omega,u}}{2} + \frac{g_{\omega,u}}{2} \begin{pmatrix} s_{\omega,u} & S_{\omega,u} \\ S^*_{\omega,u} & -s_{\omega,u} \end{pmatrix} \ . \tag{4.11}$$

The term $\mathrm{Tr}\Phi_{\omega,u}$ is conserved and then irrelevant for the flavor conversions. The initial conditions for the "swapping matrix" in the second term on the right-hand side are $s_{\omega,u} = 1$ and $S_{\omega,u} = 0$. Self-induced flavor conversions start when the off-diagonal term $S_{\omega,u}$ grows exponentially.

In the small-amplitude limit $|S_{\omega,u}| \ll 1$, and considering a large distances from the neutrino-sphere $r \gg r_\nu$, the linearized evolution equations for $S_{\omega,u}$ in inverted mass hierarchy ($\Delta m^2_{\mathrm{atm}} < 0$) assume the form [106]

$$\begin{aligned} \mathrm{i}\partial_r S_{\omega,u} &= [\omega + u(\lambda^*_r + \epsilon\mu^*_r)]S_{\omega,u} \\ &- \mu \int du' d\omega' (u + u') g_{\omega',u'} S_{\omega',u'} \ , \end{aligned} \tag{4.12}$$

where

$$\epsilon = \int du \ d\omega \ g_{\omega,u} \ , \tag{4.13}$$

quantifies the asymmetry parameter of the neutrino spectrum, normalized to the total $\overline{\nu}_e$ number flux. The ν-ν interaction strength is given by

$$\begin{aligned} \mu^*_r &= \mu_r \frac{r^2_\nu}{2r^2} \\ &= \frac{3.5 \times 10^9}{r^4} \left(\frac{L_{\overline{\nu}_e}}{10^{52} \ \mathrm{erg/s}} \right) \left(\frac{15 \ \mathrm{MeV}}{\langle E_{\overline{\nu}_e} \rangle} \right) \left(\frac{r_\nu}{10 \ \mathrm{km}} \right)^2 , \end{aligned}$$

while ordinary matter background term is given by

$$\begin{aligned} \lambda^*_r &= \lambda_r \frac{r^2_\nu}{2r^2} \\ &= \frac{0.95 \times 10^8}{r^2} \left(\frac{Y_e}{0.5} \right) \left(\frac{\rho}{10^{10} \mathrm{g/cm^3}} \right) \left(\frac{r_\nu}{10 \ \mathrm{km}} \right)^2 , \end{aligned}$$

Writing the solution of the linear differential equation [Eq. (4.12)] in the form $S_{\omega,u} = Q_{\omega,u} e^{-i\Omega r}$ with complex frequency $\Omega = \gamma + i\kappa$ and eigenvector $Q_{\omega,u}$, a value of $\kappa > 0$ would indicate an exponential increasing $S_{\omega,u}$, i.e. an instability. Moreover we reformulte the solution of Eq. (4.12) in the form of an eigenvalue equation for $Q_{\omega,u}$. Splitting this equation into its real and

imaginary parts we arrive, for a multi-angle case, at two real equations that have to be satisfied [106]

$$\begin{aligned}(J_1 - \mu_r^{*-1})^2 &= K_1^2 + J_0 J_2 - K_0 K_2 \ , \\ (J_1 - \mu_r^{*-1}) &= \frac{J_0 K_2 + K_0 J_2}{2K_1} \ , \end{aligned} \tag{4.14}$$

where

$$\begin{aligned} J_n &= \int d\omega du \ g_{\omega,u} u^n \frac{\omega + u(\lambda_r^* + \epsilon\mu_r^*) - \gamma}{[\omega + u(\lambda_r^* + \epsilon\mu_r^*) - \gamma]^2 + \kappa^2} \ , \\ K_n &= \int d\omega du \ g_{\omega,u} u^n \frac{\kappa}{[\omega + u(\lambda_r^* + \epsilon\mu_r^*) - \gamma]^2 + \kappa^2}. \end{aligned} \tag{4.15}$$

A flavor instability is present whenever Eqs. (4.14) admit a solution (γ, κ).

4.4.2 Stability analysis for the accretion phase

In this section we present our results of the stability analysis applied to the SN models with 10.8 $M_\odot$ and 8.8 $M_\odot$ progenitor masses considering realistic energy and angular neutrino distributions. [2]

Energy and angular neutrino distributions Realistic supernova simulations show that ν angular distributions at the decoupling are not half-isotropic and, moreover, they are flavor-dependent (see, e.g., [105, 107]).

Therefore we take into account the angle and energy distributions $F_{\nu_\alpha}(E, u)$ of the different neutrino species, extracted from SN simulations of [81]. We label the ν angular spectra in terms of the variable $u = \sin^2\theta_0$, where θ_0 is the emission angle with respect to the neutrino-sphere (see Sec. 3.3.3).

In Fig. 4.11 we present the (angle-integrated) flux energy spectra $F_{\nu_\alpha}(E)$ (upper panels) and the (energy-integrated) flux angular spectra $F_{\nu_\alpha}(u)$ (lower panels) for ν_e, $\overline{\nu}_e$, ν_x, with x the non-electron flavors. In particular, the fluxes for the 10.8 $M_\odot$ SN progenitor are shown at $t_{\rm pb} = 225$ ms (left panels), while that for the 8.8 $M_\odot$ SN progenitor at $t_{\rm pb} = 250$ ms (right panels). The angular variable $0 \leq u \leq 1$ characterizes the geometry of the problem (see Sec. 3.3.3), with $R_\nu = 69$ km for the 10.8 $M_\odot$ model and $R_\nu = 47$ km for the 8.8 $M_\odot$ model. The energy and angular distributions are normalized to the total neutrino number fluxes of the different species (in arbitrary units in the Fig. 4.11). Concerning the neutrino energy distributions for the different flavors, the angle-integrated energy spectra are represented by the Eq. (3.1).

[2] We omitted to show the results for the 18 $M_\odot$ SN progenitor, since it is qualitatively similar to the 10.8 $M_\odot$ case.

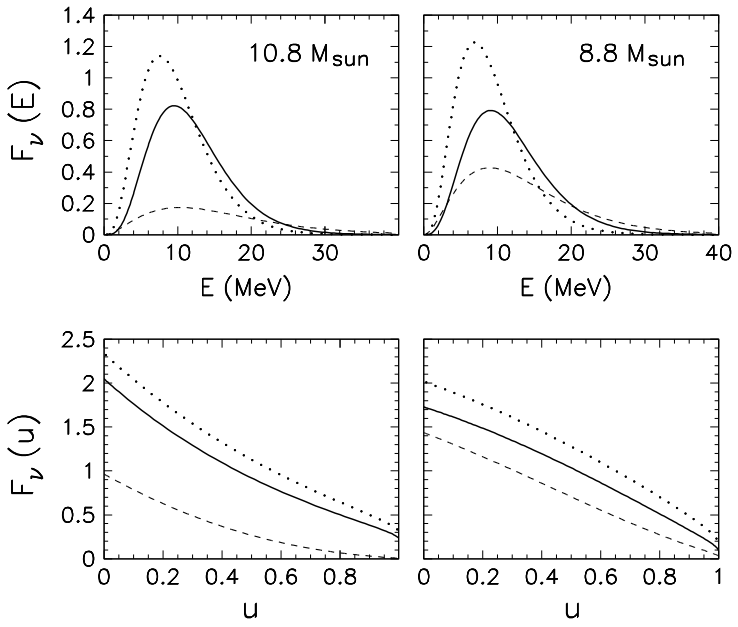

Figure 4.11: Supernova neutrino flux spectra (in arbitrary units) for 10.8 $M_\odot$ progenitor at $t_{\rm pb} = 0.225$ s (left panels) and for 8.8 $M_\odot$ progenitor at $t_{\rm pb} = 0.250$ s (right panels). The energy (upper panels) and the angular (lower panels) spectra are shown for ν_e (dotted curves), $\overline{\nu}_e$ (continuous curves) and ν_x (dashed curves) (see the text for details).

From the angular flux spectra in the Fig. 4.11, we realize that in the case of the 10.8 $M_\odot$ model, these are significantly forward enhanced (i.e. peaked at small u), with respect to the half-isotropic emission model. In addition, the angular distributions of the three ν species at the neutrinosphere are different. Indeed the ν_x distributions are more suppressed in the direction tangential to the neutrino-sphere (i.e. at $u \sim 1$), since the ν_x decouple at smaller radii with respect to ν_e and $\overline{\nu}_e$. Conversely, the case of 8.8 $M_\odot$ presents angular spectra for the electron species less forward-enhanced than in the previous case, and with less pronounced differences with the non-electron species. As for the energy spectra, this behavior is dominated by the neutral-current processes in the spectra formation.

10.8 $M_\odot$ iron-core In Fig. 4.12 we show the radial evolution of the eigenvalue κ function obtained from the solution of Eqs. (4.14) and we discuss them in comparison with the survival probability of electron antineutrinos P_{ee} presented inSec. 4.3 (see Fig. 4.7), for the same post-bounce times. We

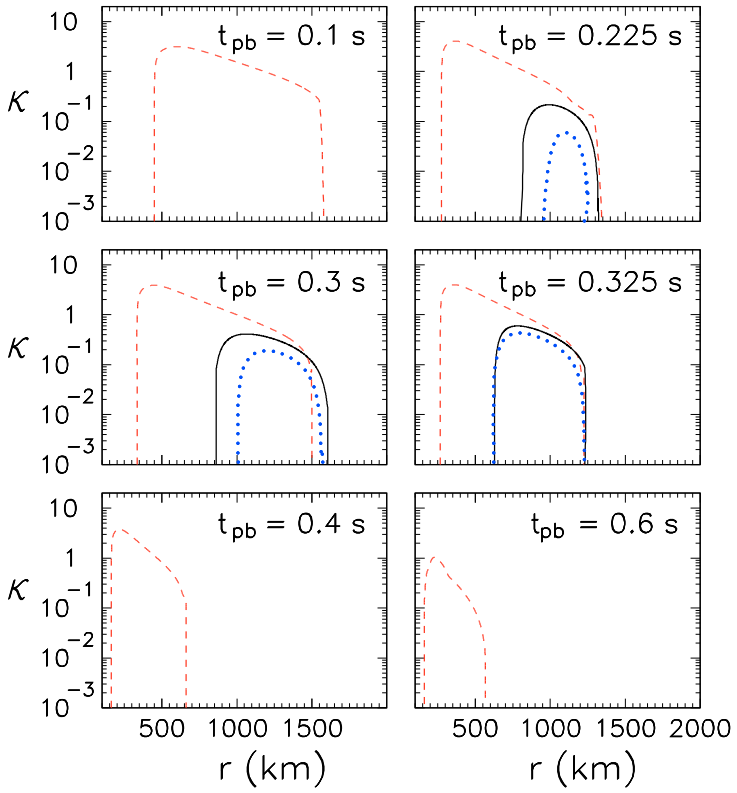

Figure 4.12: 10.8 $M_\odot$ progenitor mass. Radial evolution of the κ function at different post-bounce times for different cases: *(a)* $n_e = 0$ for a half-isotropic neutrino emission (red dashed curves), *(b)* in presence of matter effects, with a half-isotropic neutrino emission (black continuous curves), *(c)* in presence of matter effects with flavor-dependent angular distributions (blue dotted curves). Quasi-thermal ν energy spectra are assumed (see the text for details).

consider the following cases: *(a)* $n_e = 0$ and a half-isotropic neutrino emission (dashed curves), *(b)* dense matter effects and a half-isotropic neutrino emission (continuous curves) and, *(c)* dense matter effects and non-trivial neutrino angular distributions (dotted curves). In all these cases we have always assumed quasi-thermal neutrino energy distributions, parametrized as in Eq. (3.1).

Starting with the case *(a)*, we observe that when the neutrino system enters an unstable regime ($\kappa > 0$), the κ function rapidly grows from zero to a peak value greater than one. Comparing this result with the numerical solution presented in Fig. 4.7, we see a perfect agreement between the start of the self-induced flavor conversions and the position of the peak in the κ function

found here. We note, that the multi-energy effects included in the stability does not affect the onset of the flavor conversions with respect to what observed in our previous mono-energetic investigation. Conversely multi-energy effects would play a crucial role in determining the splitting features in the final neutrino spectra, once the conversions are triggered. Passing to the case *(b)*, as expected, the flavor instability is strongly suppressed in relation to the previous case with $n_e = 0$. In particular, the κ function is non-zero only at intermediate post-bounce times, i.e. $t_{\rm pb} = 0.225, 0.3, 0.325$ s in Fig 4.12 and rise of the κ function is shifted at larger radii (by $\sim 400-500$ km) with respect to the case with $n_e = 0$, consistently with the development of the self-induced flavor conversions (see Fig. 4.7). In particular, the instability happens when $n_e \sim n_{\bar{\nu}_e}$. Moreover, the peak value of κ in these cases reaches at most ~ 0.5, exhibiting a slower growth of the instability with respect to the case with $n_e = 0$. Finally, we discuss the case *(c)* in which we also take into account the flavor-dependent forward-peaked neutrino angular distributions. We find that the κ function is further suppressed with respect to the half-isotropic case and this is consistent with the weaker ν-ν strength for forward-peaked distributions, leading to a more stable system under the effect of the matter. We comment that at $t_{\rm pb} = 0.325$ s when the accretion is ending, the effect of the angular-distributions is less pronounced, since these become less forward-enhanced. As last remark, we mention that we applied the stability analysis also to the case of a 18.0 $M_\odot$ iron-core supernova, finding a very good agreement with what obtained with the multi-angle simulations.

8.8 $M_\odot$ O-Ne-Mg core We remind the reader that this model is characterised by an absence of an extended accretion phase, since the explosion succeeds very shortly after the core-bounce. From the Fig. 4.10 we have realized that the matter suppression of self-induced flavor conversions is never complete, since the matter density is very low with respect to iron-core progenitor. In the Fig. 4.13 we plot the corresponding radial evolution of the κ function, for the *(a)*, *(b)*, *(c)* cases introduced before. For the case *(a)* with $n_e = 0$ (dashed curves) we find again a perfect agreement between the peak of the κ function and the onset of the flavor conversions in Fig. 4.10.

Concerning the matter case, we first realize that the presence of non-trivial angular distributions *(c)* (dotted curves) does not further suppress the instability with respect to the case with a half-isotropic emission *(b)* (continuous curves). This different behavior with respect to the case of 10.8 $M_\odot$ SN model, is consistent with the Fig. 4.11, in which the angular spectra of different flavors for the 8.8 $M_\odot$ SN are significantly less forward-peaked than in the case of the 10.8 $M_\odot$ SN. This produces a less pronounced effect

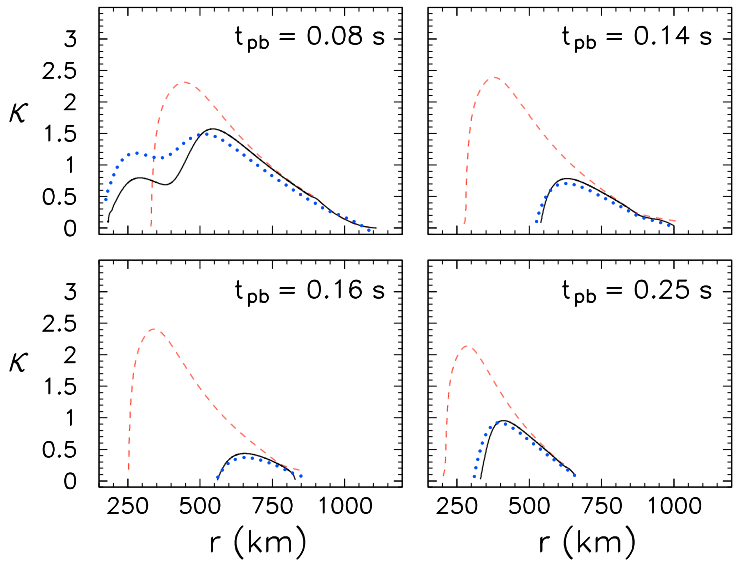

Figure 4.13: 8.8 $M_\odot$ progenitor mass. Radial evolution of the κ function at different post-bounce times for different cases: *(a)* $n_e = 0$ for a half-isotropic neutrino emission (dashed curves), *(b)* in presence of matter effects, with a half-isotropic neutrino emission (continuous curves), *(c)* in presence of matter effects with flavor-dependent angular distributions (dotted curves). Quasi-thermal ν energy spectra are assumed (see the text for details).

on the flavor stability. Moreover, referring to the Fig. 4.13, at $t_{\rm pb} = 0.08$ s (when $n_{\bar{\nu}_e} \lesssim n_e$) the κ function presents a peculiar shape due to the interplay between the self-induced and the matter effects with a comparable strength. The κ curve broadens at smaller r with respect to the case with $n_e = 0$. Even if the peak of κ is slightly reduced by the matter effects, its position is consistent with the onset of the flavor conversions found numerically. At later times, when n_e dominates over $n_{\bar{\nu}_e}$, the matter suppression becomes more relevant but never as strong as in the case of the iron-core SNe since at most $n_e \gtrsim 2n_{\bar{\nu}_e}$. Also in this case, the matter effect shifts the start of the oscillations at larger radii.

4.5 Phenomonelogical consequences

Summarizing, taking as benchmark the matter profiles from the recent long-term core-collapse SN simulation of the Basel/Darmstadt group, we have performed a detailed multi-angle numerical study and a stability analysis of the neutrino flavor evolution for different progenitors SN masses. In

all the cases examined, the electron density is never negligible with respect to the neutrino density during the accretion phase and, consequently, the trajectory-dependent matter effects always influence the development of the self-induced transformations. We found that during the accretion phase both the condition of matter suppression ($n_e \gg n_\nu$) and matter-induced decoherence ($n_\nu \sim n_e$) are realized. Matter suppression has been obtained also in [105] using progenitor SN models from the Garching. In the past [104, 77] it has been argued that swaps of neutrino fluxes between electron and non-electron flavors in the deepest SN regions could increase the neutrino energy deposition and hence the neutrino heating revitalizing the standing bounce shock and triggering the neutrino-driven explosions. We have shown that the occurring of the matter suppression of flavor conversions at high densities, behind the shock front, rules out this possibility to revitalise the shock. Finally, since the time evolution of the neutrino oscillation probability during the accretion phase is significantly different with respect to the case of the iron-core supernovae here studied, this could allow the distinction of a O-Ne-Mg-core SN from a iron-core SN, in the case of the detection of a future galactic event.

The matter suppression of collective oscillations during the accretion phase would be a benefit in order to diagnose the neutrino mass hierarchy exploiting the ordinary MSW effects on the SN accretion burst [see Sec. 3.2]. At this regard it has been proposed the rise-time of the SN neutrino signal [108], or the Earth matter effect [109] during the accretion phase have been suggested as possible observables sensitive to the ν mass hierarchy.

Chapter 5

Introduction to neutrinos in cosmology

The Early Universe offers another, different environment to test neutrino properties in high-density conditions. Indeed Big Bang Nucleosynthesis (BBN), baryogenesis, Cosmic Microwave Background (CMB) radiation, Large Scale Structure formation (LSS), lepton asymmetry could be essentially influenced by neutrino oscillations and non-zero neutrino mass. In particular, cosmological neutrino flavor conversions are a fascinating problem involving collisional damping, refractive effects from charged leptons and neutrino self-interactions and they can play a considerable role in the dynamics of the primordial Universe. In this context, I extensively worked on the flavor conversions among active and sterile neutrinos in the Early Universe and on their impact on different cosmological observables. In this Chapter we will revise the cosmological framework in which our study has been developed. We will also present different cosmological observables that can be affected by active-sterile neutrino oscillations. Our presentation is based on [110] and on [111], to which we address the reader for a more exhaustive treatment.

5.1 The isotropic and homogenous Universe

Historical and current observations support the idea of an expanding Universe, which can be elegantly described in terms of the Friedmann and Lemaitre solution of Einstein equations. In particular the large-scale homogeneity and isotropy and an almost perfect black-body spectrum of cosmic microwave background (CMB) radiation further strengthen the idea that on sufficiently large scales, and at earlier times, the Universe is widely homogeneous and isotropic. The assumptions of spatially homogeneity (phys-

ical conditions are the same at every point of a fixed time hypersurface) and isotropy (they are independent of direction at any given point), which found their formulation in the Cosmological Principle, lead to the well known Friedmann-Robertson-Walker (FRW) expression:

$$\mathrm{d}s^2 = g_{\mu\nu}\mathrm{d}x^\mu \mathrm{d}x^\nu = -\mathrm{d}t^2 + a^2(t)\left[\frac{\mathrm{d}r^2}{1-kr^2} + r^2(\mathrm{d}\theta^2 + \sin^2\theta \mathrm{d}\phi^2)\right], \quad (5.1)$$

where the coordinate t, proper time measured by a comoving observer (i.e. with constant spatial coordinates ρ, θ, ϕ as time flows) is the "physical time", $a(t)$ is the scale-factor and $k = 1, 0, -1$ determines the spatial curvature for closed, flat and open Universe respectively. The dynamics of the expansion is completely encoded in the time-dependent function $a(t)$ which appears in the metric components $g_{\mu\nu}$. These are the dynamical variable in General Relativity and satisfy the Einstein equations

$$G_{\mu\nu} = R_{\mu\nu} - \frac{1}{2}Rg_{\mu\nu} = -8\pi G_N T_{\mu\nu} + \Lambda g_{\mu\nu} \quad (5.2)$$

where $R_{\mu\nu}$ and R are the Ricci tensor and scalar, respectively and Λ is the Einstein cosmological constant, G_N the Newton constant. Finally, $T_{\mu\nu}$ is the stress-energy tensor of all matter species which fill the Universe. This tensor is symmetric and is covariantly conserved, $\nabla_\mu T^{\mu\nu} = 0$, where ∇ denotes the covariant derivative. In most of the cases the matter can be describes as a perfect fluid characterised by a energy density ϵ, pressure P and 4-velocity u_μ:

$$T^\mu_\nu = (\epsilon + p)u^\mu u_\nu + P\ \delta^\mu_\nu \quad (5.3)$$

The spatial part has to be isotropic consistently with the metric used and the constituents of the fluid have to be comoving in the cosmological rest frame, implying

$$T^0_0 = -\epsilon\ , \qquad T^i_j = P\ \delta^i_j\ . \quad (5.4)$$

Information on the particular fluid considered is encoded into the equation of state, relating pressure and energy density, $P = P(\epsilon)$. For radiation (relativistic particles) $P = \epsilon/3$, while for matter (nonrelativistic particles), $P = 0$. Moreover, the covariant conservation of $T^{\mu\nu}$ for a perfect fluid leads to the *conservation law for the expanding universe*

$$\dot{\epsilon} + 3\frac{\dot{a}}{a}(\epsilon + p) = 0. \quad (5.5)$$

Applying the Einstein equations to cosmology, given the previous form of the stress-energy tensor and considering the FRW metric, we obtain the following equations for the dynamics of the expansion:

1. Friedmann equation, which relates the scale factor (and so the Hubble expansion parameter H) to the total energy density of the universe

$$H^2 \equiv \left(\frac{\dot{a}}{a}\right)^2 = \frac{8\pi G_N}{3}\sum_i \epsilon_i - \frac{k}{a^2}, \tag{5.6}$$

   where i indicates all the species.

2. Acceleration rate equation

$$\frac{\ddot{a}}{a} = -\frac{4\pi G}{3}\sum_i (\epsilon_i + 3p_i). \tag{5.7}$$

In terms of the critical density

$$\epsilon_c = \frac{3H^2}{8\pi G_N} \tag{5.8}$$

the Friedmann equation can be written in the form

$$\Omega(a) = \frac{\epsilon_{tot}}{\epsilon_c} = 1 + \frac{k}{H^2 a^2} \tag{5.9}$$

where $\Omega(a)$ is the total energy density in unit of ϵ_c. A universe filled with a critical energy density is flat ($k = 0$).

5.2 Equilibrium Thermodynamics

For much of its history, the Early Universe has been in thermal equilibrium to a good approximation. Considering a fluid composed by different particles, the equilibrium is established by interactions processes such as scatterings, which redistribute particle momenta and are crucial to reach *kinetic equilibrium*, and interactions where the number of particles of a given species is not conserved, such as pair annihilations, which keep the *chemical equilibrium* among different species. Since the Universe is expanding, equilibrium is maintained if the rate of microscopic interactions Γ is larger than the expansion rate H:

$$\Gamma > H \qquad \Rightarrow \qquad \text{Equilibrium}$$

In this case the evolution of the system is quasi-static, and can be considered as a sequence of different thermodynamic equilibrium phases with a temperature T decreasing as a^{-1}. It is then possible a description based on

macroscopic quantities such as the number density, the energy density and pressure defined using the methods of the statistical mechanics. We start with the phase space-distribution function $f(\mathbf{x}, \mathbf{p}, t)$, [1] which gives the number of particles at a given point and at a given time. For a homogeneous and isotropic background the distribution function depends only on the time and on the modulus of momentum. Integrating over the physical volume we obtain the particle number density

$$n(t) = g \int \frac{\mathrm{d}^3 p}{(2\pi)^3} f(p,t) \tag{5.10}$$

and, similarly, the diagonal terms of the energy-stress tensor

$$T_0^0 = -\epsilon = -g \int \frac{\mathrm{d}^3 p}{(2\pi)^3} E f(p,t) \tag{5.11}$$

$$T_i^i = P = g \int \frac{\mathrm{d}^3 p}{(2\pi)^3} \frac{p^2}{3E} f(p,t) \tag{5.12}$$

where g is the number of internal degrees of freedom, such as helicity.

For a species i in equilibrium, the phase space distribution function f is given by the Fermi-Dirac (FD) or Bose-Einstein (BE) distribution:

$$f_i(p,T) = \frac{1}{e^{\left(\frac{E_i - \mu_i}{T_i}\right)} \pm 1} \tag{5.13}$$

where $+/-$ corresponds to the FD/BE statistics and μ_i the chemical potential of the species, typically parametrized in terms of $\xi_i = \mu_i/T_i$. From these equilibrium distributions we obtain the number density, the energy density and the pressure for the following cases:

- *relativistic limit ($T \gg m, \mu$)*

$$n_i = \begin{cases} (3/4)(\zeta(3)/\pi^2) g_i T_i^3 & \text{(FD)} \\ (\zeta(3)/\pi^2) g T^3 & \text{(BE)} \end{cases} \tag{5.14}$$

$$\epsilon_i = \begin{cases} (7/8)(\pi^2/30) g_i T_i^4 & \text{(FD)} \\ (\pi^2/30) g T^4 & \text{(BE)} \end{cases} \tag{5.15}$$

$$P_i = \epsilon_i/3 \tag{5.16}$$

where $\zeta(3)$=1.202.

[1] $p = |\mathbf{p}|$ is the physical momentum such that $E = \sqrt{p^2 + m^2}$

- non-relativistic limit ($T \ll m$) and $\mu \ll m$

$$n_i \sim g_i \left(\frac{m_i T_i}{2\pi}\right)^{3/2} e^{(-m_i \pm \mu_i)/T_i} \tag{5.17}$$

$$\epsilon_i \sim m_i n_i + \frac{3}{2} T_i n_i \tag{5.18}$$

$$P_i \sim T_i n_i \ll \epsilon_i. \tag{5.19}$$

It is useful to introduce the particle-antiparticle asymmetry of a fermionic species, in particular for each neutrino flavor $\alpha = e, \mu, \tau$ it writes

$$L_\alpha = \frac{n_\alpha - n_{\overline{\alpha}}}{n_\gamma} = \frac{1}{12\zeta(3)} \left(\frac{T_\nu}{T_\gamma}\right)^3 (\pi^2 \xi_\alpha + \xi_\alpha^3) \ . \tag{5.20}$$

with T_γ and T_ν the photon and neutrino temperatures, respectively. When the thermal equilibrium holds, the entropy per coming volume is conserved. Introducing the entropy density s, which scales as $\sim a^{-3}$,

$$s \equiv \frac{S}{V} = \frac{\epsilon + P}{T}, \tag{5.21}$$

the total entropy density in relativistic species can be written as

$$s_R = \frac{4}{3}\epsilon_R \equiv g_s \frac{2\pi^2}{45} T^3, \tag{5.22}$$

where for vanishing chemical potential

$$g_s = \sum_{i,\text{boson}} g_i \left(\frac{T_i}{T_\gamma}\right) 3 + \frac{7}{8} \sum_{j,\text{fermion}} g_j \left(\frac{T_j}{T_\gamma}\right)^3 . \tag{5.23}$$

At $T \sim m_i$, the i-th species becomes non-relativistic and its contribution becomes negligible, leading to a decrease of g_s. All the other species which are still in thermal equilibrium with the i particles are reheated by the entropy released by the $i - \bar{i}$ annihilations.

5.2.1 Out of equilibrium: Boltzmann equation

Even if the Universe has been mostly in equilibrium, luckily there have been a number of relevant departures from thermal equilibrium, such as neutrino and background radiation decouplings, primordial nucleosynthesis, etc.

As seen before, a rough criterion to establish if a fluid of particles is coupled to the primordial plasma is given by the comparison of the interaction

rate of the particles with the expansion rate of the Universe. Even if this criterium provides a reliable estimate of the decoupling temperature, as we will see later, a proper description of the phenomenon is obtained following the evolution of the phase space particle distribution function, governed by the Boltzmann equation

$$\hat{L}[f] = \hat{C}[f] \tag{5.24}$$

where $\hat{L}$ is the Liouville operator and $\hat{C}$ is the collisional integral operator. The homogeneity and isotropy assumptions of the FRW universe imply that the phase space distribution function depends only on time and on the modulus of the momentum, p, (or equivalently on energy E), $f(p,t)$. The relativistic generalization of the Liouville operator assumes the form:

$$\hat{L}[f((p,t)] = E\left(\frac{\partial f(p,t)}{\partial t} - Hp\frac{\partial f(p,t)}{\partial p}\right). \tag{5.25}$$

In terms of the number density of the species a,

$$n_a(t) = g_a \int \frac{\mathrm{d}^3 p}{(2\pi)^3} f_a(p,t) \tag{5.26}$$

and integrating by parts, the Boltzmann equation can be written as

$$\dot{n}_a + 3Hn_a = g_a \int \frac{\mathrm{d}^3 p}{(2\pi)^3\ E_a} \hat{C}[f] \tag{5.27}$$

with g_a the number of internal degrees of freedom of the species a. The term $\hat{C}[f]$ depends on the distributions of the all particles interacting with a. For its expression we consider, for simplicity, the particular case of two-body processes $a + b \leftrightarrow c + d$:

$$\begin{aligned}\hat{C}[f_a; f_b, f_c, f_d] = \frac{1}{E_a}\int \mathrm{d}\pi(p_b)\mathrm{d}\pi(p_c)\mathrm{d}\pi(p_d)(2\pi)^4\delta^{(4)}(p_a + p_b - p_c - p_d) \\ \times \left[|\mathcal{M}_{cd,ab}|^2 f_c(p_c,t) f_d(p_d,t) - |\mathcal{M}_{ab,cd}|^2 f_a(p_a,t) f_b(p_b,t)\right],\end{aligned} \tag{5.28}$$

where we have neglected all the quantum statistical factor. $\mathcal{M}$ denotes the invariant amplitude for the processes and $\mathrm{d}\pi(p)$ is the relativistic invariant measure

$$\mathrm{d}\pi(p) = \frac{\mathrm{d}^3 p}{(2\pi)^3\ 2E(p)}. \tag{5.29}$$

In the Boltzmann equation [Eq. (5.27)], the term $3Hn_a$ accounts for the dilution effect due to the expansion of the Universe and the collisional term accounts for interactions that change the number of particles a. In absence of interactions, the solution is $n_a \propto a^{-3}$.

5.3 Neutrino decoupling and relic neutrino formation

In the Early Universe the three flavour active left-handed neutrinos ν_α, $\alpha = e, \mu, \tau$, and their antiparticles are thermally excited in the primeval plasma of particles, being in thermal equilibrium with charged leptons, baryons and photons by weak interactions. In this regime the neutrino distribution is the Fermi-Dirac one, with a negligible contribution of their mass to the energy:

$$f_{\nu_\alpha}(p) = \frac{1}{e^{\left(\frac{p}{T} - \xi_\alpha\right)} + 1}\ , \qquad f_{\overline{\nu}_\alpha}(p) = \frac{1}{e^{\left(\frac{p}{T} + \xi_\alpha\right)} + 1}\ , \tag{5.30}$$

with p the physical momentum and $T = T_\nu = T_\gamma$. The neutrino (and antineutrino) energy density and pressure are given by the expression Eq. (5.15) and Eq. (5.19).

Due the expansion of the Universe, the temperature decreases and the neutrino interaction rate decreases faster than the Hubble rate.
When $\Gamma_\nu(T) < H(T)$ occurs, the weak rates are then inefficient to keep neutrinos in equilibrium: the neutrino species decouple from the electromagnetic plasma. The leading processes contributing to equilibrium are scattering over relativistic electrons/positrons and pair conversions, $\nu e \leftrightarrow \nu e$, $\overline{\nu}\nu \leftrightarrow e^+e^-$. The corresponding (thermally averaged) cross section times velocity is of the order of:

$$\langle \sigma v \rangle \sim G_F^2 T^2. \tag{5.31}$$

Therefore, the weak interaction rate for neutrinos is given by

$$\Gamma_\nu \sim \langle \sigma v \rangle\ n_e \sim G_F^2 T^2\ T^3 \sim G_F^2 T^5, \tag{5.32}$$

with n_e is the electron/positron number density.

The Hubble parameter in the radiation-dominated epoch, given by the Eq. (5.47), is expressed here in terms of the Planck mass, m_{Pl}.

$$H(T) \sim \sqrt{g_*}\frac{T^2}{m_{Pl}} \tag{5.33}$$

where g_* is the effective number of degrees of freedom. We will define it later [Eq. 5.46]. The decoupling temperature of neutrinos is defined as the temperature at which the two rates become equally: $H(T_{\nu,d}) = \Gamma_\nu(T_{\nu,d})$. It is given by

$$T_{\nu,d} = \left(\frac{\sqrt{g_*}}{G_F^2 m_{Pl}}\right)^{1/3} \sim g_*^{1/6} \sim \mathcal{O}(1\ \text{MeV}). \tag{5.34}$$

A more accurate computation of the decoupling temperature comes from the solution of the kinetic equation in the limit of *instantaneous decoupling* [112, 113], gives the the following values

$$T_{\nu_e,d} = 1.87 \text{ MeV}, \qquad T_{\nu_{\mu/\tau},d} = 3.12 \text{ MeV}, \tag{5.35}$$

. The slightly smaller value for the ν_e species is due to the fact they remain in equilibrium a bit longer since they can also have CC interactions (in addition to the NC) with the plasma composed by only electrons and positrons at that temperature.

After the decoupling, neutrinos freely propagate becoming transparent to the Universe forming the *Cosmic Neutrino Backgorund* (CNB). They represent an hot relic, in the sense that they decouple when they are relativistic particles. In this way their FD distribution remains unchanged except for the effect of redshift of the physical momentum. In particular, the distribution in terms of physical momenta is entirely specified by a temperature parameter which scales as $T_{\nu,d}a_d/a$, with a_d the scale factor at the decoupling. Actually some small thermal distortions will be imprinted in the neutrino distribution with respect to a standard FD function [114, 115] as a result of e^-- e^+ annihilation occurring at $T \sim m_e$. [2] Indeed the decoupling of neutrinos is not really instantaneous but it takes place over an extended range of time and more energetic neutrinos will be kept in equilibrium longer.

Concerning the temperature of the photons T_γ, it simply scales as a^{-1} as long as electron/positron pairs are relativistic. When the temperature drops below the electron mass m_e, the electron and positrons annihilate heating the photons. Assuming the neutrinos undisturbed by pair annihilations (except for a small fraction due to the non-instantaneous decoupling but not taken into account here), the neutrino to photon temperature ratio assumes the value [see Fig. (5.1)]:

$$\frac{T_\nu}{T_\gamma} = \left(\frac{4}{11}\right)^{1/3}. \tag{5.36}$$

Today, the number density of cosmic neutrinos for each flavour is $n_\nu = 56 \text{ cm}^{-3}$. Even if they are not detected yet, they are well established by cosmological observables at different epochs, contributing to radiation at early times and to matter at later times.

[2] The final spectrum of ν is not modified if all particles in contact with them are relativistic during the full decoupling period. This is not the case for e^-, e^+ at temperature of annihilation $T_{\text{ann}} \sim m_e$ where the effect of the m_e becomes important.

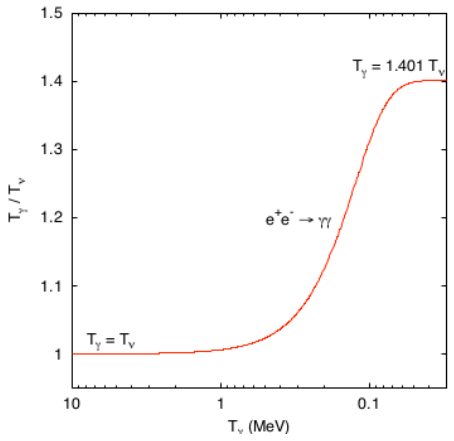

Figure 5.1: Evolution of the the neutrino to photon temperature ratio during the process of e e^--e^+ annihilations.

5.4 Big-Bang Nucleosynthesis

Big Bang Nucleosynthesis (BBN) is the epoch of the Early Universe when the primordial abundances of light elements were produced, in particular ^{2}H, ^{3}He, ^{4}He and ^{7}Li offering the oldest picture of the Early Universe and of its evolution up to the MeV scale. Predictions of the abundances of the light elements, based on weak and nuclear processes at the MeV scale or lower, are in good overall agreement with those inferred from observational data, though the latter are still affected by systematics.

Soon after neutrinos decouple, charged-current weak neutron-proton interconversions also become too slow to guarantee the $n-p$ chemical equilibrium. For temperatures below $T_d \sim 0.7$ MeV, the n/p density ratio departs from its equilibrium value and freezes out at the asymptotic value

$$\frac{n_n}{n_p} = \frac{n}{p} = e^{-\frac{\Delta m}{T_d}} \sim \frac{1}{6} \tag{5.37}$$

where $\Delta m = 1.29$ MeV is the neutron-proton mass difference. This ratio is then reduced to the value $n/p = 1/7$ by neutron decays, when the Universe is several hundred seconds old, a time comparable to the neutron lifetime τ_n.

At temperature $T_{BBN} \sim 0.08$ MeV, nuclear reactions burn a relevant fractions of free nucleons into light nuclei, starting from deuterium formation

$$n + p \leftrightarrow D + \gamma. \tag{5.38}$$

At earlier times the newly-formed deuterons are photodissociated by high density and energetic photons. Therefore the large photon-baryon (i.e, nu-

cleon) density ratio $\eta_B^{-1} = (n_B/n_\gamma)^{-1} \sim 10^9$, delays deuterium synthesis until the photo-dissociation process become ineffective (*deuterium bottleneck*).

As soon as deuterium forms, a whole network of nuclear reaction takes place producing heavier nuclei up to ^{7}Li, Fig. 5.2. [3] In particular, the deuterium is quite immediately burned into ^{4}He, which has the largest binding energy per nucleon among light nuclei [111, 116]. A crude but accurate esti-

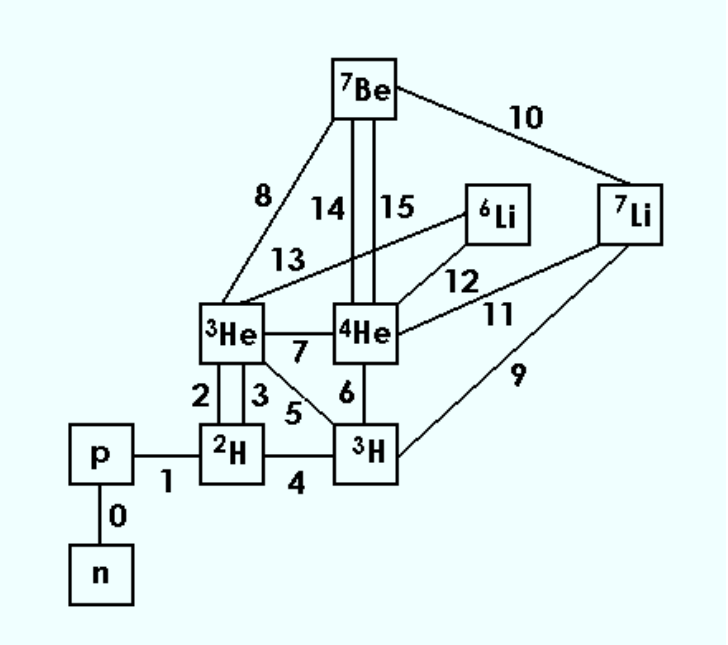

Figure 5.2: Chain of the most relevant nuclear reaction for the synthesis of the primordial abundance.

mate of the abundance ^{4}He, main outcome of the BBN, is obtained assuming that basically all neutrons are captured in Helium nuclei, gives the *Helium mass fraction* Y_P:

$$Y_P = \frac{4n_{^4\mathrm{He}}}{n_B} = \frac{4n/2}{n+p} = \frac{2n/p}{1+n/p} \simeq 0.25. \tag{5.39}$$

A more accurate determination of the primordial abundances of ^{4}He and especially of the other light nuclei requires the numerical solution of a set of coupled kinetic equations for the nuclei together with the equation for the expansion of the Universe and conservation equation of both total stress-energy tensor and baryon number [117]. The calculation of the primordial

[3] The production of heavier nuclei such as ^{12}C and ^{16}O, is disfavored since there are not stable isotopes with $A = 5, 8$ and moreover, Coulomb barrier starts to be significant.

abundance is affected by experimental uncertainties in the nuclear reaction rates and the free neutron lifetime τ_n. In particular the latter is the most important parameter in determine Y_P. The experimental value is $\tau_n^{\rm exp} = 880.1 \pm 1.1$ s [14].

Cosmological neutrinos influence the production of the primordial light elements in two ways. First, ν_e and $\overline{\nu}_e$ directly participate in the charged current weak interactions which rule the neutron/proton chemical equilibrium:

$$\begin{aligned} &(a)\ \ \nu_e + n \to e^- + p\ \ , && (d)\ \ \overline{\nu}_e + p \to e^+ + n \\ &(b)\ \ e^- + p \to \nu_e + n\ \ , && (e)\ \ n \to e^- + \overline{\nu}_e + p \\ &(c)\ \ e^+ + n \to \overline{\nu}_e + p\ \ , && (f)\ \ e^- + \overline{\nu}_e + p \to n \end{aligned} \tag{5.40}$$

To get an accurate theoretical prediction for light-element abundances, the processes $(a) - (f)$ require a careful and accurate treatment. Since ν_e and $\overline{\nu}_e$ enter the BBN equations at a fundamental level, any change in the neutrino momentum distributions can shift the n/p ratio freeze out temperature and then modifies the primordial ^{4}He abundance. An example is represented by electron neutrino-antineutrino asymmetry parameterized by the chemical potential ξ_e, which leads to the chemical equilibrium condition

$$\frac{n}{p} \sim e^{\left(-\frac{\Delta_m}{T} - \xi_e\right)}\ . \tag{5.41}$$

Second, cosmological neutrinos of each flavor contribute to the radiation energy density that governs the expansion rate of the Universe before and during BBN epoch. Changing the expansion rate alters the n/p ratio at the onset of BBN and hence the light element abundances, especially the ^{4}He abundance. The expression of the radiation energy density in terms of relativistic degree of freedom, included neutrinos, is discussed in the next section.

Light element observations Extracting primordial yields from measurements performed in astrophysical environments is not a trivial task, since the latter are altered by the stellar activity throughout the history of the Universe and then they are evolved with respect to the primordial composition. Indeed, the abundances are observed at much later epochs after stellar nucleosynthesis has already begun, which can also produce heavy elements such as C, N, O, and Fe. For this reason, one considers astrophysical sites with low metal abundances, in order to measure light element yields which are closer to primordial ones. For sake of brevity and also due to the relevance for our work, we will discuss only the Deuterium and Helium abundances.

- *Deuterium.* It is believed that astrophysical sources of deuterium are absent due to its burning in the stellar evolution processes. For this reason, any astrophysical deuterium measurement can represent a lower

bound for its primordial abundance. The best criterium to evaluate the deuterium abundance is the D/H ratio from the observation of the absorption lines of hydrogen-rich clouds at high redshifts, on the light of background quasars. This is a difficult measurement which requires the right combination of redshift, hydrogen column density and internal velocity structure of the absorbing gas. Consequently, there are only few measurements that are useful for the primordial deuterium determination. An average value of the D/H ratio was obtained considering seven determinations from different quasar absorption system [118]

$$D/H = (2.87 \pm 0.22) \times 10^{-5}. \tag{5.42}$$

More recently, analyzing a high-quality spectrum of the metal-poor damped Lyman alpha system (DLA), which presents near-ideal properties for an accurate deuterium determination, was found the following value for D/H [119]

$$D/H = (2.535 \pm 0.05) \times 10^{-5}. \tag{5.43}$$

- *Helium.* The situation concerning the primordial abundance of ^{4}He is different form the deuterium case, being the helium content enriching by the stellar burning. This process is correlated with the metallicity of the astrophysical objects due to the fact that also the heavier nuclei are the product of nuclear processes. Since in the Early Universe the amount of nuclei heavier then ^{7}Li is negligible, the Helium mass fraction Y_P is obtained extrapolating the Y_P - O/H and Y_P - N/H correlations to zero metallicity and then correcting for a model-dependent star evolution. In particular, very important are the observations of helium and hydrogen emission lines from the recombination of ionized hydrogen and helium in low-metallicity extragalactic HII regions. The estimated value for Y_P together with the possible systematic effects which dominate the uncertainty is given by [196]

$$Y_P = 0.2565 \pm 0.0010(\text{stat.}) \pm 0.0050(\text{syst.}). \tag{5.44}$$

5.5 Radiation content of the Universe and $N_{\mathbf{eff}}$

The total energy density and pressure of radiation can be expressed in terms of the photon energy density for each polarisation degree of freedom

as follows:

$$\epsilon_R = 3P_R = g_* \frac{\pi^2}{30} T_\gamma^4, \tag{5.45}$$

where g_* is the effective number of degrees of freedom contributing to ϵ_R. For particles with relativistic FD or BE distributions and $\xi = 0$, one has:

$$g_* = \sum_{i,\text{boson}} g_i \left(\frac{T_i}{T_\gamma}\right)^4 + \frac{7}{8} \sum_{j,\text{fermion}} g_j \left(\frac{T_j}{T_\gamma}\right)^4 , \tag{5.46}$$

where the additional factor of 7/8 comes from the differences in the first moments of relevant distributions and we allow for different temperatures for different species. The Friedmann equation [Eq. (5.6)], restricting to a spatially-flat Universe favored by present observations, gives the Hubble parameter during the radiation-dominated era:

$$H(T) = \sqrt{\frac{8\pi G_N}{3}\epsilon_R} = \sqrt{\frac{8\pi G_N}{3} g_* \frac{\pi^2}{30} T_\gamma^4} \tag{5.47}$$

At temperatures 1 MeV $\leq T \leq$ 100 MeV, the equilibrium plasma consists of photons, electrons and positrons and three types of neutrinos and antineutrinos, therefore the effective number of relativistic species is $g_* = 10.75$.

After the $e^+ - e^-$ annihilation, for temperature $T < m_e$, the remaining relativistic degrees of freedom are photons and the three light neutrinos. The Eq. (5.45) reads:

$$\epsilon_R = \epsilon_\gamma \left(1 + \frac{7}{8}\left(\frac{4}{11}\right)^{4/3} 3\right) , \tag{5.48}$$

where we remark that the factor 4/11 comes form the heating of the photons due to the $e^+ - e^-$ annihilation. However the above expression holds strictly if: the limit of instantaneous neutrino decoupling is considered, the neutrino distributions are standard FD function with zero chemical potential and of course in absence of other relativistic species. In order to take into account possible deviation from these assumption it is useful to define the radiation density in terms of the *effective number of neutrino species* N_{eff}, which represent the non electromagnetic radiation content of the Universe:

$$\epsilon_R = \epsilon_\gamma \left(1 + \frac{7}{8}\left(\frac{4}{11}\right)^{4/3} N_{\text{eff}}\right) \tag{5.49}$$

The Standard Model expectation (plus active neutrino oscillations) for this parameter is [115]

$$N_{\text{eff}}^{\text{SM}} = 3.046. \tag{5.50}$$

where the slightly excess with respect to 3 is to due to the non instantaneous neutrino decoupling thanks to which neutrinos share a small part of the entropy release after the $e^+ - e^-$ annihilation. This process produces non-thermal distortions on the neutrino spectra especially for ν_e. This standard value is only marginally modified even accounting for non standard neutrinos-electrons interactions [121].

Furthermore, the presence of a cosmological neutrino-antineutrino asymmetry, when neutrinos are still interacting, implies that their spectrum presents a FD form characterized by neutrino degeneracy parameters $\xi_\alpha = \mu_\alpha/T_\nu$, $\alpha = e, \mu, \tau$ leading to a contribution given by

$$N_{\rm eff} = 3 + \sum_\alpha \left[\frac{30}{7} \left(\frac{\xi_\alpha}{\pi} \right)^2 + \frac{15}{7} \left(\frac{\xi_\alpha}{\pi} \right)^4 \right]. \tag{5.51}$$

This means that, even without additional relativistic particles, a non-vanishing flavor neutrino asymmetry leads to $N_{\rm eff} > 3$ (even if a degeneracy parameter of order $\xi_\alpha \geq 0.3$ is needed to start having a sizeable contribution). However, a combined analysis of active neutrino flavor oscillations and BBN has led to an almost standard value for the effective number also in the presence of neutrino asymmetries, with $N_{\rm eff} < 3.2$ [122]. We will come back later on the role of the neutrino-antineutrino asymmetry on $N_{\rm eff}$, especially in relation to the active-sterile neutrino oscillations.

The most important question concerning $N_{\rm eff}$, is the possible existence of other light particles in addition to the three standard neutrinos. In this case we can parametrize the radiation content Eq. (5.49) as follows

$$\epsilon_R = \epsilon_\gamma \left[1 + \frac{7}{8} \left(\frac{4}{11} \right)^{4/3} (3.046 + \Delta_{N\rm eff}). \right] \tag{5.52}$$

The extra radiation may be accounted for by different particles, such as sterile neutrinos totally or partially thermalised, axions and axion-like particles, hidden sector photons, majorons, or even gravitons [123, 124, 125, 126, 127]. Among them, in our study, we consider the presence of light sterile neutrinos ($\Delta m_s^2 \leq 1$ eV^2) oscillating with the active ones.

5.6 Extra-radiation: cosmological observable effects

Cosmological measurements represent a powerful tool to probe the number of relativistic degrees of freedom $N_{\rm eff}$ and measuring it is still of great

interest today. Indeed, the primordial nucleosynthesis and the spectra of both CMB anisotropies and matter fluctuations can provide strong constrains on the radiation content ϵ_R and therefore on $N_{\rm eff}$. In particular, this number enters directly the Hubble expansion rate in the radiation dominated regime, Eq. (5.47), affecting the Early Universe observables.

- *Impact on BBN*

  Focusing on the sterile neutrinos, if these additional states are produced before the active-neutrino decoupling, they could acquire quasi-thermal distributions (depending of their temperature) and behave as extra degrees of freedom at the time of primordial nucleosynthesis. This would anticipate weak interaction decoupling leading to a larger neutron-to-proton ratio, eventually resulting into a larger ^{4}He fraction. Furthermore, sterile neutrinos can distort the ν_e phase space distribution via flavor oscillations with the active ones, leading to a possible effect on the Helium and Deuterium abundance. We will examine this aspect in more detail in the following chapter, presenting our results.

- *Impact on CMB and LSS*

  Unlike BBN, both the later time observables, CMB anisotropies and LSS distributions, are not sensitive to the flavor content of the neutrino sector, but only to $N_{\rm eff}$ and to the mass of the neutrino species.

  If additional degrees of freedom are still relativistic at the time of CMB formation, $N_{\rm eff}$ can be constrained by a detailed study of the CMB angular power spectrum, especially when combined with other cosmological probes. In the Fig. 5.3 by the 9-years Wilkinson Microwave Anisotropy Probe Satellite (WMAP9) results [128], are represented the effects of changing the $N_{\rm eff}$ value on the CMB spectrum:

  • A first effect of increasing $N_{\rm eff}$ is the decrease of the comoving sound horizon at the decoupling, r_s, and so the decrease of the angular size of the acoustic scale which determines the peak positions. However this effect is degenerate with the present-day Hubble parameter H_0.

  • Another important effect of extra radiation density is the delay of the epoch of matter-radiation equality (z_{eq}) and thus the enhancement of the first and second peaks via the Early Integrated-Sachs-Wolfe (ISW) effect.[4] This effect can be compensated by increasing the cold dark matter density Ω_{DM}, which brings the matter-radiation equality epoch back

[4]This effect represents an additional redshift of the photon temperature given by the fact that, at time of decoupling, the Universe is still near the beginning of the matter domination and there is still enough radiation around.

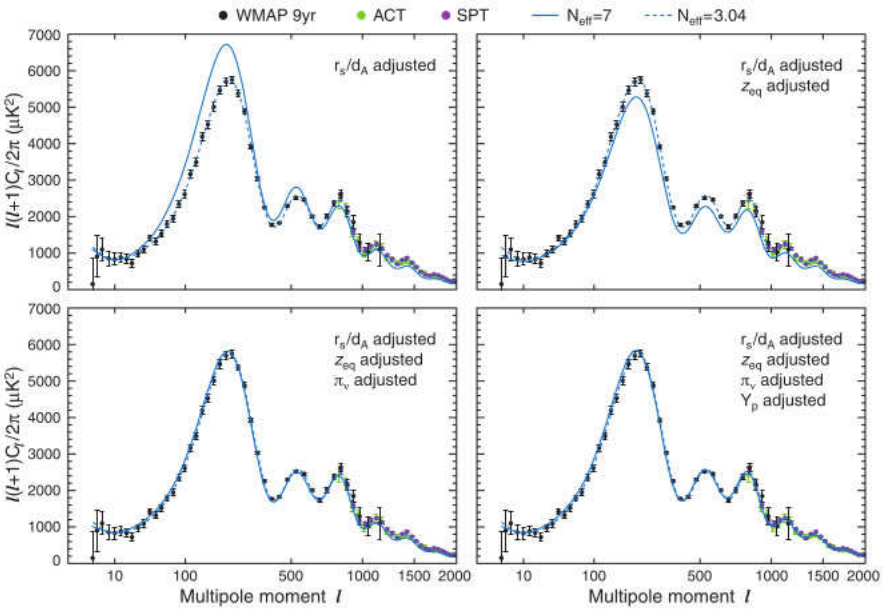

Figure 5.3: Illustration of four effects in the CMB anisotropy that can compensate for a change in $N_{\rm eff}$. The nine-year WMAP data are represented by the filled circles with errors (black), while the ACT data in green [136], and the SPT data in violet [132]. Figure taken from [128].

into agreement. Because of the strong $N_{\rm eff}$-Ω_{DM} and $N_{\rm eff}$-H_0 degeneracies, measurements of the CMB acoustic peaks alone do not completely constrain $N_{\rm eff}$.

• The CMB spectrum is also affected by the anistropic stress (π_ν) of free-streaming relativistic neutrinos, defined by:

$$\pi_{ij} = \int \frac{\mathrm{d}^3\mathbf{p}}{(2\pi)^3} p \left(p_i p_j - \frac{1}{3}\delta_{ij} \right) f(\mathbf{x}, \mathbf{p}, t). \tag{5.53}$$

This stress suppresses the amplitude of higher harmonics ($l > 200$) [129, 130] and is somewhat degenerate with the effects of changing the primordial fluctuation amplitude.

• The problem of the degeneracies can be alleviated combining the CMB measurements with other data such as the baryonic Acoustic Oscillations (BAO) and Hubble Space Telescope (HST) data, and in particular with measurements of the CMB damping tail, occurring at very high multipoles of the spectrum ($l \geq 1000$), by Atacama Cosmological Telescope (ACT) and South Pole Telescope (SPT) experiments

[131, 132]. Indeed, increasing the expansion rate increases the diffusion length of the photons relative to the sound horizon, [5] which enhances the Silk damping of the small-scale anisotropy. However this effect is degenerate with the Helium abundance [133].

Further information can came from the effect of the neutrino mass on the LSS. Indeed, small-scale neutrino density fluctuations are damped, in a scale-dependent way, by the free-streaming caused by small neutrino masses [134]. Moreover, other bounds on extra radiation can be derived from a joint constraint analysis on $N_{\rm eff}$ and $\sum m_\nu$, since extra relics could coexist with massive neutrinos or they could themselves have a mass [135].

5.6.1 Present observable constraints

For a long time the WMAP experiment has provided the best constraints on the CMB temperature spectrum for ($l < 1000$), complemented by smaller angular scale ($l > 1000$) observations performed by ACT and SPT experiments. Combing the CMB data with other experiments it is possible to obtain information on the $N_{\rm eff}$ and on the neutrino mass. In the last few years a possible cosmological hint of extra radiation (especially in the form of sterile neutrino) (see e.g. [12, 137]) was found by combining the results in a best fit of WMAP, SDSS II-Baryon Acoustic Oscillations and Hubble Space Telescope data, yielding a 68 % C.L. range on $N_{\rm eff} = 4.34^{+0.86}_{-0.88}$ [138] for a ΛCDM universe. This number has stimulated a long series of investigations on the possible existence of exotic particles, in particular sterile neutrinos. The recent results of WMAP-9 [128], SPT [139] and ACT [140], exploiting the damping tail features at high multipoles, have weakened this evidence to less than 2-σ. Moreover, a recent important contribution in constraining the extra radiation and neutrino mass is represented by the first data release in March 2013 of the Planck collaboration, a satellite experiment with unprecedented sensitivity in the high multipole range. The Planck results prefer a value $N_{\rm eff} = 3.30 \pm 0.27$ at 68 % C.L., compatible with the standard expectation [135], leaving nevertheless the opportunity for an extra species, if combined with the Hubble Telescope data. This discrepancy is due to the smaller Planck value of the Hubble constant ($H_0^{\rm Planck} = (67.3 \pm 1.2)$ km s^{-1} Mpc^{-1}) with respect to the HST one ($H_0^{\rm HST} = (73 \pm 2.4)$ km s^{-1} Mpc^{-1}) [141]. The tension between the CMB estimations and the astrophysical measurements of the Hubble parameter represents a non trivial issue, due to the strong degeneracy between Ω_{DM} and H_0. In particular, the shift

[5] Comoving distance travelled by a wavefront.

necessary to match the HST data would require a large change in Ω_{DM} which is disfavored by the Planck data.

Concerning the BBN constraint on sterile neutrino, one fully thermalized sterile neutrino is still marginally allowed [142, 119]. Then, a value corresponding to two sterile states appears largely excluded [143].

In oder to summarize the results from different experiments, in Table 5.1 we report the different recent constraints on $N_{\rm eff}$ and on neutrino mass.

CMB combined	$N_{\rm eff}$	$\sum_\nu$ (eV)
WMAP9+ACT+SPT; Y_p fixed	3.89 ± 0.67 (68% CL)	< 1.5 (95% CL)
WMAP9+ACT+SPT+BAO+H0; Y_p fixed	3.84 ± 0.40 (68% CL)	< 0.44 (95% CL)
WMAP9+ACT	2.79 ± 0.56 (68% CL)	-
Planck+ WMAP+BAO+ highL	3.30 ± 0.27 (68% CL)	< 0.3 (95% CL)
Planck+ WMAP+BAO+ highL +H0	3.52 ± 0.48 (68% CL)	-
BBN	< 4 (95% CL)	-

Table 5.1: Different recent constraints on $N_{\rm eff}$ and on neutrino mass from data of cosmological observations.

Chapter 6

Active-sterile neutrino oscillations in the Early Universe

In recent years a renewed attention has been devoted to low-mass sterile neutrinos ($m \sim$1 eV), after intriguing but controversial hints coming from precision cosmological measurements and laboratory oscillation experiments. Sterile neutrinos can be produced by oscillations with the active neutrinos in the Early Universe, contributing to the radiation content beyond photons and ordinary neutrinos and leaving possible traces on different cosmological observables. In order to determine the relic abundance of sterile neutrinos, it is necessary an accurate solution of the kinetic equations for the evolution of the active-sterile ensemble. In this context, we performed a detailed study of the kinetic equations for the active-sterile neutrino ensemble, removing several approximations adopted in the previous literature. This goal has required, in addition to an accurate characterization of the physical processes contributing to the neutrino flavor conversions, also the development of advanced numerical codes. All the original results presented in this thesis are included in the following references:

- A. Mirizzi, N. Saviano, G. Miele and P. D. Serpico, "*Light sterile neutrino production in the early universe with dynamical neutrino asymmetries*," Phys. Rev. D **86**, 053009 (2012).
- N. Saviano, A. Mirizzi, O. Pisanti, P. D. Serpico, G. Mangano and G. Miele, "*Multi-momentum and multi-flavor active-sterile neutrino oscillations in the early universe: role of neutrino asymmetries and effects on nucleosynthesis*," Phys. Rev. D **87**, 073006 (2013).

- A. Mirizzi, G. Mangano, N. Saviano, E. Borriello, C. Giunti, G. Miele and O. Pisanti, "*The strongest bounds on active-sterile neutrino mixing after Planck data*," Physic Letter B **726**, 8-14 (2013).

6.1 Light sterile neutrinos and cosmology

As discussed in the Sec. 1.4.3, light sterile neutrinos, $m \sim 1$ eV, mixing with the active ones, have been suggested to solve different anomalous results observed in short-baseline and reactor neutrino experiments. Many analyses have been performed to explain the anomalies and scenarios with one (dubbed "3+1") or two ("3+2") sub-eV sterile neutrinos [55, 57, 144] have been proposed to fit the different data. The search for sterile neutrinos in laboratory experiments is presently open. Indeed, since each experimental measurement has its own systematic uncertainties, it is important to use as many observations as possible to corner sterile neutrinos (see, e.g., [145]). In this context, cosmological observations represent a valid complementary tool to probe these scenarios, being sensitive to the number of neutrinos and to their mass at eV scale (see, e.g., [146, 147, 148]). As discussed in the previous chapter, the CMB measurements slightly favor the existence of some extra radiation and one fully thermalized sterile neutrino is still marginally allowed by BBN. However even a single extra thermalized sterile neutrino with mass $m \sim 1$ eV appears to be inconsistent with mass bounds from CMB and LSS data [12, 137, 149, 150, 58, 135].

Given this partially contradictory situation and the existence of the laboratory anomalies, it is necessary to study the physical conditions under which the sterile neutrino production can actually occur. As already mentioned, sterile neutrinos are produced in the primordial plasma by the mixing with the active species. Therefore, in order to assess their abundance it is necessary to solve the quantum kinetic equations for the the active-sterile oscillations system [60, 151]. This problem has been investigated in a long series of papers (see e.g. [152, 153, 154, 155, 156, 157, 158, 159, 160, 161, 162, 163, 164, 165, 166, 167, 168, 169, 179, 171, 172, 173]), finding a broad range of possible outputs depending on the sterile mass and mixing parameters. Due the numerical challenges of the problem, involving non-linear refractive effects and neutrino scatterings (see Chapter 2), different approximations have been adopted. In particular, most of the previous studies have solved the equations in a simplified (1+1) scenario in which only one sterile neutrino mixes with an active one. Recently, also multi-flavor studies have been performed [168, 172]. In particular, in a (3+2) scheme with mass and mixing parameters as suggested by experimental anomalies, sterile neutrinos would

be completely thermalized in the Early Universe, creating a tension with cosmological observations as has been mentioned above.

The purpose of our work is, therefore, to revisit the production and thermalization of sterile neutrinos in the Early Universe for multi-flavor scenarios, going beyond several approximations used in the previous studies. In particular, motivated by the recent data release of the Planck experiment, we performed an extensive scan of the sterile neutrino parameter space in a 3+1 model, in the range $(10^{-5} - 10^2)\,\mathrm{eV}^2$ for the active-sterile mass splitting Δm^2_{st} and accounting, for the first time, the possibility of two non-vanishing active-sterile mixing angles. Once more we confirm the tension between the cosmological data and the mass and mixing suggested by the laboratory hints, see Sec. 6.4. A possible escape route to relieve this tension would be the suppression of the sterile neutrino production introducing a primordial neutrino asymmetry among the active species. At this regard, in Sec. 6.5 we present our results in (3 +1) and (2+1) scenarios. At first we perform an exploratory investigation solving the evolution equations assuming an equal thermal momentum for all the neutrino ensemble (the so called "average-momentum approximation"). Then we remove this assumption performing for the first time a multi-momentum treatment in a multi-flavor scenario. The impact of active-sterile conversions on the BBN have been also explored.

6.2 Set-up of the flavor evolution

(3+1) neutrino framework In the 3+1 scenario, the flavor neutrino basis is constituted by the three active neutrinos ν_e, ν_μ, ν_τ and by a sterile one ν_s. The flavor eigenstates ν_α are connected to the mass eigenstates ν_i ($i = 1, \ldots 4$, ordered by growing mass) by a unitary matrix $\mathcal{U}$ through [174, 13]

$$\nu_\alpha = \mathcal{U}^*_{\alpha i}\,\nu_i \ , \quad \mathcal{U}\mathcal{U}^\dagger = \mathcal{U}^\dagger\mathcal{U} = I \ , \tag{6.1}$$

Neglecting for the moment arbitrary phases responsible for CP violation effects, the matrix $\mathcal{U}$ can be parameterized as a product of 4×4 Euler rotation matrices R_{ij} acting in the (i, j) mass eigenstate subspace, each one characterized by a mixing angle θ_{ij}. According to [175] one can write

$$\mathcal{U} = R_{34}R_{24}R_{23}R_{14}R_{13}R_{12} \ , \tag{6.2}$$

where the flavor eigenstates are ordered in such a way that $(\nu_e, \nu_\mu, \nu_\tau, \nu_s) = (\nu_1, \nu_2, \nu_3, \nu_4)$ if all angles are vanishing. In the limit of the three mixing angles θ_{i4} vanish, we have

$$\lim_{\theta_{i4}\to 0} \mathcal{U} = \begin{pmatrix} U(\theta_{12}, \theta_{13}, \theta_{23}) & 0 \\ 0 & 1 \end{pmatrix} \ , \tag{6.3}$$

where U is the 3×3 unitary mixing matrix for the active neutrinos as define in the Eq. (1.8).

In our study we fix the values of three active mixing angles to the current best-fit from global analysis of the different active neutrino oscillation data as in the Table (1.2):

$$\sin^2\theta_{12} = \quad 0.307 \ , \quad \sin^2\theta_{23} \quad = 0.398 \ , \qquad \sin^2\theta_{13} = \quad 0.0245 \ . \tag{6.4}$$

Moreover, we neglect CP violating effects in the active sector.

Concerning the mixing angles between the active neutrinos and the sterile one, we assume (according to phenomenological studies) that at most two mixings are non vanishing, in particular we put $\mathcal{U}_{\tau 4} = 0$. We will specify the values chosen later.

Coming to the 4ν mass spectrum, it is parameterized as [176]

$$\mathcal{M}^2 = \mathrm{diag}(m_1^2, m_2^2, m_3^2, m_4^2) = \mathrm{diag}\left(0 \ , +\Delta m^2_{\mathrm{sol}} \ , \Delta m^2_{\mathrm{atm}} \ , \Delta m^2_{\mathrm{st}}\right) \ , \tag{6.5}$$

where the solar and the atmospheric mass-square differences are given

$$\Delta m^2_{\mathrm{sol}}/\mathrm{eV}^2 = 7.54 \times 10^{-5} \ , \quad \Delta m^2_{\mathrm{atm}}/\mathrm{eV}^2 = 2.43 \times 10^{-3}, \tag{6.6}$$

Concerning the values of the sterile mass and mixing parameters, we will specify them later.

(2+1) neutrino framework In order to reduce the numerical complexity of the complete 3+1 problem, sometimes it is useful to characterize the flavor evolution in a simplified (2+1) scenario, composed by only two active neutrino species plus the sterile one. In particular, one can consider two different sub-sectors associated with $(\Delta m^2_{\mathrm{sol}}, \theta_{12})$ and $(\Delta m^2_{\mathrm{atm}}, \theta_{13})$, respectively. After checked that, for the cases analized, there are marginal differences in the flavor evolution in these two sub-sectors, in the following we will refer only to the $(\Delta m^2_{\mathrm{atm}}, \theta_{13})$.

The mass-squared matrix is consequently given in terms of the atmospheric mass-squared difference and of the active-sterile mass splitting:

$$\mathcal{M}^2 = \mathrm{diag}(0, \Delta m^2_{\mathrm{atm}}, \Delta m^2_{\mathrm{st}}). \tag{6.7}$$

6.3 Equations of motion

As discussed in the Chapter 2, a proper characterization of the evolution of a neutrino ensemble, simultaneously mixing and scattering in the Early Universe, requires to use of the density matrix formalism. According to it

the neutrino (antineutrino) ensemble for the scenario (3+1) is expressed in terms of 4×4 density matrices ϱ ($\bar{\varrho}$): [1]

$$\varrho(x,y) = \begin{pmatrix} \varrho_{ee} & \varrho_{e\mu} & \varrho_{e\tau} & \varrho_{es} \\ \varrho_{\mu e} & \varrho_{\mu\mu} & \varrho_{\mu\tau} & \varrho_{\mu s} \\ \varrho_{\tau e} & \varrho_{\tau\mu} & \varrho_{\tau\tau} & \varrho_{\tau s} \\ \varrho_{se} & \varrho_{s\mu} & \varrho_{s\tau} & \varrho_{ss} \end{pmatrix} , \tag{6.8}$$

where, following [66], it has been worthwhile to introduce the following dimensionless variables which replace time, momentum and photon temperature, respectively

$$x \equiv m\, a \qquad y \equiv p\, a \qquad z \equiv T_\gamma\, a \ . \tag{6.9}$$

The parameter m is an arbitrary mass scale which can be put e.g. equal to 1 MeV or to m_e. The function a is normalized so that $a(t) \to 1/T$ at large temperatures, with T the temperature of the particles in equilibrium. Consequently, a^{-1} can be identified with the initial temperature of thermal, active neutrinos.

In terms of these new variables, the equations of motion Eq. (2.5) for the neutrino (and antineutrino) ensemble in the expanding Universe ($\partial_t \to \partial_t - Hp\, \partial_{\mathbf{p}}$) assume the form [151, 60, 66]

$$\begin{aligned} i\frac{d\varrho}{dx} =& + \frac{x^2}{2m^2\, y\, \overline{H}} \left[\mathrm{M}^2, \varrho\right] + \frac{\sqrt{2} G_F\, m^2}{x^2\, \overline{H}} \\ & \times \left[\left(-\frac{8\, y\, m^2}{3\, x^2\, m_W^2} \mathsf{E}_\ell - \frac{8\, y\, m^2}{3\, x^2\, m_Z^2} \mathsf{E}_\nu + \mathsf{N}_\nu \right), \varrho \right] + \frac{x\, \hat{C}[\varrho(y)]}{m\, \overline{H}}, \qquad (6.10) \\ i\frac{d\bar{\varrho}}{dx} =& - \frac{x^2}{2m^2\, y\, \overline{H}} \left[M^2, \bar{\varrho}\right] + \frac{\sqrt{2} G_F\, m^2}{x^2\, \overline{H}} \\ & \times \left[\left(+\frac{8\, y\, m^2}{3\, x^2\, m_W^2} \mathsf{E}_\ell + \frac{8\, y\, m^2}{3\, x^2\, m_Z^2} \mathsf{E}_\nu + \mathsf{N}_\nu \right), \bar{\varrho} \right] + \frac{x\, \hat{C}[\bar{\varrho}(y)]}{m\, \overline{H}}, \qquad (6.11) \\ x\frac{d\varepsilon}{dx} =& \varepsilon - 3\mathcal{P}. \qquad (6.12) \end{aligned}$$

Here $\overline{H}$ denotes the properly normalized Hubble parameter

$$\overline{H} \equiv \frac{x^2}{m} H = \frac{x^2}{m} \sqrt{\frac{8\pi\, \epsilon(x, z(x))}{3\, M_{Pl}^2}} = \left(\frac{m}{M_{Pl}}\right) \sqrt{\frac{8\pi \varepsilon(x, z(x))}{3}} \ , \tag{6.13}$$

[1] The restriction to a 3×3 matrix for the system (2+1) is trivial.

where the total energy density ϵ and pressure of the plasma P are present through their "comoving transformed" $\varepsilon \equiv \epsilon(x/m)^4$ and $\mathcal{P} \equiv P(x/m)^4$ respectively. Since for the temperatures of interest, electrons and positrons are the only charged leptons populating the plasma copiously, we can consider to a very good approximation the total energy density composed by:

$$\varepsilon(x, z(x)) \simeq \varepsilon_\gamma + \varepsilon_e + \varepsilon_\nu \,, \tag{6.14}$$

where

$$\varepsilon_\gamma = \frac{\pi^2}{15} z^4(x), \tag{6.15}$$

$$\varepsilon_e = \frac{1}{\pi^2} \int_0^\infty dy\, y^3 \, [f_{FD}(y/z(x) - \phi_e) + f_{FD}(y/z(x) + \phi_e)] \simeq \frac{7\,\pi^2}{60}\, z^4(x), \tag{6.16}$$

$$\varepsilon_\nu = \frac{1}{2\pi^2} \int dy\, y^3 \mathrm{Tr}[\varrho(x, y) + \bar{\varrho}(x, y)] \equiv \frac{7}{8} \frac{\pi^2}{15} N_{\rm eff} \,. \tag{6.17}$$

In this expressions, we have assumed massless $e^\pm$ in the range of temperature considered and $e^\pm$ have a Fermi-Dirac distribution $f_{FD}(y/z(x) \mp \phi_e) \equiv 1/(\exp(y/z(x) \mp \phi_e) + 1)$ due to the fast electromagnetic interactions. Further, the reduced electron chemical potential ϕ_e is, in general, a dynamical variable that requires an extra equation (the electric charge conservation) in order to be evolved consistently. In some cases, the electrons are only important when their energy density is dominated by pairs, rather than by the e^- excess due to the baryon asymmetry. In this case ϕ_e can be put equal to zero.
Passing to the different terms involved in the evolution equations [Eqs. (6.10), (6.11)], (see also Chapter 2), the first term on the r.h.s. is responsible for the vacuum neutrino oscillations, where in the flavor basis $\mathrm{M}^2 = \mathcal{U}^\dagger \mathcal{M}^2 \mathcal{U}$. The successive term represents the second order contribution refractive term with the background medium (electrons and positrons). The diagonal matrix E_ℓ, related to the energy density of the charged leptons under the previous assumptions, is

$$\mathsf{E}_\ell \equiv \mathrm{diag}(\varepsilon_e, 0, 0, 0) = \mathrm{diag}\left(\frac{7\,\pi^2}{60}\, z^4(x), 0, 0, 0\right) \quad . \tag{6.18}$$

The other two terms in the brackets correspond to the leading and the higher order of the self-interactions, related, respectively, to the *difference* and to

the *sum* of the density matrices of neutrinos and antineutrinos:

$$\mathsf{N}_\nu = \frac{1}{2\pi^2}\int dy\, y^2 \left\{\mathsf{G}_s(\varrho(x,y) - \bar{\varrho}(x,y))\mathsf{G}_s + \mathsf{G}_s \mathrm{Tr}\left[(\varrho(x,y) - \bar{\varrho}(x,y))\mathsf{G}_s\right]\right\} \tag{6.19}$$

$$\mathsf{E}_\nu = \frac{1}{2\pi^2}\int dy\, y^3\, \mathsf{G}_s(\varrho(x,y) + \bar{\varrho}(x,y))\mathsf{G}_s\,, \tag{6.20}$$

where the matrix $\mathsf{G}_s = \mathrm{diag}(1,1,1,0)$ in flavor space contains the dimensionless coupling constants. We remind the reader that these terms make the EoMs non-linear and then represent the main numerical challenge in the study of this physical system. Moreover we remark that, in the presence of more than one active specie, the N_ν matrix also contains off-diagonal terms. The last term at r.h.s. of Eqs. (6.10) and (6.11) is the collisional term proportional to G_F^2. Using the approximate form [179] for the collisional terms, we obtain the expressions

$$\begin{aligned}\hat{C}[\rho(y)] = &-\frac{i}{2}G_F^2\, m^4(\{\mathsf{S}^2, \rho(y) - \rho_{\rm eq}\} - 2\mathsf{S}(\rho(y) - \rho_{\rm eq})\mathsf{S} + \{\mathsf{A}^2, (\rho(y) - \rho_{\rm eq})\} \\ &+ 2\mathsf{A}(\bar{\rho}(y) - \bar{\rho}_{\rm eq})\mathsf{A})\end{aligned} \tag{6.21}$$

$$\begin{aligned}\hat{C}[\bar{\rho}(y)] = &-\frac{i}{2}G_F^2\, m^4(\{\mathsf{S}^2, \bar{\rho}(y) - \bar{\rho}_{\rm eq}\} - 2\mathsf{S}(\bar{\rho}(y) - \bar{\rho}_{\rm eq})\mathsf{S} + \{\mathsf{A}^2, (\bar{\rho}(y) - \bar{\rho}_{\rm eq})\} \\ &+ 2\mathsf{A}(\rho(y) - \rho_{\rm eq})\mathsf{A}).\end{aligned} \tag{6.22}$$

where $\rho_{\rm eq}$ is the equilibrium density matrix written in terms of the FD distributions. Even if these expressions have been derived for null neutrino asymmetry, the correction induced by its presence would be negligible if restricting to a small values for it (as those adopted in the following) (see, e.g., [163]). In flavor space, the matrices S, A write $\mathsf{S} = \mathrm{diag}(g_s^e, g_s^\mu, g_s^\tau, 0)$ and $\mathsf{A} = \mathrm{diag}(g_a^e, g_a^\mu, g_a^\tau, 0)$, respectively, and include the numerical coefficients for the scattering and annihilation processes of the different neutrino flavors. Numerically one finds [153]

$$\begin{aligned}(g_s^e)^2 &= 3.06 \quad , \quad (g_a^e)^2 = 0.50\ , \\ (g_s^{\mu,\tau})^2 &= 2.22 \quad , \quad (g_a^{\mu,\tau})^2 = 0.28\ .\end{aligned} \tag{6.23}$$

We note that this collisional form, even though approximate, guarantees that: i) the correct collisional term is found when integrating the EoMs over momenta, ii) the overall lepton number conservation is preserved. This is not the case for alternative damping prescriptions usually used in literature, where the lepton number conservation is obtained imposing an additional equation (see e.g. [177]). We comment that possible minor inaccuracies in the

$y-$dependence of the collisional terms are of slight significance for our application.

Finally, Eq. (6.12) provides an evolution equation for the quantity $z(x)$. On the other hand, even when a fourth neutrino is populated in the plasma via early oscillations (before the active neutrino decoupling), the correction with respect to the initial value of ε is at most of the order of $\sim 10\%$. We have tracked $z(x)$ by using the integrated entropy ratio formula (see e.g. Eq. (15) in [178], with df_i/dx at the right-hand side put to zero).

Concerning the initial conditions for the density matrix ϱ, they are given by

$$\begin{aligned} \varrho_{\rm in} &= {\rm diag}\left(f_{\rm eq}(y,\xi_e), f_{\rm eq}(y,\xi_\mu), f_{\rm eq}(y,\xi_\tau), 0\right) \ , \\ \bar{\varrho}_{\rm in} &= {\rm diag}\left(f_{\rm eq}(y,-\xi_e), f_{\rm eq}(y,-\xi_\mu), f_{\rm eq}(y,-\xi_\tau), 0\right) \ , \end{aligned} \tag{6.24}$$

with the equilibrium distribution

$$f_{\rm eq}(y,\xi) = 1/[\exp(y-\xi)+1]. \tag{6.25}$$

In absence of primordial neutrino asymmetry, $\xi_\alpha = 0$.

6.3.1 "Average momentum" approximation

In the presence of continuous neutrino momentum distributions, to solve the full set of EoMs (6.10) and (6.11) represents a computationally challenging and time consuming task. In our first study on the subject, in order to perform a more treatable numerical treatment of the flavor evolution, which nevertheless would be able to catch the main features of the complete calculation, we took advantage of a "average-momentum approximation" (called also single-momentum approximation), based on the ansatz (and similarly for antineutrinos)

$$\varrho(x,y) \to f_{FD}(y)\,\rho(x)\,. \tag{6.26}$$

In terms of Eq. (6.26) the set of EoMs (6.10) and (6.11) can be rewritten as

$$\begin{aligned} i\frac{d\rho}{dx} =& + \frac{x^2}{2m^2\,\overline{H}}\left\langle\frac{1}{y}\right\rangle\left[{\rm M}^2,\rho\right] + \frac{\sqrt{2}G_F\,m^2}{x^2\,\overline{H}} \\ & \times\left[\left(-\frac{8\langle y\rangle m^2}{3\,x^2\,m_W^2}\mathsf{E}_\ell - \frac{8\langle y\rangle\,m^2}{3\,x^2\,m_Z^2}\mathsf{E}_\nu + \mathsf{N}_\nu\right),\rho\right] + \frac{\widehat{C}[\rho]}{x^4\,\overline{H}} \end{aligned} \tag{6.27}$$

$$\begin{aligned} i\frac{d\bar{\rho}}{dx} =& - \frac{x^2}{2m^2\,\overline{H}}\left\langle\frac{1}{y}\right\rangle\left[{\rm M}^2,\bar{\rho}\right] + \frac{\sqrt{2}G_F\,m^2}{x^2\,\overline{H}} \\ & \times\left[\left(+\frac{8\langle y\rangle m^2}{3\,x^2\,m_W^2}\mathsf{E}_\ell + \frac{8\langle y\rangle m^2}{3\,x^2\,m_Z^2}\mathsf{E}_\nu + \mathsf{N}_\nu\right),\bar{\rho}\right] + \frac{\widehat{C}[\bar{\rho}]}{x^4\,\overline{H}}\,, \end{aligned} \tag{6.28}$$

where by definition $\langle g(y)\rangle \equiv \int_0^\infty y^2\, g(y)\, f_{FD}(y)\, dy / \int_0^\infty y^2\, f_{FD}(y)\, dy$. According to this notation $\langle y\rangle = 3.15$ and $\langle 1/y\rangle = 0.456 \neq 1/\langle y\rangle$. The non-linear terms N_ν and E_ν of Eqs. (6.19,6.20) assume the form

$$\mathsf{N}_\nu = \frac{3\,\zeta(3)}{4\pi^2}\{\mathsf{G}_s(\rho-\bar\rho)\mathsf{G}_s + \mathsf{G}_s \mathrm{Tr}\,[(\rho-\bar\rho)\mathsf{G}_s]\}\,, \tag{6.29}$$

$$\mathsf{E}_\nu = \frac{7}{8}\frac{\pi^2}{30}\mathsf{G}_s(\rho+\bar\rho)\mathsf{G}_s\,. \tag{6.30}$$

In absence of primordial neutrino asymmetries, the equilibrium initial conditions for the density matrix are $\rho = \mathsf{I}$. Instead, in presence of non vanishing primordial neutrino asymmetry, $L_\nu = (n_\nu - n_{\bar\nu})/n_\gamma$, the initial conditions for the density matrix ρ are written

$$\begin{aligned}\rho_{\rm in} &= \mathrm{diag}\left(1+\frac{4}{3}L_e, 1+\frac{4}{3}L_\mu, 1+\frac{4}{3}L_\tau, 0\right)\,,\\ \bar\rho_{\rm in} &= \mathrm{diag}\left(1-\frac{4}{3}L_e, 1-\frac{4}{3}L_\mu, 1-\frac{4}{3}L_\tau, 0\right)\,,\end{aligned} \tag{6.31}$$

where the neutrino asymmetries in the different neutrino flavors $\alpha = e,\mu,\tau$ are related to dimensionless chemical potentials $\xi_\alpha = \mu_\alpha/T_\nu$ through

$$L_\alpha = \frac{\pi^2}{12\zeta(3)}(\frac{T_\nu}{T_\gamma})^3\left(\xi_\alpha + \frac{{\xi_\alpha}^3}{\pi^2}\right). \tag{6.32}$$

The expression in Eq. (6.31) is only valid at leading order in L.

Neutrino interaction terms and resonances conditions

We estimate the different dimensionless factors multiplying ρ and $\bar\rho$ on the r.h.s. of Eqs. (6.27) and (6.28), respectively. The vacuum oscillation term is proportional, except for a matrix whose coefficients are $\mathcal{O}(1)$, to the quantity

$$\Omega_{\rm vac} \equiv \frac{x^2\,\Delta m^2}{2\,\overline{H}\,m^2}\left\langle\frac{1}{y}\right\rangle = 2.3\times 10^{-13}\left(\frac{\Delta m^2}{\mathrm{eV}^2}\right)\frac{x^2}{\overline{H}}\,, \tag{6.33}$$

Taking into account the e^+e^- pairs only, the matter potential in Eqs. (6.27) and (6.28) apart from the different sign for neutrinos and antineutrinos, is proportional to

$$\Omega_{\rm matt} = \frac{8\sqrt{2}\langle y\rangle G_F\, m^4}{3\,m_W^2}\frac{7\,\pi^2}{60}\left(\frac{1}{x^4\,\overline{H}}\right) = 2.4\times 10^{-20}\,\frac{1}{x^4\,\overline{H}}\,. \tag{6.34}$$

The asymmetric and symmetric terms given by the neutrino-neutrino interactions are proportional to

$$\begin{aligned}\Omega_{\rm asy} =& \frac{\sqrt{2} G_F\, m^2}{x^2\, \overline{H}}\, \frac{3\,\zeta(3)}{4\,\pi^2} = 1.5 \times 10^{-12}\, \frac{1}{x^2\, \overline{H}}\ , \\ \Omega_{\rm sym} =& \frac{8\sqrt{2}\langle y\rangle G_F\, m^4}{3\, m_Z^2} \frac{7\,\pi^2}{240} \left(\frac{1}{x^4\, \overline{H}}\right) = \frac{1}{4} \left(\frac{m_W}{m_Z}\right)^2 \Omega_{\rm matt} = \frac{\cos^2\theta_W}{4}\, \Omega_{\rm matt}\ .\end{aligned} \tag{6.35}$$

Finally, the collisional term is proportional to

$$\Omega_{\rm coll} = \frac{G_F^2\, m^4}{2\, x^4\, \overline{H}} = 6.8 \times 10^{-23}\, \frac{1}{x^4\, \overline{H}}\, . \tag{6.36}$$

The refractives terms can induce MSW-like resonances between the actives ($a = e, \mu, \tau$) and sterile state when they become $\mathcal{O}(\Delta m^2_{\rm st})$, i. e. when one of the following conditions is satisfied [163]:

$$\begin{aligned}\Omega_{\rm vac} \cos 2\theta_{as} - \Omega_{\rm asy}\Delta_a + \Omega_{\rm sym}\Sigma_{aa} + \Omega_{\rm mat} &= 0 \quad \text{for } \nu\ , \\ \Omega_{\rm vac} \cos 2\theta_{as} + \Omega_{\rm asy}\Delta_a + \Omega_{\rm sym}\Sigma_{aa} + \Omega_{\rm mat} &= 0 \quad \text{for } \overline{\nu}\ .\end{aligned} \tag{6.37}$$

The quantities Δ_a and Σ_{aa} are given in terms of the difference and the sum of the density matrix diagonal components, respectively. In particular for the ν_e they reads: $\Delta_e = 2(\rho_{ee} - \bar{\rho}_{ee}) + (\rho_{\mu\mu} - \bar{\rho}_{\mu\mu}) + (\rho_{\tau\tau} - \bar{\rho}_{\tau\tau}) \propto (2L_e + L_\mu + L_\tau)$ and $\Sigma_{ee} = (\rho_{ee} + \bar{\rho}_{ee}) \simeq 2$. These conditions are obtained in the limit of only one mixing angle between the active and the sterile neutrinos, but can be generalized to the multi-flavor case. We remark that the possible resonances depend on the different mass hierarchies in the active and sterile neutrino sector.

6.4 Bounds on sterile mass and mixing parameter space

In this section we present the bound update on the sterile mass and mixing parameter space in (3+1) sterile neutrino scenarios using the value of $N_{\rm eff} = 3.30 \pm 0.27$ at 68 % C.L. measured with a quite a good precision by the Planck satellite experiment [135], as well as the constraint $\Omega_\nu h^2 \lesssim 0.0045$ at 95 % C.L. coming from the neutrino mass bound data of the same experiment. We consider a broad range for active-sterile neutrino mass squared splitting (which covers the regions where laboratory hints emerge) in both normal and inverted mass hierarchies for the active and sterile states. For the first time,

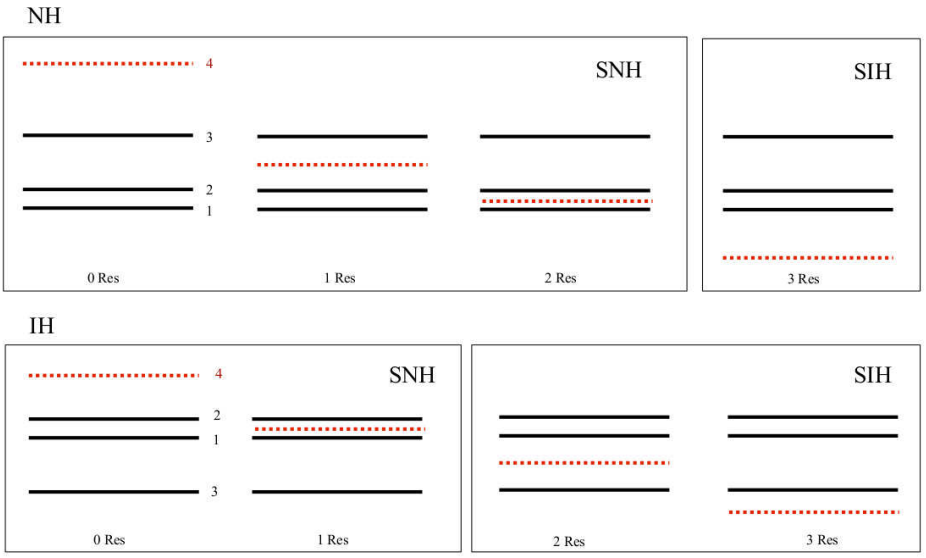

Figure 6.1: Schematic representation of the possible resonances occurring for different combinations of active (continuous curve) and sterile (dashed) hierarchies.

we have taken into account the possibility of two non-vanishing active-sterile mixing angles.

Depending on the sign of Δm^2_{31} and $\Delta m^2_{41} = \Delta m^2_{\rm st}$, we define the following cases:

- active normal mass hierarchy (NH, $\Delta m^2_{31} > 0$)

- active inverted mass hierarchy (IH, $\Delta m^2_{31} < 0$)

- sterile normal mass hierarchy (SNH, $\Delta m^2_{41} > 0$)

- sterile inverted mass hierarchy (SIH, $\Delta m^2_{41} < 0$).

In our study we consider the following mass splitting ranges:

$$10^{-5} \leq \Delta m^2_{41}/\mathrm{eV}^2 \leq 10^2 \text{ (in SNH)} , \quad 10^{-5} \leq |\Delta m^2_{41}|/\mathrm{eV}^2 \leq 10^{-2} \text{ (in SIH)}.$$

Concerning the SIH case, larger values of $|\Delta m^2_{41}|$ are disfavored due to the cosmological bounds on the neutrino masses [128, 135]. For the mixing angles between active and sterile neutrinos we choose as representative range $10^{-5} \leq \sin^2\theta_{i4} \leq 10^{-1}$ (i=1,2,3).

Since we want to perform an extensive scan of the sterile neutrino parameter space, we follow the evolution of the [Eqs. (6.27)-(6.28)] in the averaged-momentum approximation Eq. (6.26), in order to make more treatable the numerical analysis. Moreover we consider the most conservative scenario, with zero neutrino asymmetries, as small as the baryon asymmetry.

As discussed before, the matter terms in the Eqs. (6.27)-(6.28), can induce MSW-like resonances. The possible resonances depend on the different mass hierarchies in the active and sterile neutrino sector, as schematically described in the Fig. 6.1. In particular, in the absence of neutrino asymmetries, the resonance condition Eq. (6.37) can be satisfied (in both neutrino and antineutrino sectors) only for $\Delta m^2_{4i} < 0$. When more than one Δm^2_{4i} is negative, multiple resonances can occur, influenced the sterile neutrino production. In the presence of non-zero θ_{13} the resonance conditions become more complicated, since more than one active neutrino species can resonate with the sterile state, even in the presence of a single active-sterile mixing angle. An example of a possible resonance pattern is shown in Fig. 6.2, where we plot the sterile neutrino density matrix element ρ_{ss} for $\sin^2\theta_{14} = 10^{-2}$ versus temperature T, for different values of the Δm^2_{41} mass splitting. For $\Delta m^2_{41} = +10^{-5}$ eV^2 (continuous curve), since both Δm^2_{43} and Δm^2_{42} are negative, we find two resonances. The first at $T \simeq 6.5$ MeV between ν_4 and $\nu_{2,3}$ associated with Δm^2_{43}, and a second one at $T \simeq 3.5$ MeV between ν_4 and $\nu_{1,2,3}$ associated with Δm^2_{42}. For $\Delta m^2_{41} = -10^{-5}$ eV^2 (dashed curve) we also have a further resonance at $T \simeq 2.5$ MeV between ν_4 and $\nu_{1,2,3}$. Finally, for $\Delta m^2_{41} = 5 \times 10^{-2}$ eV^2 (dotted curve), since all the mass splitting between active and sterile neutrinos are positive, this case is associated with no resonances. The presence of possible multiple resonances implies that the sterile neutrino production would be strongly dependent on the active and sterile mass hierarchies. When $\Omega_{\rm asy}\Delta_{ii}$ is the dominant term, if $\Delta m^2_{4i} > 0$ resonances can occur for $\Delta_{ii} > 0$ in the ν sector and for $\Delta_{ii} < 0$ in the $\overline{\nu}$ one, and viceversa if $\Delta m^2_{4i} < 0$.

Results The quantity we are exploiting to constrain the sterile neutrino parameter space is the overall non electromagnetic radiation content, parametrized via $N_{\rm eff}$,

$$N_{\rm eff} = \frac{1}{2}{\rm Tr}(\rho + \bar{\rho}) \ . \tag{6.38}$$

Our bounds are given comparing this number with the one measured by Planck experiment, $N_{\rm eff} < 3.80$ at 95 % C.L. [135]. We mention that at 3 σ, $N_{\rm eff} > 4$ and then no useful constraint can be put. Moreover, also combining the Planck data with the measurement of the Hubble parameter H_0 given by the Hubble Space Telescope experiment, one would allow for one sterile

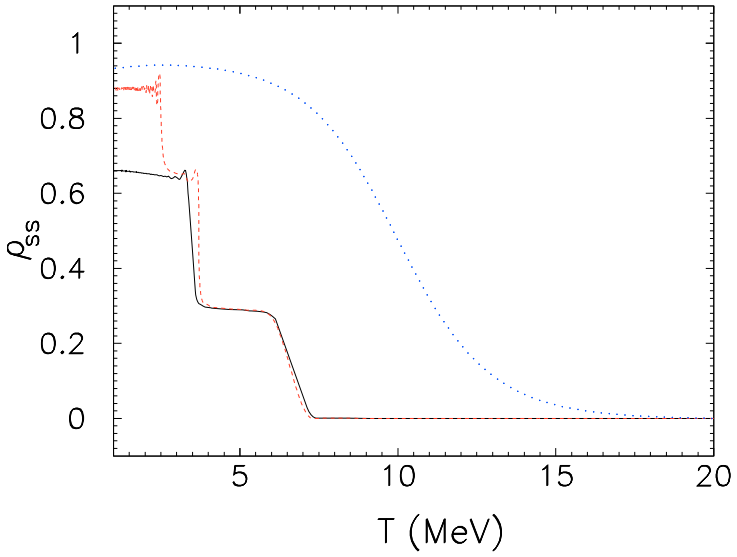

Figure 6.2: Evolution of the density matrix element ρ_{ss} in function of the temperature for different value of Δm^2_{41} mass splitting: $+10^{-5}$ eV^2 (continuous curve), -10^{-5} eV^2 (dashed curve), 5×10^{-2} eV^2 (dotted curve).

neutrino [135]. Given the current limit on the sum of the neutrino masses we remark that the constraints on $N_{\rm eff}$ can set upper bounds on the sterile neutrino mixing parameters for sterile mass $m_4 < 0.5$ eV considering a fully thermalised extra neutrino species [135]. Larger values of the sterile neutrino mass would be not relativistic anymore at the CMB decoupling and therefore they could not be constrained exploiting the measurement of $N_{\rm eff}$ by Planck. In order to probe them, one should include sterile neutrinos in the codes computing the CMB observables. However, one can get a qualitative bound evaluating the neutrino contribution to the energy density in the Universe. Assuming the existence of a thermalized massive sterile neutrino together with two massless active neutrinos and a massive one with mass fixed by the atmospheric mass-splitting(i.e. m 0.06 eV), we have

$$\Omega_\nu h^2 = \frac{1}{2}\frac{\sqrt{\Delta m^2_{41}}\cdot(\rho_{ss}+\overline{\rho}_{ss})}{94.1\ \text{eV}} \quad . \tag{6.39}$$

The Planck+BAO constraint on the neutrino energy density is $\Omega_\nu h^2 \lesssim 0.0045$ at 95 % C.L, coming from the Planck bound on the effective sterile mass $m_s^{\rm eff} \leq 0.42$ eV. We note that the calculation of $\Omega_\nu h^2$ assumes the sterile mass contribution as the dominate one being much larger than the active neutrino ones, in agreement with the Planck analysis. Therefore, this bound

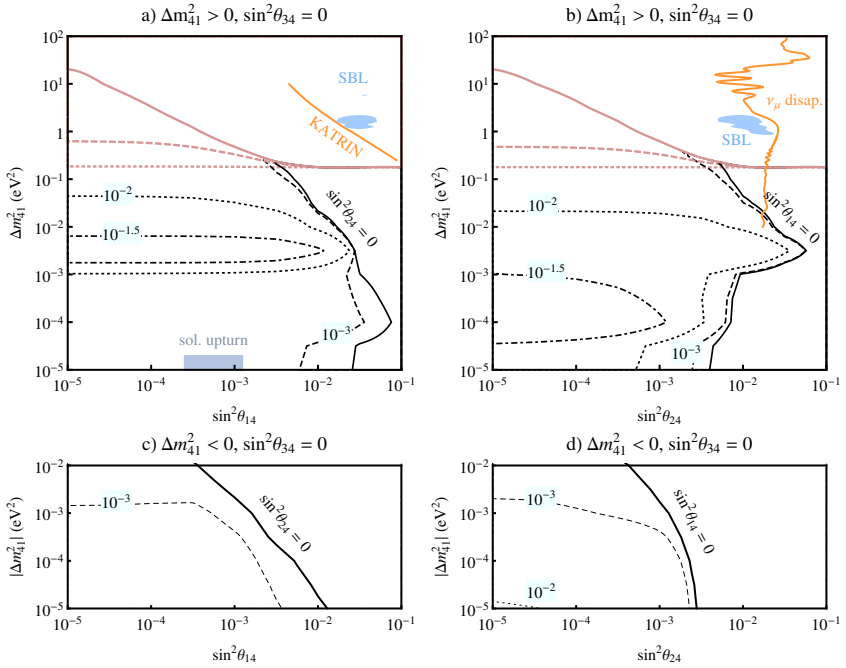

Figure 6.3: Exclusion plots for the active-sterile neutrino mixing parameter space for different scenarios (see the text for details).

is insensitive to the active mass hierarchy.

In Fig. 6.3 we present our exclusion plots at 95 % C.L. in the planes $(\Delta m^2_{41}, \sin^2\theta_{i4})$. For simplicity, we show our findings only for NH, while we consider both SNH and SIH. Moreover, since the results as a function of $\sin^2\theta_{34}$ and $\sin^2\theta_{24}$ are very similar, we omit to present the $\sin^2\theta_{34}$ case.

In the upper panels a), b) we consider SNH, while in the lower panels c), d) we show the SIH case. Left panels correspond to the exclusion plots in the plane $(\Delta m^2_{41}, \sin^2\theta_{14})$ for different values of $\sin^2\theta_{24}$, while right panels refer to the plane $(\Delta m^2_{41}, \sin^2\theta_{24})$ for different values of $\sin^2\theta_{14}$. In all the cases, $\sin^2\theta_{34}$ is fixed to zero. The excluded regions from the extra-radiation $N_{\rm eff}$ are those on the right or at the exterior of the (closed) contours (black curves). The obtained constrains from the energy density $\Omega_\nu h^2$ are represented by the red curves. We now discuss the different panels in more details.

- *Panel a)* The most conservative bound corresponds to $\sin^2\theta_{24} = 0$, where for $\Delta m^2_{41} \gtrsim 10^{-2}$ eV^2 the radiation exclusion contour is given by a straight line in this plane. The cut in the contour at ($\Delta m^2_{41} \sim 10^{-1}$ eV^2 , is due to the fact that the neutrinos with higher masses are not relativistic anymore at the CMB epoch and so we cannot use

radiation constraints. However, mass bounds from $\Omega_\nu h^2$ give important information.

Concerning the radiation constraints, lowering the value of Δm^2_{41} one triggers first a $\nu_4 - \nu_3$ resonance (when $\Delta m^2_{41} < \Delta m^2_{31}$) and then also a $\nu_4 - \nu_2$ resonance (when $\Delta m^2_{41} < \Delta m^2_{21}$) which is the dominant one. These cause the changes of the slope in the exclusion contour. In particular, increasing the value of $\sin^2\theta_{24}$, the constraint on the parameter space becomes more severe. Large values of $\sin^2\theta_{24}$ would rule the sterile neutrino production and excluding regions otherwise permitted for only the mixing angle $\sin^2\theta_{14}$ different from zero. The only part allowed is then the transition region between the efficient non-resonant production range at large Δm^2_{41} and the one of resonant production at small Δm^2_{41}. Concerning the bounds from $\Omega_\nu h^2$, the most conservative limit is for $\sin^2\theta_{24} = 0$ for which values of $\Delta m^2_{41} \gtrsim 10^{-1}$ eV^2 are excluded for $\sin^2\theta_{14} \gtrsim 10^{-2}$, since the sterile neutrinos are fully thermalized. For smaller values of $\sin^2\theta_{14} \gtrsim 10^{-2}$ the constraint becomes less stringent, due to the incomplete thermalization of the sterile species, allowing e.g. $\Delta m^2_{41} \lesssim 1$ eV^2 for $\sin^2\theta_{14} \lesssim 10^{-4}$. The bound becomes more severe increasing the value of $\sin^2\theta_{24}$. In particular, for $\sin^2\theta_{24} \gtrsim 10^{-2}$, $\Delta m^2_{41} \gtrsim 10^{-1}$ eV^2 is excluded independently on the value of $\sin^2\theta_{14}$, since sterile neutrinos would be always thermally produced. For comparison, we also show the slice at $\sin^2\theta_{24} = 10^{-2}$ of the 95 % C.L., allowed region obtained from the global analysis of short-baseline oscillation data [144, 180] (filled blue region in the up right part of the plot indicated by SBL). We see that it seems to be completely ruled out by the cosmological bound. We also show in orange the 90 % C.L. expected sensitivity of the KATRIN experiment (measuring the spectrum of electrons from tritium beta decay) after 3-years of data taking [181]. We see that, in absence of any additional ingredient, such us a significant primordial neutrino asymmetry [179, 173], also this region is excluded by cosmology, in particular for $\sin^2\theta_{24} > 10^{-3}$. Finally, we represent with a grey square in the lower part of the plot, the region of parameters corresponding to a light sterile neutrino with $\Delta m^2_{41} \simeq 10^{-5}$ eV^2 and $\sin^2\theta_{14} \sim 10^{-4} - 10^{-3}$, suggested to solve the problem of the upturn of the solar neutrino spectrum [182].

- *Panel b)* The description of the exclusion plot is analogous to the one of panel a), with the roles of θ_{14} and θ_{24} interchanged. In particular, the region of resonant sterile neutrino production is at $\Delta m^2_{41} \simeq 10^{-3}$ eV^2 when a $\nu_4 - \nu_3$ resonance is efficient. We have also drawn the slice at $\sin^2\theta_{14} = 10^{-1.5}$ of the 95 % C.L. allowed region from the global

analysis of short-baseline oscillation data [144, 180], which is another view of the SBL region shown in panel a), and, moreover, the exclusion curve obtained from the combined analysis of the data of ν_μ and $\bar{\nu}_\mu$ disappearance experiments. We can see that also in this case the region is excluded by the cosmological limit.

- *Panels c) and d)* Since $\Delta m^2_{41} < 0$ also a ν_4-ν_1 resonance is present leading to an increase in the production of sterile neutrinos, with respect to the case of SNH. Therefore, the excluded regions are larger than the corresponding ones in the upper panels. We note that only $|\Delta m^2_{41}| < 10^{-2}$ eV^2 is considered, due to the cosmological bound on active neutrino masses.

Summarizing, using as benchmark the joint constraints on $N_{\rm eff}$ and $\sum m_\nu$ (translated in a constraint for $\Omega_\nu h^2$), as measured by the Planck experiment, we find that the sterile neutrino mass and mixing parameter space is severely constrained, and the excluded area covers the region accessible by current and future laboratory experiments. Therefore we confirm that there is a tension with the sterile neutrino hints from short-baseline experiments.

6.5 Role of the neutrino asymmetry in the sterile neutrino production

From previous studies and also from our analysis on the sterile parameter space one infers that, for the mass and mixing parameters needed to describe the short-baseline anomalies, sterile neutrinos would be completely thermalized in the Early Universe, creating tension with cosmological observations on $N_{\rm eff}$ and on the neutrino mass bound. Therefore, non standard scenarios have to be invoked to alleviate this tension. A possible escape-route to reconcile sterile neutrinos with cosmological data is represented by the inclusion of a primordial asymmetry between neutrinos and antineutrinos [161]

$$L = \frac{n_\nu - n_{\bar{\nu}}}{n_\gamma} \,. \tag{6.40}$$

Considering the very small value of the baryonic asymmetry, $\eta = (n_B - n_{\bar{B}})/n_\gamma \simeq 6 \times 10^{-10}$, it is reasonable to expect the same order of magnitude for the charged lepton asymmetry, in order to respect the charge neutrality. In the neutrino case, being neutral particles, the constrains on L are quite loose, allowing also $|L| \simeq 10^{-2} - 10^{-1}$ [66, 183, 184, 185, 186, 122, 187]. Moreover, there are models for producing large L and small η [188, 189, 190].

An initial neutrino asymmetry implies an additional "matter term potential" in the equations of motion [Eq. (6.10)-(6.10)]. If sufficiently large, it can block the active-sterile flavor conversions via the in-medium suppression of the mixing angle. However, this term can also generate MSW-like resonant flavor conversions among active and sterile neutrinos, *enhancing* the sterile neutrino production. In order to assess which of the two effects dominates the flavor evolution it is mandatory to perform a study of the kinetic equations for active-sterile neutrino oscillations. This problem has been treated in a long series of paper [156, 159, 160, 161, 162, 163, 166, 167, 168, 169, 166, 173]. Among the recent ones, it is worthwhile to mention [179], where the authors solved the equations of motion in a simplified (3+1) single-momentum scheme, inspired by LSND, to look for the minimal value of L necessary to have a significant reduction of the sterile neutrino abundance. They found that $L \sim 10^{-4}$ was enough to suppress the sterile production, relieving the tension between sterile neutrinos and cosmology. However, this result has to be taken with caution, since the authors adopted some severe approximations. In particular, they fixed the neutrio asymmetry as an initial condition taken constant during the flavor evolution. However this quantity is expected to dynamically evolve due to the flavor conversions. Moreover, they solved the coupled equations of motion only for the neutrino system, missing in this case possible resonant transitions between sterile and active neutrino that could occur in the antineutrino sector for the negative value of neutrino asymmetries they used. Finally, they considered only a single active-sterile mixing angle. In a more recent (1+1) multi-momentum study [173] it has been found that for sterile neutrinos with parameters preferred by the laboratory hints, a neutrino asymmetry $L = 10^{-2}$ would strongly suppress their production. However, once again, this scenario is too simplified to detect features proper to multi-flavor system, such as equal or opposite asymmetries between the active species.

We devoted our work to a detailed study of the flavor evolution for (3+1) and (2+1) scenarios inspired by the laboratory anomalies, in presence of primordial neutrino asymmetry, going beyond most of approximations used in previous studies. The results are presented in the next section.

6.5.1 Sterile neutrino production: our explorative study

Here we present the results of the sterile neutrino production for different scenarios and cases. First we analyse the (3+1) scenario for different values of the primordial neutrino asymmetries, taken equal among the different active flavors. Then, we calculate the sterile neutrino abundance in a (2+1) scenario, considering both cases with equal and opposite initial neutrino asymmetries

among the active species, as well as the effects of CP violation in the sterile sector. We remark that in all the cases, we take into account both the active-sterile mixing angles θ_{es} and $\theta_{\mu s}$,[2] from the fits of the short-baseline data [55]

$$\begin{aligned} \sin\theta_{es} &\simeq |\mathcal{U}_{e4}| = \sqrt{0.025} \ , \\ \sin\theta_{\mu s} &\simeq |\mathcal{U}_{\mu 4}| = \sqrt{0.023} \ . \end{aligned} \tag{6.41}$$

The sterile-active mass splitting from the short-baseline fit in the 3+1 model is given by [55]

$$\Delta m^2_{\rm st}/{\rm eV}^2 = 0.89 \ . \tag{6.42}$$

Therefore, it results in a clear hierarchy among the mass differences, i.e. $\Delta m^2_{\rm st} \gg \Delta m^2_{\rm atm} \gg \Delta m^2_{\rm sol}$.

Given the number of the examined cases and the numerical challenging of the problem, we make use of the average-momentum approximation [Eq. (6.26)]. In order to get an idea of the strength of the interaction terms involved in the evolution equations [Eqs. (6.27)-(6.28)], it is useful to confront them in function of the temperature T. Referring to the Sec. 6.3.1, in Fig. (6.4) we plot as a function of the temperature T, $\Omega_{\rm vac}$ (solid curve), $\Omega_{\rm matt}$ (long-dotted curve), $\Omega_{\rm asy} \times \Delta_e$ (dashed curve), $\Omega_{\rm sym} \times \Sigma_{ee}$ (short-dotted curve), $\Omega_{\rm coll} \times [(g^e_s)^2 + (g^\mu_s)^2]$ (dash-dotted curve). Here we use as mass square difference $\Delta m^2_{\rm st}$, $\Delta_e = 2(\rho_{ee} - \bar\rho_{ee}) + (\rho_{\mu\mu} - \bar\rho_{\mu\mu}) + (\rho_{\tau\tau} - \bar\rho_{\tau\tau}) = 8/3(2L_e + L_\mu + L_\tau)$, where for illustration we fixed $L_e = L_\mu = L_\tau = 10^{-4}$. Finally $\Sigma_{ee} = (\rho_{ee} + \bar\rho_{ee}) \simeq 2$.

As expected, the system remains in collisional regime down to a few MeV. Moreover it dominates over the vacuum oscillation term at $T \gtrsim 20$ MeV, thus breaking the coherence of the neutrino enable and preventing significant oscillations. From the resonances condition [Eq. (6.37)], in the hypothesis of sterile normal mass hierarchy we are considered (SNH, $m_4 > m_1$), we obtain that in absence of lepton asymmetries ($\Delta_a = 0$) the resonance condition cannot be satisfied neither for the ν's nor for $\overline{\nu}$'s. Instead, when $\Omega_{\rm asy}\Delta_a$ is the dominant term, as our case, resonance conditions can occur for $\Delta_a > 0$ in the ν sector and for $\Delta_a < 0$ in the $\overline{\nu}$ one. In particular, in Fig. 6.4 it was considered an initial neutrino asymmetry of $L = 10^{-4}$ and the resonance occurs around $T \simeq 3$ MeV. We also note that, due to the dynamical nature of the asymmetries, Δ_a can rapidly change sign so that *both* sterile neutrinos and antineutrinos get populated. Resonances can also take place in the active sector at lower temperatures. However, their effect can be considered subleading, since active neutrino distributions are expected not to depart too much from their equilibrium values.

[2]The angle $\theta_{\tau s}$ is unconstrained by laboratory experiments. For definitess, we will take it zero in the following.

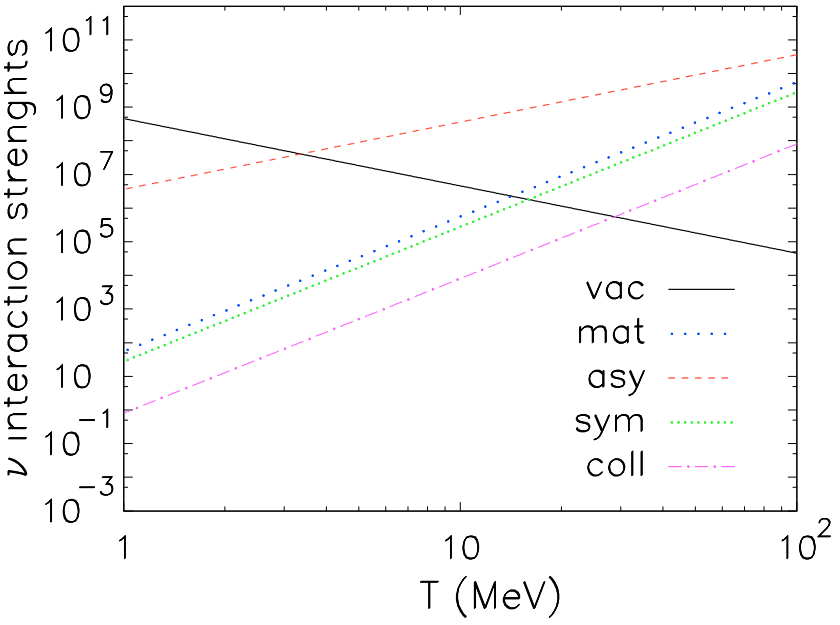

Figure 6.4: Different interaction rates (normalized in terms of the Hubble rate) in function of temperature T. In particular are shown: $\Omega_{\rm vac}$ (solid curve), $\Omega_{\rm matt}$ (long-dotted curve), $\Omega_{\rm asy} \times \Delta_e$ (dashed curve), $\Omega_{\rm sym} \times \Sigma_{ee}$ (short-dotted curve), $\Omega_{\rm coll} \times [(g_s^e)^2 + (g_s^\mu)^2]$ (dash-dotted curve). Here we use $\Delta m^2_{\rm st}$, $\Delta_e = 32L/3$ with $L = 10^{-4}$ and $\Sigma_{ee} = 2$ (see the text for more details).

3+1 results In order to calculate the sterile neutrino abundance in the 3+1 scenario, we numerically solved the EoMs [Eq. (6.28)], using a Runge-Kutta method for the equations written in the variable $x = m/T$ and evolved in the range $x \in [10^{-2}, 1.0]$. We take 10^5 steps in $\log(x)$ in the integration interval. We consider equal and negative neutrino asymmetries, $L = L_e = L_\mu = L_\tau < 0$, but the results presented in the following do not change considering positive asymmetries. In the left panel of the Fig. 6.5 we show the evolution of the sterile component of the density matrix ρ_{ss} (i.e. the flavor content of the sterile state) in function of the temperature T for different initial neutrino asymmetries, namely $L = 0$ (solid curve), $L = -10^{-4}$ (dashed curve), $L = -10^{-3}$ (dotted curve), and $L = -10^{-2}$ (dash-dotted curve). We realise that in absence of lepton asymmetries sterile neutrinos are copiously produced at $T \lesssim 30$ MeV until they reach $\rho_{ss} = 1$, confirming the results presented in the literature. Instead, including a non-zero initial neutrino asymmetry, the sterile neutrino production is suppressed as long as $|\Omega_{\rm asy}| \gg |\Omega_{\rm vac}|$. However, these two functions at some time they will cross, due to their opposite dependence on the temperature, and they will

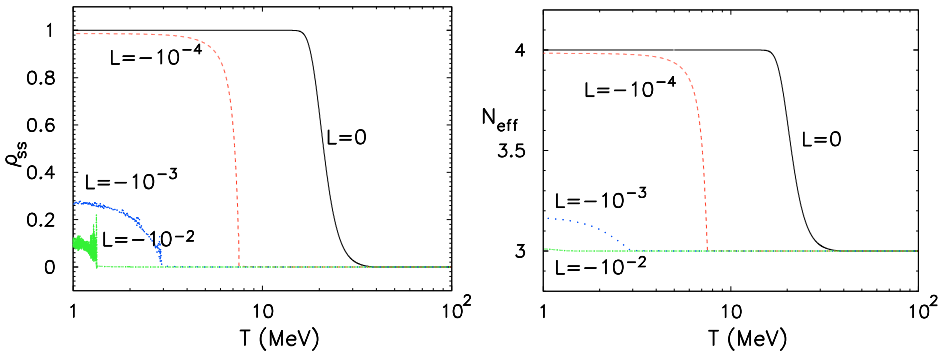

Figure 6.5: (3+1) scenario. Left panel: Evolution of the density matrix element ρ_{ss} in function of the temperature T for different values of initial neutrino asymmetry L. Right panel: Evolution of the effective number of degrees of freedom $N_{\rm eff}$ for the same L values.

producing a resonance. Sterile neutrinos are then produced profusely, albeit with a non-linear, dynamical resonance condition which is itself influenced by the evolution of the system. Increasing the value of L, the position of the resonance shifts towards lower temperatures, where the resonance is less adiabatic and so the sterile production less efficient. Indeed, the adiabaticity parameter scales as $\sim T$, as shown in [191]. In particular, asymmetries greater than $|L| = 10^{-3}$ are required in order to significantly suppress the sterile neutrino production. Moreover, the asymmetric term changes sign and thus the resonance occur in both neutrino and antineutrino sectors, which turn out to be populated almost equally.

From this result we can infer that a neutrino asymmetry of $L = -10^{-3}$ is needed in order to suppress the sterile neutrino production. This value is greater at least by an order of magnitude with respect to what found in a previous study on the subject [179]. The discrepancy is due to the fact that keeping constant the neutrino asymmetry, they missed resonant effects that would have occurred in the antineutrino sector.

In the right panel of the Fig. 6.5, we show the impact of the sterile neutrino production on the increase of the neutrino degrees of freedom in the Early Universe, parameterized via $N_{\rm eff}$. Note that for vanishing or small asymmetry and for the parameters chosen, the active-sterile flavor conversions occur early enough that the depleted active states are rapidly repopulated by collisions. Consequently, $N_{\rm eff}$ reaches the value 4. On the other hand, for $|L| = 10^{-3}$ the conversion starts around the decoupling time, and the repopulation of the active neutrinos is only partial, with a difference between $N_{\rm eff}$ and ρ_{ss} of about 0.1 units. Finally, for $|L| = 10^{-2}$, $N_{\rm eff} = 3$ even if about 10%

of a "thermal-equivalent" sterile state has been produced. This is due to the fact that the flavor conversions occur after the decoupling and only a negligible fraction of the converted active neutrinos are repopulated. Since the temperature at which the sterile production starts depends on when the resonance takes place, there is a strong relation from the exact values of the active neutrino mass, mixing, and the initial value of $|L|$.

2+1 results We present the results of the flavor conversions in the same cases as before, considering a (2+1) sub-sectors with the active mixing associated with $(\Delta m^2_{\rm atm}, \theta_{13})$ as described in the Sec. 6.2. Finding results very similar to the ones presented before, we decide, in order to make more treatable the numerical calculations, to explore the sterile neutrino production in the four different cases of the Fig. 6.6, referring to $(2+1)$ scenarios. In all plots, the solid curve corresponds to $L = 0$, the dashed curve to $L = -10^{-4}$, the dotted curve to $L = -10^{-3}$ and the dash-dotted one to $L = -10^{-2}$.

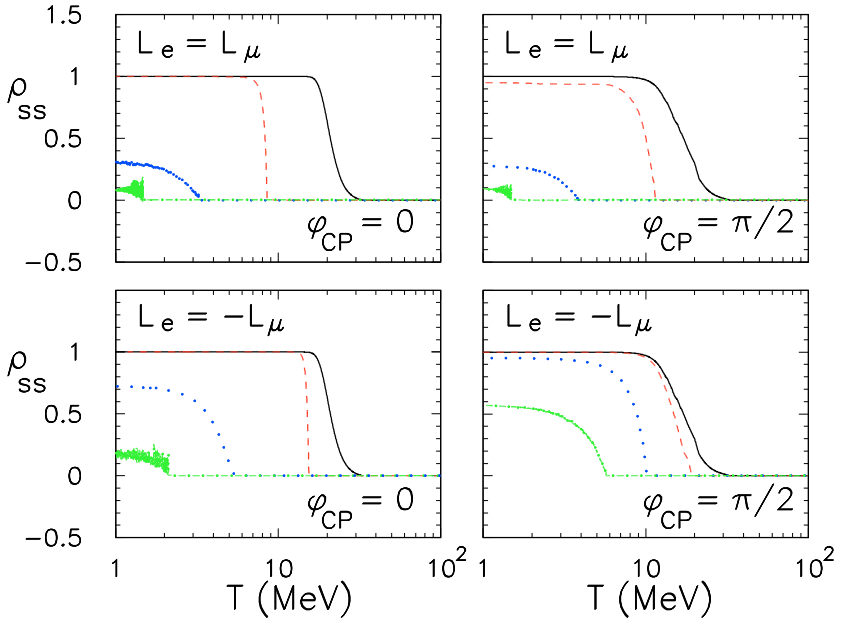

Figure 6.6: (2+1) scenario. Evolution of the sterile component ρ_{ss} in function of the temperature T for different values and combinations of initial neutrino asymmetries. In particular, upper panels correspond to $L = L_e = L_\mu$, lower panels correspond to $L = L_e = -L_\mu$. The solid curves represent $L = 0$, the dashed curves $L = -10^{-4}$, the dotted $L = -10^{-3}$ and the dash-dotted $L = -10^{-2}$. Moreover, left panels show cases with no CP violation in the sterile neutrino sector, while right panels refers to $\varphi_{\rm CP} = \pi/2$.

1. *upper-left panel*: $L_e = L_\mu$, $\varphi_{CP} = 0$

   This case is very close to the (3+1) scenario shown in Fig. 6.5. For $L = 0$, at $T \lesssim 30$ MeV, when collisional rates became week enough (see Fig. 6.4), sterile neutrinos are produced copiously. Considering non-zero initial neutrino asymmetries, since θ_{es} and $\theta_{\mu s}$ are non-vanishing, both the active states can have resonances with the sterile one. In the case with initial $L = -10^{-4}$ the production of ν_s starts at $T \simeq 10$ MeV when an active-sterile resonance occurs. In the other two cases, $L = -10^{-3}$ and $L = -10^{-2}$, the position of the resonance coincides with the onset of the ρ_{ss} rise. However, the lower the resonance temperature, the less adiabatic the resonance and therefore, the sterile neutrino production is further inhibited.

2. *upper-right panel*: $L_e = L_\mu$, $\varphi_{CP} = \pi/2$

   CP violation effects have been include in the sterile sector fits for laboratory anomalies, to accommodate some controversial data (see e.g. [192]). Moreover, whenever three or more neutrinos mix, CP-violating "Dirac phases" entering oscillations are present in the theory. For both reasons, it proved useful to investigate the impact of CP-violation in our framework, including an extra phase in the sterile-active mixing matrix [Eq. (6.3). This inclusion could generate an asymmetry among sterile neutrinos and antineutrinos, which could be transferred by oscillations into the active sector, with a feedback on the further growth of sterile neutrinos. For definiteness we consider $\varphi_{CP} = \pi/2$. From the comparison with the CP conserving case (left-top panel) one infers that the suppression of the sterile neutrino abundance due to φ_{CP} is sub-leading.

3. *lower-left panel*: $L_e = -L_\mu$, $\varphi_{CP} = 0$

   Here we discuss the case in which the initial neutrino asymmetries in the active sector are opposite for ν_e and ν_μ, i.e. $L = L_e = -L_\mu$. For a non-vanishing initial L, the sterile neutrino production is enhanced with respect to the previous case and an asymmetry of $|L| \sim 10^{-3}$ is not enough anymore to achieve a significant suppression of the sterile species. Indeed one needs an initial $|L| \sim 10^{-2}$. We note that since the initial asymmetries have opposite signs, resonances can occur simultaneously in the neutrino and antineutrino channels. When these occur,

they tend to produce flavor equilibrium between ν_e and ν_μ, leading to a vanishing final lepton number. When the total neutrino asymmetry is destroyed, sterile neutrinos can be produced without any obstacle leading to the increase in the final ρ_{ss} found in this case.

4. *lower-right panel*: $L_e = -L_\mu$, $\varphi_{CP} = \pi/2$

   The sterile production is further enhanced when we consider both the case of opposite initial neutrino asymmetries and $\varphi_{\rm CP} = \pi/2$. In particular, also for an initial $L = -10^{-2}$, the final abundance of sterile neutrinos is significant. This is due to the fact that CP violating effects tend to produce an asymmetry in the sterile sector. As a consequence, the active system would be pushed earlier to equilibrium in order to conserve the total null neutrino asymmetry, leading to a more efficiently production.

Summarizing, we have analysed the evolution of the active-sterile system in presence of neutrino asymmetry, for (3+1) and (2+1) scenarios. A primordial neutrino asymmetry, originally introduced to suppress the sterile production, can also generate resonant conversions whose effects depend on the temperature that they occur. Starting from equal asymmetries between the different flavors, we find that an asymmetry of $|L| \sim 10^{-3}$ is required to achieve e notable suppression of the sterile production. This is not guaranteed anymore, if we consider opposite asymmetry signs between the active neutrinos and the situation get worse if we include also a CP violating phase in the sterile sector, requiring an initial asymmetry of $|L| \sim 10^{-2}$. However this value shifts the position of the resonance near or after the neutrino decoupling where the active neutrinos cannot be repopulated by collisions, leading to possible effect on the BBN observables. In particular, as we will see in a while, the absence of repopulation of electron neutrinos would produce distorted neutrino distributions, which can anticipate the n/p freeze-out and hence increase the ^{4}He yield. To asses this point, we have to relax the average momentum approximation used in this exploratory study. Due to the momentum-dependence of the resonant conversions between active and sterile neutrinos, a detailed treatment solving the full momentum-dependent equations is mandatory to derive quantitative phenomenological predictions.

6.5.2 Multi-momentum and multi-flavor active-sterile neutrino oscillations

We present a full multi-flavor and multi-momentum treatment of the active-sterile neutrino oscillations for the (2+1) scenario described before,

with parameters suggested by the short-baseline neutrino anomalies. In particular, we have considered large neutrino asymmetries ($|L_\nu| \gtrsim 10^{-3} - 10^{-2}$) to suppress the sterile production in the Early Universe in order to get a better agreement with the cosmological observations. However, as discussed before, for these large values, the resonant active-sterile flavor conversions occur at lower temperature where the repopulation of the active neutrinos by collision is less efficient, leading to significant distortion in the active spectra. The larger the asymmetry, the more relevant the impact of the distortions on the primordial nucleosynthesis.

In order to characterize these effects, we numerically solved the momentum-dependent EoMs [Eqs. (6.10)-(6.11)] using an integration routine for stiff ordinary differential equations taken from the NAG libraries [193] and based on an adaptive method. The range for x is chosen to be $x \in [2 \times 10^{-2}, 0.5]$. In order to obtain a good compromise between energy resolution of the spectral distortions and computational cost, we took $N_y = 21$ momentum modes in the range $y \in [0, 10]$. The grid points are not chosen to be equally spaced, but are instead fixed by imposing weighted Gaussian quadrature of the integrals in the right-hand-side of Eqs. (6.19)–(6.20).

Concerning the initial conditions for the flavor evolution, we remind the reader that in the presence of primordial neutrino asymmetries, the original active neutrino spectra are given by Fermi-Dirac distributions Eq. (6.25) parametrized in terms of a temperature T_ν and chemical potentials μ_α for $\alpha = e, \mu, \tau$, connected to neutrino asymmetry through the [Eq. (6.40)]. In order to conform with the notation usually used in literature, in the following we shall indicate the neutrino asymmetries in terms of the ξ_α parameters rather than L_α.

Due to the momentum dependence of the resonance conditions, the evolution in in the multi-momentum treatment of the EoMs could show significant deviations with respect to average momentum case. At this regard, in Fig. 6.7 we plot the comparison between the sterile production obtained in the single-momentum and in the multi-momentum cases. In detail, we show the momentum-integrated sterile neutrino density matrix element (solid black curves) normalized to the integral of a Fermi-Dirac distribution with zero chemical potential,

$$\rho_{ss}(x) = \frac{\int dy \;\; y^2 \varrho_{ss}(x, y)}{\int dy \;\; y^2 f_{\rm eq}(y, 0)} \;\; , \tag{6.43}$$

and the sterile neutrino density matrix element ρ_{ss} in the average momentum treatment (dot-dashed red curves), normalized correspondingly. In the left panels we consider the case of equal initial neutrino asymmetries, $\xi_e = \xi_\mu$, while in the right panels we take the opposite ones, $\xi_e = -\xi_\mu$. In the upper

panels we refer to $\xi_e = 10^{-3}$, while in the lower panels we have $\xi_e = 10^{-2}$. We find that in all the cases the values of ρ_{ss} for the single momentum approximation underestimates the sterile neutrino abundance with respect to the multi-momentum treatment. In particular, the enhancement obtained is significant, $\sim 20\%$ of a degree of freedom.

Moreover, from the Fig. 6.7 we infer that the sterile neutrino production in the multi-momentum case occurs at higher temperatures with respect to the average momentum one. Indeed, in the multi-momentum evolution the sterile neutrino population receives contribution also from lower momenta modes, that resonate earlier than the average momentum $\langle y \rangle = 3.15$. This anticipates the dynamical evolution of ξ producing the difference observed. Furthermore, at higher temperature the resonance is more adiabatic and leads to a more efficiently production. Hence, the average momentum treatment of the EoMs is expected to *underestimate* the sterile neutrino abundance.

Finally we comment that the dynamical evolution of the asymmetries is such that *both* neutrinos and antineutrinos get populated resonantly with similar abundances.

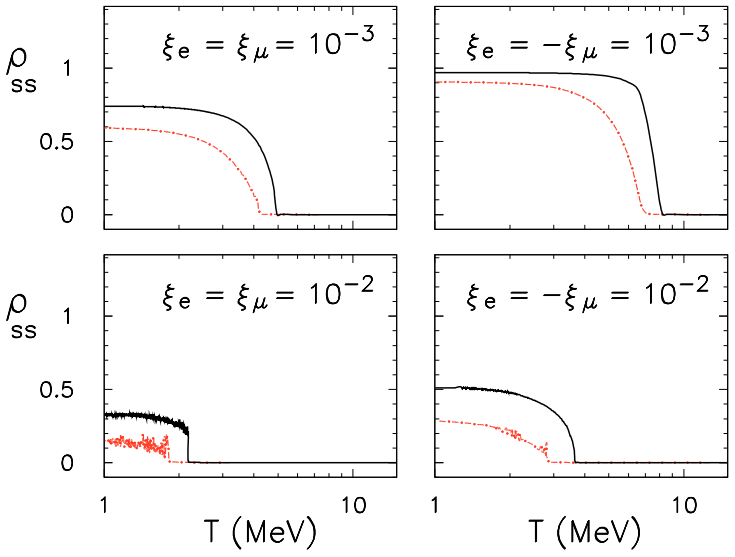

Figure 6.7: Evolution of the total value of the sterile neutrino density matrix element ρ_{ss} for the multi-momentum case (continuos curves) and the average momentum (dot-dashed curves) one with a thermal momentum $\langle y \rangle = 3.15$, as function of the temperature T. Left panels refer to $\xi_e = \xi_\mu$, while in the lowers $\xi_e = -\xi_\mu$. Upper panels correspond to $\xi_e = 10^{-3}$ and right to $\xi_e = 10^{-2}$.

6.5.2.1 Impact on Big-Bang Nucleosynthesis

The primordial abundances of light element are affected by active-sterile neutrino flavor conversions in two ways: by the distortions of the electron (anti)neutrino spectra (a basic input for BBN weak rates) and by the non-electromagnetic radiation content, parametrized via $N_{\rm eff}$.

In the upper panels of Figs. 6.8 and 6.9 are shown the y-dependent ν_e energy spectrum $y^2\varrho_{ee}(y)$ (dashed curve) at $T = 1$ MeV, compared with the initial one $y^2 f_{\rm eq}(y, \xi_e)$ (solid line). In particular Figs. 6.8 refers to $\xi_e = 10^{-3}$ and Fig. 6.9 to $\xi_e = 10^{-2}$. In each figure, in the left panels $\xi_e = \xi_\mu$, while in the right ones $\xi_e = -\xi_\mu$. In order to show clearly the distortion in the ν_e spectrum with respect to the initial one, in the lower panel we plot the ratio

$$R = \frac{\varrho_{ee}(y)}{f_{\rm eq}(y, \xi_e)} \ . \tag{6.44}$$

In the case of $\xi_e = 10^{-3}$, $R \gtrsim 0.95$ for equal asymmetries and $R \gtrsim 0.98$ in the case of opposite asymmetries. Conversely the spectral distortions are more evident for $\xi_e = 10^{-2}$, reaching the value of $R \gtrsim 0.82$ for equal asymmetries and $R \gtrsim 0.9$ for opposite ones.

Indeed for $\xi_e = 10^{-2}$, the resonant active-sterile conversions occur near the active neutrino decoupling temperature and the spectral distortions in the active neutrinos become more evident, as pointed out at first in [166].

Concerning the effective number of neutrino species, neglecting sub-leading corrections, we take $N_{\rm eff} = 3 + \Delta N_{\rm eff}$. This enters the dynamics only via its contribution to the Hubble parameter, see Eq. (6.13), rescaling the standard neutrino energy density contribution ε_ν as

$$\varepsilon_\nu(x, N_{\rm eff}) \to \varepsilon_\nu(x, 3) \left(1 + \frac{\Delta N_{\rm eff}}{3}\right) . \tag{6.45}$$

We numerical compute $\Delta N_{\rm eff}$ in the above equation via the following integral

$$\Delta N_{\rm eff} = \frac{60}{7\pi^4} \int dy \ \ y^3 {\rm Tr}[\varrho(x, y) + \bar{\varrho}(x, y)] \ \ - 2 \ , \tag{6.46}$$

the factor "-2" being due to the fact that we are considering only two active neutrino species.

This quantity is shown in Figure 6.10 for two representative values of asymmetries: $\xi_e = 10^{-3}$ (solid curves) and $\xi_e = 10^{-2}$ (for dashed curves), taken equal for the e and μ sector in the left panel and opposite in the right one. We observe that for $\xi_e = 10^{-3}$ the resonant production of sterile neutrinos starts around $T \simeq 5$ MeV for equal asymmetries, while at $T \simeq 8$ MeV

for opposite ones. Since at these temperatures the active-sterile neutrino conversions mostly occur when the collisional regime is still effective, the active neutrinos are almost fully repopulated, reflecting in a $\Delta N_{\rm eff} \simeq \rho_{ss}$ in both cases (see Fig. 6.7). This is still true for the case $\xi_e = -\xi_\mu = 10^{-2}$, but not when $\xi_e = \xi_\mu = 10^{-2}$. Namely, in this latter situation, the resonant population occur at temperatures $T \sim 2\,\mathrm{MeV}$, comparable to neutrino decoupling temperature, where repopulation of the depleted electron neutrinos is only partial. An appreciable difference (in this case of ~ 0.1) is established between ρ_{ss} and $N_{\rm eff}$.

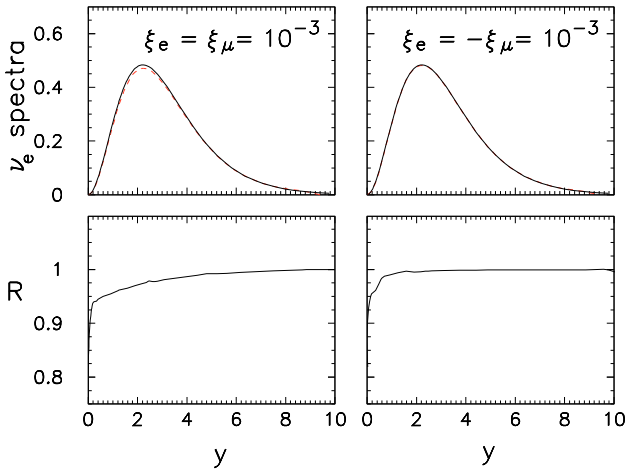

Figure 6.8: Cases with $\xi_e = 10^{-3}$. In the upper panels we show the final ν_e energy spectra at $T = 1$ MeV (dashed curve) and initial ones (continuous curve). In the lower panel we present the ratio R between final and initial ν_e energy spectra. Left panels correspond to $\xi_e = \xi_\mu$ while right panels to $\xi_e = -\xi_\mu$.

The numerical values of the $\Delta N_{\rm eff}$'s found in these representative cases are reported in Table 6.1 together with the values of the abundance of ^{4}He mass fraction Y_p and deuterium ^{2}H, as obtained from a modified version of the numerical code `PArthENoPE` [117], considering a baryon fraction $\omega_b = 0.02249$ and the neutron lifetime $\tau_n = 880.1\,\mathrm{s}$, [14]. In the same table, we also show for comparison the "degenerate BBN" case (i.e. with neutrino asymmetries but no sterile neutrinos) as well as the standard BBN case (i.e. no sterile and no asymmetry).

Technically, we note that the rates $\Gamma_{n\to p}[f_{\nu_e}, f_{\bar\nu_e}]$ and $\Gamma_{p\to n}[f_{\nu_e}, f_{\bar\nu_e}]$ are functionals of the distributions $f_{\nu_e}, f_{\bar\nu_e}$. Denoting with Γ^0 the rates computed

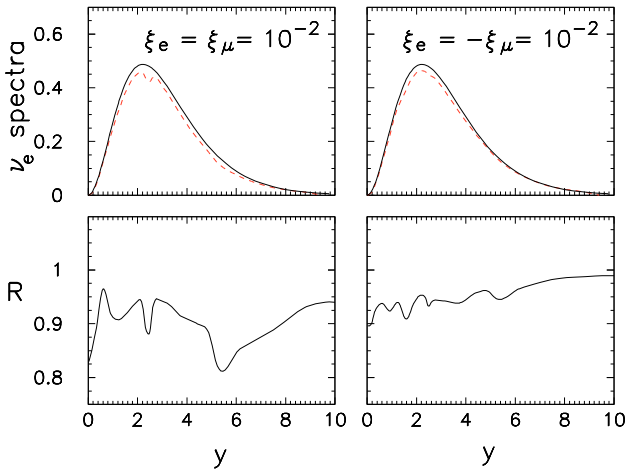

Figure 6.9: Cases with $\xi_e = 10^{-2}$. In the upper panels we show the final ν_e energy spectra at $T = 1$ MeV (dashed curve) and initial ones (continuous curve). In the lower panel we present the ratio R between final and initial ν_e energy spectra. Left panels refer to $\xi_e = \xi_\mu$ while right panels are for $\xi_e = -\xi_\mu$.

in the Born approximation[3] for Fermi-Dirac spectra, and with Γ the actual rates for the cases under consideration, we have calculated the effect of sterile neutrinos by rescaling the rates implemented in the code `PArthENoPE` [117] (see also [194]) by Γ/Γ^0, which has been numerically evaluated and then interpolated. This amounts to a first-order correction in a perturbative approach. The error due to this approximation is safely below 0.3% (see e.g. [195] for the analysis of corrections to Born weak rates) and it is comparable or lower than neglecting the modification to the reheating in the standard scenario. The main source of error in determining the shape of the distribution function, especially for the cases with $|\xi| = 10^{-2}$, comes from the discretization of the neutrino distribution (and the corresponding interpolation). However, test runs performed with a $N_y = 30$ points grid in momentum space, suggest that this does not invalidate the reliability of the size of the effects we found.

With reference to Table 6.1 we note that:
for sufficiently small values of $\xi_{e,\mu}$, the effect of the sterile neutrino production on both Y_p and ^{2}H is due to the increase of $N_{\rm eff}$. For higher values, $|\xi_{e,\mu}| \sim 10^{-2}$, some fraction of the sterile neutrino population is produced relatively late, namely after the the decoupling of the active neutrinos. These cases are associated to a $\Delta N_{\rm eff}$ significantly smaller than 1. While this quantity is still

[3]Limit of infinite nucleon mass.

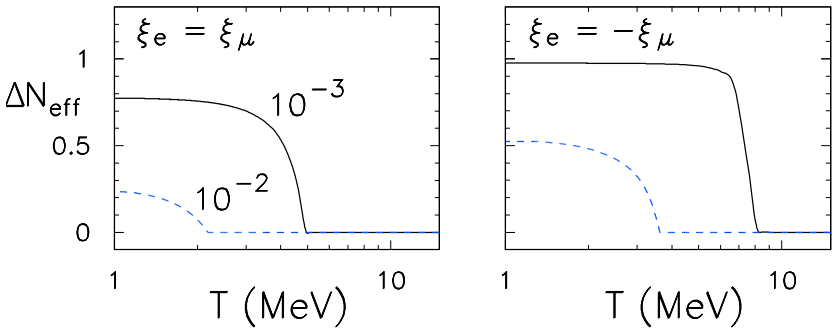

Figure 6.10: Evolution of $\Delta N_{\rm eff}$ in function of the temperature T for equal asymmetries $\xi_e = \xi_\mu$ (left panel) and opposite ones $\xi_e = -\xi_\mu$ (right panel). Solid curves refer to $\xi_e = 10^{-3}$ while dashed curves to $\xi_e = 10^{-2}$.

the main cause of the change in ^{2}H, the effect on Y_p is mainly due to the changes of the weak rates regulating the $n \leftrightarrow p$ chemical equilibrium as a consequence of the distorted ν_e and $\bar{\nu}_e$ distributions. In the case $\xi_e = -\xi_\mu = 10^{-2}$, this effect is estimated to account $\sim 75\%$ of totally with respect the one related to the speed-up of the expansion induced by $\Delta N_{\rm eff}$, while for $\xi_e = \xi_\mu = 10^{-2}$ it becomes three times larger than the other [4]. Quantitatively, we observe sizeable modifications in the BBN yields induce by sterile neutrinos. For comparison, the statistical error on the astrophysical Y_p determination can be as small as 0.001 (although the systematic error is at present several times larger) [196], the determination of ^{2}H/H in the highest quality Quasar system is $(2.535 \pm 0.05) \times 10^{-5}$ [119], and the 1σ errors on $N_{\rm eff}$ and Y_p reported by the combined analysis of the Planck team amount to $\Delta N_{\rm eff} \simeq 0.27$ and $\Delta Y_p \simeq 0.021$ [135], in substantial agreements with earlier forecasts [197].

Important considerations are in the following:

1. The presence of both sterile neutrinos and asymmetries in the evolution produces an increase of the Helium abundance Y_P with respect to the standard BBN, confirming the prediction based on analytical estimations presented in [198]. This trend is opposite of what obtained in degenerate BBN.

2. Since one thermalized sterile neutrino is marginally accepted by the BBN constraint [142], it was speculated by some authors (like in [149]) that a degenerate BBN could relieve the tension with the laboratory

[4] For this case the evolution is extremely slow and there is still a small evolution in the parameters taking place at $T \lesssim 1\,$MeV. Hence the results presented here are *conservative*.

Case	$\Delta N_{\rm eff}$	$\Delta N_{\rm eff}^{\langle y \rangle}$	Y_p	^{2}/H ($\times 10^5$)
$\lvert\xi\rvert \ll 10^{-3}$	1.0	1.0	0.259	2.90
$\xi_e = -\xi_\mu = 10^{-3}$	0.98	0.89	0.257	2.87
$\xi_e = \xi_\mu = 10^{-3}$	0.77	0.51	0.256	2.81
$\xi_e = -\xi_\mu = 10^{-2}$	0.52	0.44	0.255	2.74
$\xi_e = \xi_\mu = 10^{-2}$	0.22	0.04	0.251	2.64
$\xi_e = \lvert\xi_\mu\rvert = 10^{-3}$, no ν_s	~ 0	–	0.246	2.56
$\xi_e = \lvert\xi_\mu\rvert = 10^{-2}$, no ν_s	~ 0	–	0.244	2.55
standard BBN	0	0	0.247	2.56

Table 6.1: We report the values of $\Delta N_{\rm eff}$ and the computed abundances of ^{4}He mass fraction Y_p and deuterium ^{2}H in the different cases considered in our investigation. For comparison we also show in the third column the increase in the effective degrees of freedom obtained in the average momentum approximation, $\Delta N_{\rm eff}^{\langle y \rangle}$.

hints. Indeed large positive neutrino asymmetry decreases the n/p ratio trough the equation

$$\frac{n}{p} \sim e^{\left(-\frac{\Delta m}{T} - \xi_e\right)} \ . \tag{6.47}$$

leading to a decreasing of the Y_P. This decrease would compensate the increase induced by adding sterile neutrinos, creating a positive correlation between the increase of ξ and $N_{\rm eff}$, as shown e.g. in Fig. 6 of Ref. [149]. However this conclusion is not valid when the sterile neutrinos is properly take into account in the evolution (see comment 1).

3. The scenario considered in this work, could lead to a possible inconsistency in the value of $N_{\rm eff}$ extracted from CMB and BBN. Indeed, as shown in the Table 6.1, sterile neutrinos and large asymmetries would produce a relatively low value of $N_{\rm eff}$ (as for example probed by CMB) and an increase of Y_p effecting the BBN. However, the same increase of Y_p could be mimicked by a *larger* $N_{\rm eff}$.

As final remark, we checked that changing the mass and mixing parameters within current uncertainties [199], one can easily obtain $\mathcal{O}(10\%)$ differences in $N_{\rm eff}$. For example, the disappearance experiments prefer larger values of sterile mass splitting than the 0.89 eV^2 used in our work [200], leading to an easier thermalization of the sterile state. Therefore, the results presented here are rather on the conservative side and "precision" computa-

tions would be illusory and premature, given the dependence from unknown or poorly constrained parameters.

Conclusions

Since neutrinos were postulated in 1930 as "desperate way out" to save the energy conservation in the beta decay of nuclei, they have always raised questions. For many decades one of the most pressing issue has been to understand which of the three neutrinos has mass. At this regard, the discovery of atmospheric and solar neutrino oscillations has implied that at least two neutrinos are massive. At present, neutrino oscillations have been firmly established by increasingly accurate measurements using different sources and experimental techniques. Now that the neutrino oscillation framework has been probed, measuring all the mixing angles and the two mass-squared splittings, still interesting questions related to neutrino oscillations are open. In particular, the flavor structure reproducing the observed neutrino mixing still misses a deep theoretical understanding where an initial prejudice seemed to support small values for the neutrino mixing angles, in analogy with what observed in the quark sector. It was quite a surprise to discover a completely different structure with relatively large mixing angles among neutrinos.

Another important question, that has been the topic of this thesis is: *"How do neutrinos oscillate in high-density environments?"* In this context, core-collapse supernovae and the Early Universe represent unique environments to probe the flavor mixing of neutrinos in conditions that cannot realized in any other natural or artificial site. Remarkably, these represent the only two cases in which neutrinos themselves contribute to the background medium for their propagation, making their oscillations a non-linear phenomenon.

In 2006 it was surprising to discover that in the deepest supernova regions these non-linear effects, associated with the neutrino-neutrino interactions, can lead to a collective behavior in the flavor evolution. This can imprint peculiar spectral swaps and splits that are sensitive to the unknown neutrino mass hierarchy. The rich phenomenology associated to this non-linear flavor dynamics is still in its infancy and many unexpected results have been found in the last years.

The study of flavor conversions in the Early Universe is another fasci-

nating problem involving collisional damping, refractive effects from charged leptons, and neutrino self-interactions. In particular, we used this environment as a cosmic laboratory to deal with this timely question: *"Do exist more than three species of neutrinos?"* Recent analysis from cosmological observation data leave open the possibility of extra radiation in the Universe beyond photons and ordinary neutrinos, supporting to the existence of sterile neutrinos. Moreover, anomalous results coming from neutrino oscillation experiments seem to point towards the existence of low-mass sterile neutrinos. However the primordial abundance of thermal sterile neutrinos, with mass preferred by laboratory, would be in tension with cosmological observables. Given this contradictory situation it is very important to study the physical conditions under which sterile neutrinos could be produced in the Early Universe, contributing as extra radiation.

This dissertation presents our results about flavor transitions of neutrinos in supernovae and Early Universe. Let us summarize the main original findings of this work.

In the Chapter 4 we have presented our results on the matter suppression of the self-induced flavor conversions during the supernova accretion phase. We numerically solved the neutrino equations of motion, characterizing the neutrino emissivity and the SN matter density profile, using results from recent neutrino radiation hydrodynamical simulations. We found that collective flavor conversions would be inhibited by a trajectory-dependent effect associated with the large matter term. The matter suppression implies that neutrino oscillations will start outside the neutrino transport region and therefore have a negligible impact on the neutrino heating and explosion dynamics. Furthermore, the possible detection of the next galactic SN neutrino signal from the accretion phase, based on the usual MSW effect in the SN mantle, can allow to determine the neutrino mass hierarchy for values of θ_{13} as large as the one recently measured. We also supported our results presenting a stability analysis of the linearized equations of motion.

In the Chapter 6 we have discussed our results on the active-sterile neutrino oscillations in the Early Universe. We derived strong bounds on the active-sterile neutrino mixing using the recent measurement of the the effective number of neutrino species by the Planck satellite experiment. Our results point towards a strong tension with the short-baseline hints of sterile neutrinos. In order to relieve this disagreement, we proposed to modify the standard cosmological scenario, introducing primordial asymmetries in the active neutrino species. These would inhibit the sterile neutrino production via in-medium suppression of the sterile-active mixing. Nevertheless, neutrino asymmetries permit also a resonant sterile neutrino production. Solving the kinetic equations of motion for the active-sterile neutrino ensemble, we have

found that an asymmetry $L > 10^{-3}$ is necessary in order to have a sufficient suppression of the sterile neutrino abundance, improving the agreement with the laboratory hints. However, for such asymmetries, active-sterile flavor conversions happen so late to significantly distort the electron (anti)neutrino spectra. We explored the effect of these distortions on the Big Bang Nucleosynthesis.

In conclusion, the study of neutrino physics has been always accompanied by surprises. Often our theoretical prejudices have been disproved by experimental results, that required to significantly modify our previous pictures. In this context, supernvoae and Early Universe represent two laboratories where amazing effects can still arise. A complete understanding of flavor conversions in supernovae is mandatory in order to interpret the neutrino signal from the next Galactic explosion. This could shed light on the mechanism of a stellar gravitational collapse and on neutrino fundamental properties, like the mass ordering. Early Universe will continue to be an important environment to probe neutrino properties, such as the mass and the possibility of extra sterile neutrinos.

Therefore, further studies are motivated in order to better understand the neutrino flavor conversions in these high-density media and their impact on cosmology and astrophysics.

Bibliography

[1] B. Pontecorvo, Sov. Phys. JETP **7**, 172 (1958) [Zh. Eksp. Teor. Fiz. **34**, 247 (1957)].

[2] B. Pontecorvo, Sov. Phys. JETP **26**, 984 (1968) [Zh. Eksp. Teor. Fiz. **53**, 1717 (1967)].

[3] Z. Maki, M. Nakagawa and S. Sakata, Prog. Theor. Phys. **28**, 870 (1962).

[4] A. Strumia and F. Vissani, hep-ph/0606054.

[5] G. L. Fogli, E. Lisi, A. Marrone, D. Montanino, A. Palazzo and A. M. Rotunno, Phys. Rev. D **86**, 013012 (2012).

[6] D. V. Forero, M. Tortola and J. W. F. Valle, Phys. Rev. D **86**, 073012 (2012).

[7] F. P. An *et al.* [DAYA-BAY Collaboration], Phys. Rev. Lett. **108**, 171803 (2012).

[8] J. K. Ahn *et al.* [RENO Collaboration], Phys. Rev. Lett. **108**, 191802 (2012).

[9] Y. Abe *et al.* [Double Chooz Collaboration], Phys. Rev. D **86**, 052008 (2012).

[10] G. G. Raffelt, Prog. Part. Nucl. Phys. **64**, 393 (2010).

[11] A. D. Dolgov, S. H. Hansen, S. Pastor, S. T. Petcov, G. G. Raffelt and D. V. Semikoz, Nucl. Phys. B **632**, 363 (2002).

[12] J. Hamann, S. Hannestad, G. G. Raffelt, I. Tamborra and Y. Y. Y. Wong, Phys. Rev. Lett. **105**, 181301 (2010).

[13] K. N. Abazajian, M. A. Acero, S. K. Agarwalla, A. A. Aguilar-Arevalo, C. H. Albright, S. Antusch, C. A. Arguelles and A. B. Balantekin *et al.*, arXiv:1204.5379 [hep-ph].

[14] J. Beringer *et al.* [Particle Data Group Collaboration], Phys. Rev. D **86**, 010001 (2012).

[15] S. M. Bilenky, J. Hosek and S. T. Petcov, Phys. Lett. B **94**, 495 (1980).

[16] J. Schechter and J. W. F. Valle, Phys. Rev. D **25**, 2951 (1982).

[17] W. Buchmuller, R. D. Peccei and T. Yanagida, Ann. Rev. Nucl. Part. Sci. **55**, 311 (2005).

[18] G. Altarelli and F. Feruglio, Springer Tracts Mod. Phys. **190**, 169 (2003).

[19] R. Davis, Jr., D. S. Harmer and K. C. Hoffman, Phys. Rev. Lett. **20**, 1205 (1968).

[20] J. N. Bahcall, "Neutrino Astrophysics," CAMBRIDGE, UK: UNIV. PR. (1989) 567p

[21] J. N. Bahcall, M. H. Pinsonneault and S. Basu, Astrophys. J. **555**, 990 (2001).

[22] Q. R. Ahmad *et al.* [SNO Collaboration], Phys. Rev. Lett. **89**, 011301 (2002).

[23] Q. R. Ahmad *et al.* [SNO Collaboration], Phys. Rev. Lett. **89**, 011302 (2002).

[24] Y. Fukuda *et al.* [Super-Kamiokande Collaboration], Phys. Rev. Lett. **81**, 1562 (1998) [hep-ex/9807003].

[25] K. Eguchi *et al.* [KamLAND Collaboration], Phys. Rev. Lett. **90**, 021802 (2003).

[26] K. Abe *et al.* [T2K Collaboration], Phys. Rev. Lett. **107**, 041801 (2011).

[27] T. -K. Kuo and J. T. Pantaleone, Rev. Mod. Phys. **61**, 937 (1989).

[28] L. Wolfenstein, Phys. Rev. D **17**, 2369 (1978).

[29] S. P. Mikheev and A. Yu. Smirnov, Yad. Fiz. **42**, 1441 (1985) [Sov. J. Nucl. Phys. **42**, 913 (1985)].

[30] A. I. Belesev, A. I. Bleule, E. V. Geraskin, A. A. Golubev, N. A. Golubev, O. V. Kazachenko, E. P. Kiev and Y. .E. Kuznetsov *et al.*, Phys. Lett. B **350**, 263 (1995).

[31] F. M. Fraenkle, arXiv:1110.0087 [physics.ins-det].

[32] S. Hannestad, A. Mirizzi, G. G. Raffelt and Y. Y. Y. Wong, JCAP **1008**, 001 (2010.

[33] P. A. R. Ade *et al.* [Planck Collaboration], arXiv:1303.5076 [astro-ph.CO].

[34] S.R. Elliott and J. Engel, J. Phys. G **30**, R183 (2004).

[35] H. V. Klapdor-Kleingrothaus, A. Dietz, H. L. Harney and I. V. Krivosheina, Mod. Phys. Lett. A **16**, 2409 (2001).

[36] H. V. Klapdor-Kleingrothaus, I. V. Krivosheina, A. Dietz and O. Chkvorets, Phys. Lett. B **586**, 198 (2004).

[37] K. Hirata *et al.* [KAMIOKANDE-II Collaboration], Phys. Rev. Lett. **58**, 1490 (1987).

[38] K. S. Hirata, T. Kajita, M. Koshiba, M. Nakahata, Y. Oyama, N. Sato, A. Suzuki and M. Takita *et al.*, Phys. Rev. D **38**, 448 (1988).

[39] R. M. Bionta, G. Blewitt, C. B. Bratton, D. Casper, A. Ciocio, R. Claus, B. Cortez and M. Crouch *et al.*, Phys. Rev. Lett. **58** (1987) 1494.

[40] S. Fukuda *et al.* [Super-Kamiokande Collaboration], Phys. Rev. Lett. **86**, 5656 (2001).

[41] C. Arpesella *et al.* [Borexino Collaboration], Phys. Lett. B **658**, 101 (2008).

[42] Y. Ashie *et al.* [Super-Kamiokande Collaboration], Phys. Rev. D **71** 112005 (2005).

[43] P. Adamson *et al.* [MINOS Collaboration], Phys. Rev. Lett. **101**, 131802 (2008).

[44] P. Adamson *et al.* [MINOS Collaboration], arXiv:1304.6335 [hep-ex].

[45] N. Agafonova *et al.* [OPERA Collaboration], Phys. Lett. B **691**, 138 (2010).

[46] G. L. Fogli, E. Lisi, A. Marrone, A. Palazzo and A. M. Rotunno, Phys. Rev. Lett. **101**, 141801 (2008).

[47] A. Aguilar-Arevalo *et al.* [LSND Collaboration], Phys. Rev. D **64**, 112007 (2001).

[48] B. Armbruster *et al.* [KARMEN Collaboration], Phys. Rev. D **65**, 112001 (2002).

[49] K. Eitel, New J. Phys. **2** (2000) 1.

[50] A. A. Aguilar-Arevalo *et al.* [MiniBooNE Collaboration], Phys. Rev. Lett. **98** 231801(2007).

[51] A. A. Aguilar-Arevalo *et al.* [MiniBooNE Collaboration], Phys. Rev. Lett. **105**, 181801 (2010).

[52] M. Antonello, B. Baibussinov, P. Benetti, E. Calligarich, N. Canci, S. Centro, A. Cesana and K. Cieslik *et al.*, arXiv:1209.0122 [hep-ex].

[53] G. Mention, M. Fechner, T. Lasserre, T. A. Mueller, D. Lhuillier, M. Cribier and A. Letourneau, Phys. Rev. D **83**, 073006 (2011).

[54] M. A. Acero, C. Giunti and M. Laveder, Phys. Rev. D **78**, 073009 (2008).

[55] C. Giunti and M. Laveder, "3+1 and 3+2 Sterile Neutrino Fits," Phys. Rev. D **84**, 073008 (2011).

[56] C. Giunti and M. Laveder, "Status of 3+1 Neutrino Mixing," Phys. Rev. D **84**, 093006 (2011) .

[57] J. Kopp, P. A. N. Machado, M. Maltoni and T. Schwetz, arXiv:1303.3011 [hep-ph].

[58] M. Archidiacono, N. Fornengo, C. Giunti and A. Melchiorri, Phys. Rev. D **86**, 065028 (2012).

[59] J. T. Pantaleone, Phys. Lett. B **342**, 250 (1995).

[60] G. Sigl and G. Raffelt, Nucl. Phys. B **406**, 423 (1993).

[61] G. Raffelt, G. Sigl and L. Stodolsky, Phys. Rev. D **45**, 1782 (1992).

[62] G. Raffelt, G. Sigl and L. Stodolsky, Phys. Rev. Lett. **70**, 2363 (1993) [Erratum-ibid. **98**, 069902 (2007)].

[63] A. D. Dolgov, Sov. J. Nucl. Phys. **33**, 700 (1981) [Yad. Fiz. **33**, 1309 (1981)].

[64] R. Barbieri and A. Dolgov, Nucl. Phys. B **349**, 743 (1991).

[65] C. Giunti, C. W. Kim and W. P. Lam, Phys. Rev. D **43**, 164 (1991).

[66] A. D. Dolgov, S. H. Hansen, S. Pastor, S. T. Petcov, G. G. Raffelt and D. V. Semikoz, Nucl. Phys. B **632**, 363 (2002).

[67] H. T. Janka, K. Langanke, A. Marek, G. Martinez-Pinedo and B. Mueller, Phys. Rept. **442**, 38 (2007).

[68] B. Dasgupta, arXiv:1005.2681 [hep-ph].

[69] A. S. Dighe and A. Y. Smirnov, Phys. Rev. D **62**, 033007 (2000).

[70] H. Duan, G. M. Fuller and Y. Z. Qian, Ann. Rev. Nucl. Part. Sci. **60**, 569 (2010).

[71] G. G. Raffelt, "Stars as laboratories for fundamental physics : The astrophysics of neutrinos, axions, and other weakly interacting particles," Chicago, USA: Univ. Pr. (1996) 664 p.

[72] S. Hannestad, G. G. Raffelt, G. Sigl and Y. Y. Y. Wong, Phys. Rev. D **74**, 105010 (2006) [Erratum-ibid. D **76**, 029901 (2007)] .

[73] A. Esteban-Pretel, S. Pastor, R. Tomas, G. G. Raffelt and G. Sigl, Phys. Rev. D **76**, 125018 (2007).

[74] G. L. Fogli, E. Lisi, A. Marrone and A. Mirizzi, JCAP **0712**, 010 (2007).

[75] A. Esteban-Pretel, A. Mirizzi, S. Pastor, R. Tomas, G. G. Raffelt, P. D. Serpico and G. Sigl, Phys. Rev. D **78**, 085012 (2008) .

[76] A. Mirizzi and R. Tomas, Phys. Rev. D **84**, 033013 (2011).

[77] H. Duan, G. M. Fuller, JCarlson and Y. -Z. Qian, Phys. Rev. D **74**, 105014 (2006).

[78] G.E. Brown, H.A. Bethe, and G. Baym, Nucl. Phys. A **375**, 481 (1982).

[79] S.E. Woosley and T.A. Weaver, Ann. Rev. Astron. Astrophys. **24**, 205 (1986).

[80] A. Burrows, Nature **403**, 727 (2000).

[81] T. Fischer, S. C. Whitehouse, A. Mezzacappa, F. -K. Thielemann and M. Liebendorfer, Astron. Astrophys. **517**, A80 (2010).

[82] M. T. .Keil, G. G. Raffelt and H. -T. Janka, Astrophys. J. **590**, 971 (2003).

[83] G. L. Fogli, E. Lisi, D. Montanino and A. Mirizzi, Phys. Rev. D **68**, 033005 (2003).

[84] S. Pastor, G. G. Raffelt and D. V. Semikoz, Phys. Rev. D **65**, 053011 (2002).

[85] H. Duan, G. M. Fuller and Y. -Z. Qian, Phys. Rev. D **76**, 085013 (2007).

[86] H. Duan, G. M. Fuller, J. Carlson and Y. -Q. Zhong, Phys. Rev. Lett. **99**, 241802 (2007).

[87] A. Esteban-Pretel, arXiv:0912.1616 [hep-ph].

[88] R. F. Sawyer, Phys. Rev. D **79**, 105003 (2009).

[89] G. G. Raffelt and G. Sigl, Phys. Rev. D **75**, 083002 (2007).

[90] H. Duan, G. M. Fuller, J. Carlson and Y. -Z. Qian, Phys. Rev. Lett. **100**, 021101 (2008).

[91] B. Dasgupta, A. Dighe, A. Mirizzi and G. G. Raffelt, Phys. Rev. D **77**, 113007 (2008).

[92] B. Dasgupta, A. Dighe, G. G. Raffelt and A. Y. .Smirnov, Phys. Rev. Lett. **103**, 051105 (2009) [arXiv:0904.3542 [hep-ph]].

[93] K. Nomoto, Astrophys. J. **277**, 791 (1984).

[94] K. Nomoto, Astrophys. J. **322**, 206 (1987).

[95] F. S. Kitaura, H.-Th. Janka and W. Hillebrandt, Astron. Astrophys. **450**, 345 (2006).

[96] S. E. Woosley, A. Heger and T. A. Weaver,

[97] H. Shen, H. Toki, K. Oyamatsu and K. Sumiyoshi, Nucl. Phys. A **637**, 435 (1998).

[98] M. Liebendoerfer, O. E. B. Messer, A. Mezzacappa, S. W. Bruenn, C. Y. Cardall and F. K. Thielemann, Astrophys. J. Suppl. **150**, 263 (2004).

[99] T. Totani, K. Sato, H. E. Dalhed and J. R. Wilson, Astrophys. J. **496**, 216 (1998).

[100] L. Hudepohl, B. Muller, H. T. Janka, A. Marek and G. G. Raffelt, Phys. Rev. Lett. **104**, 251101 (2010) [Erratum-ibid. **105**, 249901 (2010)],

[101] H. Duan and A. Friedland, Phys. Rev. Lett. **106**, 091101 (2011).

[102] B. Dasgupta, A. Mirizzi, I. Tamborra and R. Tomàs, Phys. Rev. D **81**, 093008 (2010).

[103] B. Dasgupta and A. Dighe, Phys. Rev. D **77**, 113002 (2008).

[104] G. M. Fuller, R. Mayle, B. S. Meyer and J. R. Wilson, Astrophys. J. **389**, 517 (1992).

[105] S. Sarikas, G. G. Raffelt, L. Hudepohl and H. -T. Janka, Phys. Rev. Lett. **108**, 061101 (2012). [

[106] A. Banerjee, A. Dighe and G. Raffelt, Phys. Rev. D **84**, 053013 (2011).

citeOtt:2008jb

[107] C. D. Ott, A. Burrows, L. Dessart and E. Livne, Astrophys. J. **685**, 1069 (2008).

[108]

[108] P. D. Serpico, S. Chakraborty, T. Fischer, L. Hudepohl, H. -T. Janka and A. Mirizzi, Phys. Rev. D **85**, 085031 (2012).

[109] E. Borriello, S. Chakraborty, A. Mirizzi, P. D. Serpico and I. Tamborra, Phys. Rev. D **86**, 083004 (2012).

[110] J. Lesgourgues, G. Mangano, G. Miele, S. Pastor, "Neutrino Cosmology," Cambridge University Press (2013).

[111] E. W. Kolb, M. S. Turner, "The Early Universe," Westview Press (1994).

[112] A. D. Dolgov and Y. .B. Zeldovich, Rev. Mod. Phys. **53**, 1 (1981).

[113] K. Enqvist and V. Semikoz, Phys. Lett. B **312**, 310 (1993).

[114] G. Mangano, G. Miele, S. Pastor and M. Peloso, Phys. Lett. B **534**, 8 (2002).

[115] G. Mangano, G. Miele, S. Pastor, T. Pinto, O. Pisanti and P. D. Serpico, Nucl. Phys. B **729**, 221 (2005).

[116] S. Sarkar, Rept. Prog. Phys. **59**, 1493 (1996).

[117] O. Pisanti, A. Cirillo, S. Esposito, F. Iocco, G. Mangano, G. Miele and P. D. Serpico, Comput. Phys. Commun. **178**, 956 (2008).

[118] F. Iocco, G. Mangano, G. Miele, O. Pisanti and P. D. Serpico, Phys. Rept. **472** (2009) 1.

[119] M. Pettini and R. Cooke, arXiv:1205.3785 [astro-ph.CO]

[120] Y. I. Izotov, T. X. Thuan, Astrophys. J. **710**, L67-L71 (2010).

[121] G. Mangano, G. Miele, S. Pastor, T. Pinto, O. Pisanti and P. D. Serpico, Nucl. Phys. B **756**, 100 (2006).

[122] G. Mangano, G. Miele, S. Pastor, O. Pisanti and S. Sarikas, Phys. Lett. B **708**, 1 (2012).

[123] K. Nakayama, F. Takahashi and T. T. Yanagida, Phys. Lett. B **697**, 275 (2011).

[124] J. Jaeckel, J. Redondo and A. Ringwald, Phys. Rev. Lett. **101**, 131801 (2008).

[125] J. Hasenkamp and J. Kersten, arXiv:1212.4160 [hep-ph].

[126] M. Cicoli, J. P. Conlon and F. Quevedo, Phys. Rev. D **87**, 043520 (2013).

[127] P. Graf and F. D. Steffen, JCAP **1302**, 018 (2013).

[128] G. Hinshaw, *et al.*, arXiv:1212.5226 [astro-ph.CO].

[129] S. Bashinsky and U. Seljak, Phys. Rev. D **69**, 083002 (2004). [astro-ph/0310198].

[130] W. Hu, D. J. Eisenstein, M. Tegmark and M. J. White, Phys. Rev. D **59**, 023512 (1999).

[131] J. Dunkley, R. Hlozek, J. Sievers, V. Acquaviva, P. A. R. Ade, P. Aguirre, M. Amiri and J. W. Appel *et al.*, Astrophys. J. **739**, 52 (2011).

[132] R. Keisler, C. L. Reichardt, K. A. Aird, B. A. Benson, L. E. Bleem, J. E. Carlstrom, C. L. Chang and H. M. Cho *et al.*, Astrophys. J. **743**, 28 (2011).

[133] B. A. Reid, L. Verde, R. Jimenez and O. Mena, JCAP **1001**, 003 (2010).

[134] J. Lesgourgues and S. Pastor, Adv. High Energy Phys. **2012**, 608515 (2012)

[135] P. A. R. Ade *et al.* [Planck Collaboration], arXiv:1303.5076 [astro-ph.CO].

[136] S. Das, B. D. Sherwin, P. Aguirre, J. W. Appel, J. R. Bond, C. S. Carvalho, M. J. Devlin and J. Dunkley *et al.*, Phys. Rev. Lett. **107**, 021301 (2011)

[137] M. C. Gonzalez-Garcia, M. Maltoni and J. Salvado, JHEP **1008**, 117 (2010).

[138] E. Komatsu *et al.* [WMAP Collaboration], Astrophys. J. Suppl. **192**, 18 (2011).

[139] Z. Hou, *et al.*, arXiv:1212.6267 [astro-ph.CO].

[140] J. L. Sievers, *et al.*, arXiv:1301.0824 [astro-ph.CO].

[141] A. G. Riess, L. Macri, S. Casertano, H. Lampeitl, H. C. Ferguson, A. V. Filippenko, S. W. Jha and W. Li *et al.*, Astrophys. J. **730**, 119 (2011) [Erratum-ibid. **732**, 129 (2011)]

[142] G. Mangano and P. D. Serpico, Phys. Lett. B **701**, 296 (2011)

[143] T. D. Jacques, L. M. Krauss and C. Lunardini, arXiv:1301.3119 [astro-ph.CO].

[144] C. Giunti, *et al.*, arXiv:1210.5715 [hep-ph].

[145] F. Pietropaolo, J. Phys. Conf. Ser. **408**, 012010 (2013).

[146] J. Lesgourgues and S. Pastor, Phys. Rept. **429**, 307 (2006)

[147] Y. Y. Y. Wong, Ann. Rev. Nucl. Part. Sci. **61**, 69 (2011)

[148] S. Riemer-Sorensen, D. Parkinson and T. M. Davis, arXiv:1301.7102 [astro-ph.CO].

[149] J. Hamann, S. Hannestad, G. G. Raffelt and Y. Y. Y. Wong, JCAP **1109**, 034 (2011).

[150] S. Riemer-Sorensen, D. Parkinson, T. M. Davis and C. Blake, Astrophys. J. **763**, 89 (2013)

[151] B. H. J. McKellar and M. J. Thomson, Phys. Rev. D **49**, 2710 (1994).

[152] K. Enqvist, K. Kainulainen and J. Maalampi, Phys. Lett. B **249**, 531 (1990).

[153] K. Enqvist, K. Kainulainen and M. J. Thomson, Nucl. Phys. B **373**, 498 (1992).

[154] K. Enqvist, K. Kainulainen and J. Maalampi, Phys. Lett. B **244**, 186 (1990).

[155] P. Di Bari, P. Lipari and M. Lusignoli, Int. J. Mod. Phys. A **15**, 2289 (2000).

[156] P. Di Bari and R. Foot, Phys. Rev. D **61**, 105012 (2000).

[157] P. Di Bari and R. Foot, Phys. Rev. D **63**, 043008 (2001).

[158] P. Di Bari, Phys. Rev. D **65**, 043509 (2002) [Addendum-ibid. D **67**, 127301 (2003)] .

[159] A. D. Dolgov, S. H. Hansen, S. Pastor and D. V. Semikoz, Astropart. Phys. **14**, 79 (2000).

[160] P. Di Bari, R. Foot, R. R. Volkas and Y. Y. Y. Wong, Astropart. Phys. **15**, 391 (2001).

[161] R. Foot and R. R. Volkas, Phys. Rev. Lett. **75**, 4350 (1995).

[162] R. Foot, M. J. Thomson and R. R. Volkas, Phys. Rev. D **53**, R5349 (1996) .

[163] N. F. Bell, R. R. Volkas and Y. Y. Y. Wong, Phys. Rev. D **59**, 113001 (1999). [hep-ph/9809363].

[164] D. P. Kirilova and M. V. Chizhov, Phys. Rev. D **58**, 073004 (1998).

[165] D. P. Kirilova and M. V. Chizhov, The Resonant case," Nucl. Phys. B **591**, 457 (2000).

[166] K. Abazajian, N. F. Bell, G. M. Fuller and Y. Y. Y. Wong, Phys. Rev. D **72**, 063004 (2005).

[167] C. T. Kishimoto, G. M. Fuller and C. J. Smith, Phys. Rev. Lett. **97**, 141301 (2006).

[168] A. D. Dolgov and F. L. Villante, Nucl. Phys. B **679**, 261 (2004).

[169] M. Cirelli, G. Marandella, A. Strumia and F. Vissani, Nucl. Phys. B **708**, 215 (2005).

[170] Y. -Z. Chu and M. Cirelli, Phys. Rev. D **74**, 085015 (2006).

[171] K. N. Abazajian and P. Agrawal, JCAP **0810**, 006 (2008).

[172] A. Melchiorri, O. Mena, S. Palomares-Ruiz, S. Pascoli, A. Slosar and M. Sorel, JCAP **0901**, 036 (2009).

[173] S. Hannestad, I. Tamborra and T. Tram, JCAP **1207**, 025 (2012).

[174] C. Giunti and C. W. Kim, "Fundamentals of Neutrino Physics and Astrophysics", Oxford University Press 2007.

[175] M. Maltoni, T. Schwetz and J. W. F. Valle, Phys. Rev. D **65**, 093004 (2002).

[176] G. L. Fogli, E. Lisi, A. Marrone and A. Palazzo, Prog. Part. Nucl. Phys. **57**, 742 (2006).

[177] K. Enqvist, K. Kainulainen and J. Maalampi, Nucl. Phys. B **349**, 754 (1991).

[178] S. Esposito, G. Miele, S. Pastor, M. Peloso and O. Pisanti, Nucl. Phys. B **590**, 539 (2000).

[179] Y. -Z. Chu and M. Cirelli, Phys. Rev. D **74**, 085015 (2006)

[180] M. Archidiacono, N. Fornengo, C. Giunti, S. Hannestad and A. Melchiorri, arXiv:1302.6720 [astro-ph.CO].

[181] A. Esmaili and O. L. G. Peres, Phys. Rev. D **85**, 117301 (2012).

[182] P. C. de Holanda and A. Y. .Smirnov, Phys. Rev. D **83**, 113011 (2011).

[183] P. D. Serpico and G. G. Raffelt, Phys. Rev. D **71**, 127301 (2005).

[184] S. Pastor, T. Pinto and G. G. Raffelt, Phys. Rev. Lett. **102**, 241302 (2009).

[185] G. Mangano, G. Miele, S. Pastor, O. Pisanti and S. Sarikas, JCAP **1103**, 035 (2011).

[186] E. Di Valentino, M. Lattanzi, G. Mangano, A. Melchiorri and P. Serpico, Phys. Rev. D **85**, 043511 (2012).

[187] E. Castorina, U. Franca, M. Lattanzi, J. Lesgourgues, G. Mangano, A. Melchiorri and S. Pastor, arXiv:1204.2510 [astro-ph.CO].

[188] J. A. Harvey and E. W. Kolb, Phys. Rev. D **24**, 2090 (1981).

[189] A. Casas, W. Y. Cheng and G. Gelmini, Nucl. Phys. B **538**, 297 (1999).

[190] A. D. Dolgov, "Neutrinos in cosmology," Phys. Rept. **370**, 333 (2002).

[191] P. Di Bari and R. Foot, Phys. Rev. D **65**, 045003 (2002).

[192] G. Karagiorgi, A. Aguilar-Arevalo, J. M. Conrad, M. H. Shaevitz, K. Whisnant, M. Sorel and V. Barger, Phys. Rev. D **75**, 013011 (2007), [Erratum-ibid. D **80**, 099902 (2009)].

[193] `http://www.nag.co.uk/numeric/numerical_libraries.asp`

[194] P. D. Serpico, S. Esposito, F. Iocco, G. Mangano, G. Miele and O. Pisanti, 'JCAP **0412**, 010 (2004).

[195] S. Esposito, G. Mangano, G. Miele and O. Pisanti, Nucl. Phys. B **540**, 3 (1999).

[196] Y. I. Izotov, T. X. Thuan, Astrophys. J. **710**, L67-L71 (2010).

[197] L. Perotto, J. Lesgourgues, S. Hannestad, H. Tu and Y. Y. Y. Wong, JCAP **0610**, 013 (2006).

[198] C. J. Smith, G. M. Fuller, C. T. Kishimoto and K. N. Abazajian, Phys. Rev. D **74**, 085008 (2006).

[199] C. Giunti, private comunication.

[200] C. Giunti, M. Laveder, Y. F. Li and H. W. Long, Phys. Rev. D **87**, 013004 (2013).

Eidesstattliche Versicherung

Declaration on Oath

Hiermit erklre ich Eides statt, dass ich die vorliegende Dissertations-Schrift selbst verfasst und keine anderen als die angegebenen Quellen und Hilfsmittel benutzt habe.

I Hereby declare, on oath, that I have written the present dissertation by my own and have not used other than the acknowledged and aids.

Hamburg, 15 January 2014

Ninetta Saviano

Acknowledgements

I express my gratitude to everyone who contributed to this dissertation with advice, support and encouragement. Foremost I would thank my family, in particular my parents and Antonio who supported me in every moment. I am indebted to my advisors, Alessandro Mirizzi and Gennaro Miele, not only for proposing this research project but even more for their great support and advice. I also benefited very much from the close and inspiring collaboration with Gianpiero Mangano and Ofelia Pisanti always available for suggestions and discussions. I am also grateful to my friends, especially to Francesca Calore who shared with me this work and personal experience. This work was in part supported by the German Science Foundation (DFG) within the Collaborative Research Center 676 "Particles, Strings and the Early Universe" and by the Instituto Nazionale di Fisica Nucleare (INFN).